Progress in Materials Science 141 (2024) 101219

Contents lists available at ScienceDirect

Progress in Materials Science

journal homepage: www.elsevier.com/locate/pmatsci

Supercapacitor electrode energetics and mechanism of operation: Uncovering the voltage window

Deepak Pandey [a,b], Kowsik Sambath Kumar [a,b], Jayan Thomas [a,b,c,*]

[a] Department of Materials Science and Engineering, University of Central Florida, Orlando, FL 32816, United States
[b] NanoScience Technology Center, University of Central Florida, Orlando, FL 32826, United States
[c] CREOL, College of Optics and Photonics, University of Central Florida, Orlando, FL 32816, United States

A B S T R A C T

In recent years, supercapacitors have received enormous popularity as energy storage devices due to their high power density and long-lasting cycle life compared to Lithium-Ion batteries and other similar energy storage devices. To attain high energy density, pseudocapacitive materials are being primarily investigated for asymmetric configuration-based supercapacitors. While most of the research is focused on finding new pseudocapacitive materials with higher specific capacitance, only very limited knowledge is available about how high voltage can be achieved in supercapacitors. Here, we present a comprehensive review of the mechanism of operation of the asymmetric supercapacitors. We discuss in detail the factors affecting the voltage window of the asymmetric supercapacitors like 1) the work function of the electrodes, 2) the highest occupied molecular orbital (HOMO) and lowest unoccupied molecular orbital (LUMO) levels of the electrolyte and 3) hydrogen and oxygen evolution overpotentials. We included an in-depth review of how work function originates in pseudocapacitive electrodes and its relation to Fermi level and electronegativity. Though transition metal oxides and carbon-based materials are used as base materials for this study, their application can be extended to any electrode-active material as long as it operates on the pseudocapacitive principle.

1. Introduction

Are you thrilled by speed? If your answer is 'Yes,' here is exciting news for you: Lamborghini has recently launched its new hybrid-supercar "Sián – FKP 37", which can accelerate from 0 to 100 km h^{-1} in just 2.8 s [1]. With 800 plus horsepower engine and a 48-volt e-motor built into its transmission, it is probably the most powerful Lambo in the history of the company. However, the distinctive feature which makes it stand out in terms of its power is the implementation of supercapacitors instead of traditional Lithium-ion (Li-ion) batteries for its e-motors [2]. The argument which the company presented for this shift is that the supercapacitors have high power density, quick charge time and 3–4 times longer cycle life when compared to Li-ion batteries. This marks the growing significance of supercapacitors as reliable energy storage devices. Though Li-ion batteries and supercapacitors (also known as electrochemical capacitors) are both popular energy storage devices, they have their niche applications based on energy and power requirements. Generally, Li-ion batteries exhibit high energy density and are good for long-duration usage. On the other hand, supercapacitors are suitable for devices that require high power density [3–5]. The recent supercapacitor research focuses on developing devices with both high energy and power densities. The energy density of a supercapacitor depends mainly on its specific capacitance and the cell voltage [6]. Mathematically, this is given according to Eq. (1)

$$E = \frac{1}{2} C_g \Delta V^2 \tag{1}$$

* Corresponding author at: Department of Materials Science and Engineering, University of Central Florida, Orlando, FL 32816, United States.
E-mail address: Jayan.Thomas@ucf.edu (J. Thomas).

https://doi.org/10.1016/j.pmatsci.2023.101219
Received 23 May 2023; Received in revised form 13 November 2023; Accepted 19 November 2023
Available online 23 November 2023

where E is the specific energy density in Wh kg^{-1}, C_g is the specific capacitance in F g^{-1}, and ΔV is the cell voltage after the ohmic drop. An important aspect to notice here is that the energy density is linearly dependent on specific capacitance but quadratically on cell voltage. So, an increase in the cell voltage will have a greater influence on the energy density. The specific capacitance of a supercapacitor depends primarily on the number of active sites, the type of charge storage mechanism exhibited by the supercapacitor electrodes, and the cell voltage.

High voltage supercapacitors are gaining popularity because of their potential applications in a wide variety of areas. Airbus, in its latest and most advanced passenger aircraft A380, uses high voltage supercapacitors to operate the emergency exit doors [7]. They are more powerful for quicker deployment in case of emergencies. Supercapacitors are much more reliable, safer, and long-lasting than Li-ion batteries. Toyota Yaris (Hybrid-R) and PSA Peugeot Citroen have started using high voltage supercapacitors for their start-stop fuel-saving systems [8]. Very similar to this, Mazda's i-ELOOP system uses high voltage supercapacitors to charge when the vehicle decelerates and uses it to power the onboard electrical systems. High voltage supercapacitors also supplement batteries in the starter system of diesel-railroad locomotives, which have diesel-electric transmissions [9]. Besides these applications, high-voltage supercapacitors find their potential in military applications (pulsed laser systems) [10], medical support [11], fork-lift trucks [12], street lamps, etc. [13]. Thus, it becomes imperative to investigate and understand the underlying principles which govern the cell voltage and charge storage mechanism for a supercapacitor device.

Currently, there are only a few reports which discuss the aspects like the mechanism of operation and cell voltage arising from energy-interaction of electrodes and electrolyte in detail. Herein, we take both a quantitative and qualitative approach to discuss the energy interactions occurring within an operational asymmetric supercapacitor. However, in order to build this understanding, we need to consider different types of charge storage mechanisms and how supercapacitors are classified based on (1) mechanism of energy storage and (2) configuration. This helps to avoid any confusion that could arise when we generalize this study for a particular "configuration" or "mechanism" in a supercapacitor. This is discussed in the first part of the review.

The second part of this review focuses on the energy aspect of the voltage window. First, the voltage window is discussed in metal oxide-based pseudocapacitors where the role of work-function is critical in deciding the voltage window. The output voltage a supercapacitor can deliver depends mainly on the interactions of energy states of the two electrodes and the energy levels of the electrolyte [14–16]. Energy states of the electrodes are marked by their fermi-level (E_F), which also governs the electrochemical potential (μ). However, for a supercapacitor electrode in action, the energy which enables the charge transfer is the work-function (Φ) of the electrodes [14]. This work function (Φ) is defined as the energy required to pull an electron from a material's fermi level to a local vacuum level ($E_{v,\ local}$) through the bulk (of the material) and the surface (interface) [17]. Therefore, it is a combined effect of an electrode's electrochemical potential and its surface potential. Since supercapacitors operate by storing charge at the electrode surface instead of bulk [18], the work function becomes more relevant compared to just electrochemical potential. Therefore, for understanding the energy interactions, it is essential to discuss the work function of electrodes and the factors influencing them. Second, the voltage window in carbon-based double-layer capacitors has also been discussed. Many oxygen-based surface functional groups on carbon-based electrodes tend to cause unwanted redox reactions. These redox reactions may cause the early onset of electrolyte decomposition, lowering the voltage window. On the other hand, in some carbon-based electrodes, an electrode–electrolyte interface could prevent the onset of such unwanted side redox reactions, which could help in the expansion of the voltage window.

Besides the effect of electrode material, the electrolyte itself can offer a wide range in the potential window. It is important to distinguish the role of electrode material and the role of electrolytes in establishing the voltage window for an assembled device. This review also focuses on different types of electrolytes and their achievable voltage window. Overpotential in electrolytes is another poorly understood aspect among the supercapacitor community. It is discussed in the third part of this review. Overpotential is highly desirable for the electrodes if they have to deliver high voltage in an asymmetric configuration [19]. Supercapacitors employing organic electrolytes can achieve a stable voltage in the range of 2.5–4.0 V. Still, they suffer from inherent problems like relatively high equivalent series resistance, low ion diffusion rate, toxicity, and fire hazards. On the other hand, aqueous electrolytes do not have such limitations and are safe and eco-friendly. However, they have a lower potential window of 1.23 V. However, many asymmetric supercapacitors employing aqueous electrolytes can deliver well beyond this range due to a build-up of hydrogen and oxygen evolution overpotential. Therefore, high overpotential on the electrodes can significantly enhance the voltage window of supercapacitors.

Finally, once the above-discussed factors affecting the voltage window are understood, a supercapacitor can likely be designed with a tuned voltage window. The theoretical voltage window of these customized supercapacitors can be known and understood before they are fabricated in a lab. This helps to save a lot of time, materials and manpower. Therefore, the purpose of this review is to bring forth the underlying mechanism of operation in supercapacitors and how various energies interact within an operational supercapacitor from the reported literature. This review enables the development of supercapacitors with highly optimized electrodes having enhanced voltage output.

2. Classification of supercapacitors and their charge storage mechanisms

Supercapacitors can be classified categorically based on (i) their electrode configuration and (ii) the type of charge storage mechanism exhibited by their electrodes. It is imperative to do this bifurcation to help us understand the mechanism of operation and evaluate the performances of supercapacitors. As discussed by Silvia et al., the classification of supercapacitors in many reported papers mixed up the above two categories [20]. This has led to much confusion and erroneous designations. Hence it is necessary to define the type of a particular supercapacitor. Recently, a lot of tutorials and perspectives have been published to discuss the differences between electrochemical behaviors of supercapacitors, batteries, their hybrids, and methods to evaluate their performance

[21–23]. Therefore, it is imperative to study various charge storage modes/mechanisms, as it directly affects their operation. Before we proceed to the classification, we start discussing the different charge storage mechanisms in supercapacitors and their battery hybrids.

2.1. Types of charge storage mechanisms

For any energy storage device to function, the mechanism to store the charges would define its applicability and efficacy for different applications [24]. Fig. 1 represents the schematic of different charge storage mechanisms that occur in supercapacitor electrode-active materials, namely.

(1) Electric double-layer (EDL) charge storage
(2) Pseudocapacitive charge storage
(3) Battery-type charge storage [25,26].

Fig. 1 differentiates the faradaic charge storage with the non-faradaic type and capacitive charge storage with hybrid capacitive/battery-type charge storage. One of the key features of an electric double-layer capacitor (EDLC) is that there is no charge transfer between the electrolyte and the electrode, i.e., this is a non-faradaic charge-storage process [27,28]. The specific capacitance in EDLCs is highly dependent on accessible surface area and other surface properties of the electrode.

The general formula for the capacitance of the EDLC electrodes can be given by Eq. (2)

$$C = A \times (\varepsilon_0 . \varepsilon_r / \mathrm{d}) \tag{2}$$

where A is the effective surface area, d is the effective charge separation distance between the electrical double layer, i.e., debye length, ε_0 is the permittivity of free space and ε_r is the relative permittivity of the liquid electrolyte relative to vacuum [29].

2.1.1. EDL charge storage

Fig. 2 explains the different charge storage mechanisms that take place in a supercapacitor electrode/electrolyte interface with the help of a representative negative electrode. When an electronically conducting electrode is dipped in an ionically conducting electrolyte, a double layer of ions is spontaneously formed at the electrode/electrolyte interface due to the re-organization of charges. This type of charge storage is represented as zone [A] in Fig. 2. Here, the charges are physically adsorbed and electrostatically held on the surface of the electrode with a polarized solvent molecule layer sandwiched in between [29–34]. This type of charge storage mechanism is known as 'EDL charge storage.' In Fig. 2, IHL refers to the Inner Helmholtz Layer, which is the stern layer of polarized solvent molecules. In this layer the polarized solvent molecules cannot move in the longitudinal directions and are mostly static due to spatially adsorbing and columbic interactions. The region next to the stern layer is the diffusion layer which consists of the cations from the electrolyte. The stern layer and the diffusion layer are together called double layer. The negative charge from the electrode and the positive charge (from the electrolyte cation) together form the double layer capacitance.

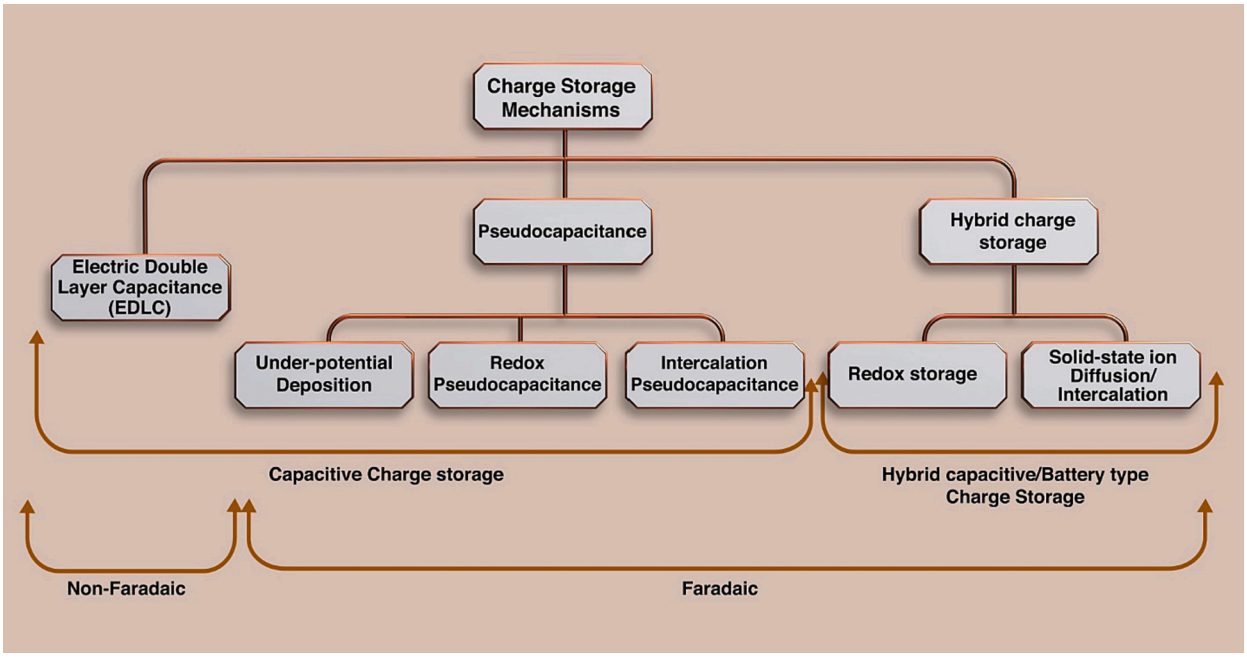

Fig. 1. A schematic showing various charge storage mechanisms in a supercapacitor electrode-active material.

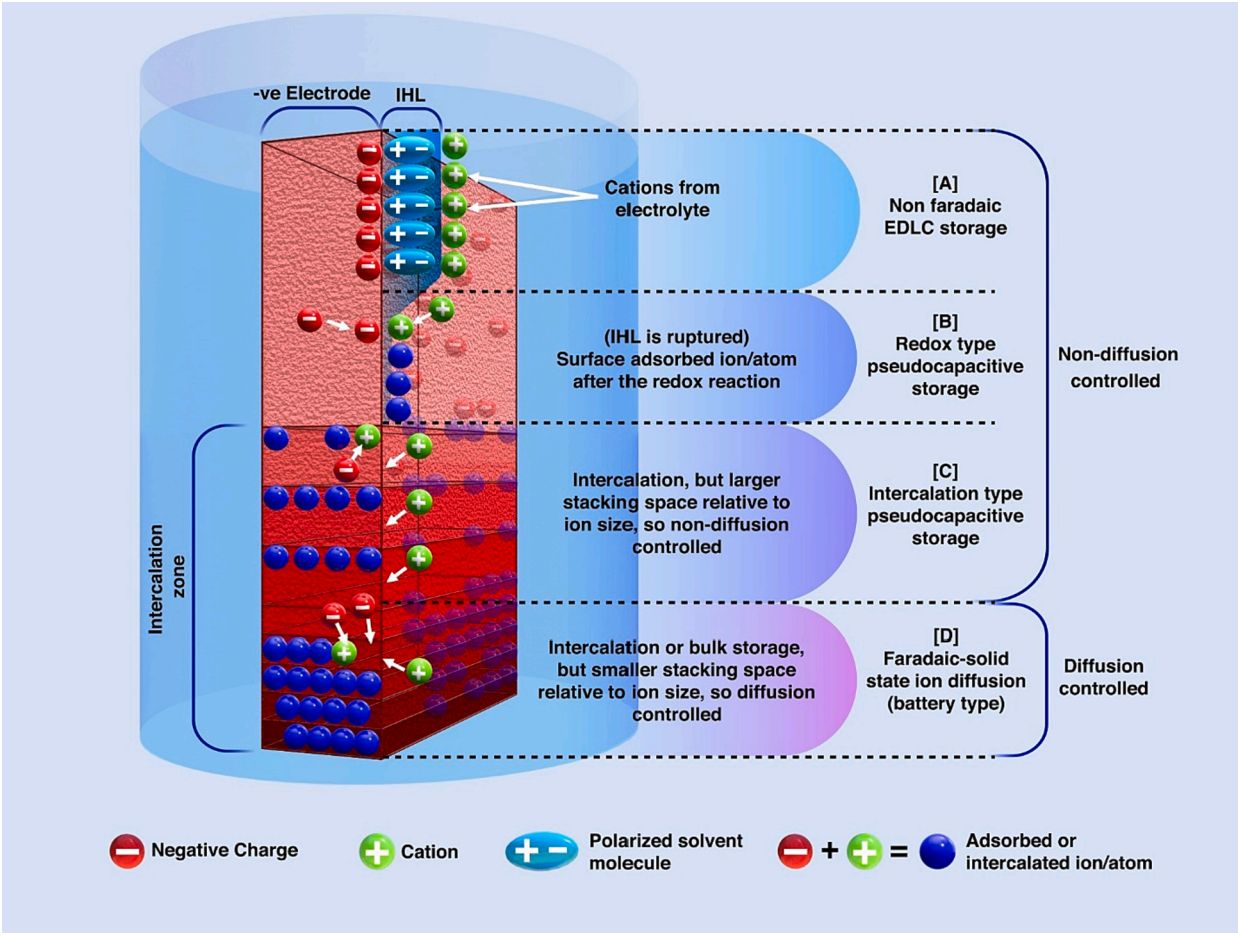

Fig. 2. Cartoon showing different mechanisms of charge storage in a representative negative electrode material. Zone [A], [B], and [C] show non-diffusion controlled capacitive storage. Zone [D] shows diffusion-controlled storage.

2.1.2. Pseudocapacitive charge storage

Pseudocapacitance is a faradaic mode of charge storage, where charge transfer occurs between the surface adsorbed or near-surface adsorbed ion/atom and the active material on the electrode via fast reversible redox reactions [35–37]. In this mechanism, electrons are transferred between the active material and electrolyte ions, bringing changes in the valence state of both species [38–41]. First-ever material that was found to show pseudocapacitance was ruthenium oxide (RuO_2) [14,42]. Though the charge storage in the RuO_2 electrode is by the faradaic charge transfer process, the cyclic voltammogram (CV) profile showed a capacitive-type behavior, i.e., a rectangular shape [39]. The term pseudocapacitive is used to identify the electrode whose electrochemical signature is capacitive in nature but operates via fast and reversible surface redox reactions [43]. Even though the process is faradaic in origin, the capacitance obeys a direct proportionality between the extent of charges stored and the change in potential. This mechanism is represented by zone [B] and [C] in Fig. 2.

Pseudocapacitance can be further divided into three categories as shown in Fig. 1: i) Underpotential deposition: this occurs when ions deposit on a two-dimensional metal-electrolyte interface at potentials positive to their reversible redox potentials (e.g., H^+ on Pt or Pd^{+2} on Au) [44–46]. This mechanism is well known for the adsorption of a hydrogen atom (H-atom) on catalytic noble metals including Pt, Rh, Ru, and Ir, along with electrodeposition of metal cations at potentials less negative than their equilibrium potentials for cation reduction [44]. ii) Redox pseudocapacitance: this type of pseudocapacitance is based on fast and reversible redox reactions via electron transfer between an oxidized species, O_x (eg. RuO_2 [40], MnO_2 [47], or p-doped conducting polymers [48,49] and reduced species (e.g., $RuO_{2-z}(OH)_z$, $MnO_{2-z}(OH)_z$ or n-doped conducting polymers). These reactions are usually characterized by electrochemical adsorption of cations on the surface of oxidized species with a fast and reversible electron transfer across the interface between the cation of the electrolyte and the electrode [50]. This type of pseudocapacitance is schematically represented by zone [B] in Fig. 2. iii) Intercalation pseudocapacitance: this type of capacitance is achieved when charges get stored via ion insertion/ intercalation in a layered crystalline material [51,52]. This is schematically represented by zone [C] in Fig. 2. When this type of intercalation happens, it is also accompanied by a change in the metal valence to maintain electric neutrality. For a cation intercalation supercapacitor, the electrochemical behavior is an interplay between Li-ion batteries and supercapacitors [52]. The major difference

between intercalation pseudocapacitor and intercalating Li-ion battery is capacitor-like electrochemical signatures, such as fast-ion transport kinetics, shorter charge time, near rectangular CV profile, long cycling stability and high rate capabilities.

2.1.3. Hybrid charge storage

The third category of charge storage is hybrid (or battery-type) charge storage, which is no longer a surface phenomenon, but a bulk charge storage mechanism marked by slow ion transport kinetics, slower charge and discharge process, high energy density, and lower cycle life when compared to capacitive storage. Intercalation in a battery-type electrode is limited by solid-state ion diffusion, which makes the current 'diffusion-controlled,' resulting in lower power density, as shown in zone (D) in Fig. 2. Discussion of this type of storage is out of this paper's scope. We only introduced it to show the difference between the intercalating pseudocapacitive storage (non-diffusion controlled) and intercalating battery-type storage (bulk phenomenon and diffusion controlled).

2.2. Classification of supercapacitors

During the early stages of supercapacitor development (early 2000), it was easy to classify and categorize supercapacitors, as there were only a few variations in the design and charge storage mechanism. However, as the research gained pace in developing newer materials for their charge storage properties, the classification became more and more complex [53]. Often it was observed that "charge storage mechanism" based classification was confused with "configuration based" classification resulting in misleading designations [20]. Thus, it became crucial to define the criterion and scope of classification for supercapacitors clearly.

Current supercapacitors can be classified based on (1) configuration (of electrodes) and (2) the mechanism of charge storage. In configuration-based classification, the electrode design, choice of active material and amount of active material are considered as key parameters for further sub-classification. Fig. 3 shows the classification based on the configuration and assembly of supercapacitor electrodes.

2.2.1. Classification based on electrode configuration

Based on the type of electrode configurations, the supercapacitors are classified as (i) symmetric, (ii) asymmetric, and (iii) hybrid-type, (which could be present in both symmetric and asymmetric configurations) as shown in Fig. 3 and explained in the following paragraphs.

(i) *Symmetric configuration:* In a symmetric supercapacitor, both the positive and negative electrodes are made of the same kind of active material [54,55]. The electrode-active material can be either of EDL capacitive or pseudocapacitive nature, but only one

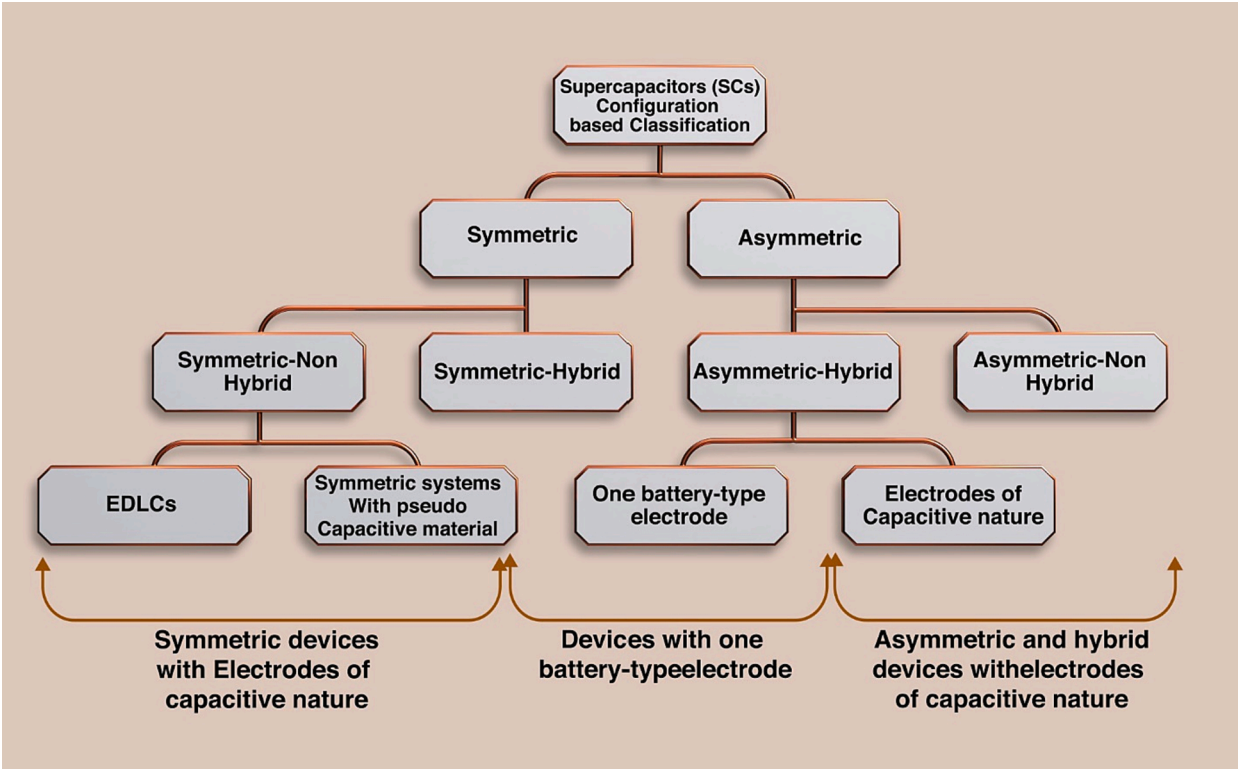

Fig. 3. Classification of supercapacitors based on the electrode configuration.

type of charge storage mechanism is displayed by both the electrodes [56]. In addition to having the same material on both the electrodes, generally, the amount of material is also kept the same for achieving the charge balance. In most cases of a symmetrical configuration, carbon materials, metal oxides (MOs) and conducting polymers are used as the active materials [31,40,50]. The EDL-type storage mechanism employed by carbon materials, which uses a purely electrostatic type of charge storage mechanism, is the simplest and the most prevalent system of the symmetric configuration [33,57]. However, when symmetric systems use MOs or conducting polymers, the storage mechanism becomes pseudocapacitive. They are referred to as 'symmetric systems with pseudocapacitive materials.'

(ii) *Asymmetric configuration:* Supercapacitors can also be constructed by using dissimilar electrode-active materials as the positive and negative electrodes. This design is known as 'asymmetric design,' and by using this configuration, a high energy density can be achieved even with aqueous electrolytes [58]. The electrodes can be made of carbon materials, MOs, and conducting polymers [59,60]. However, the charge storage mechanism may be the same on both the electrodes, even with an asymmetric design. Therefore, as we have stressed earlier, it is essential to understand that 'symmetric' and 'asymmetric' only refer to the configuration of electrodes in a supercapacitor. These discrepancies in the classification and erroneous nomenclature become more prominent while including 'hybrid configuration' [59].

(iii) *Hybrid configuration:* By all means, the term 'hybrid' refers to when the charge storage mechanism is dominated by bulk solid-state ion diffusion [61]. This type of mechanism is also popularly called a battery-type charge storage mechanism. When either one electrode out of the two or some part of any of the two electrodes shows charge and discharge by solid-state ion diffusion, the term 'hybrid' can be used. A hybrid device is often referred to as a configuration where one of the electrodes is battery-type, while the other is capacitive.

It is unfortunate that the term 'asymmetric' and 'hybrid' are ambiguously used in some reports in the literature, which has often resulted in misleading designations [62,63]. One probable reason for this ambiguity is the term 'asymmetric' to show different types of charge storage mechanisms (EDLC, faradaic, and solid-state ion diffusion) on the two separate electrodes. This is, again, a mix of "configuration"-based classification with "mechanism"-based. As per the internationally accepted nomenclature, a hybrid configuration refers to a device, which performs somewhere between a battery and a supercapacitor in terms of its energy density and power density [64]. This is usually made practical by using one battery-type electrode and another capacitive-type electrode in the device assembly [22,62,65–68]. The reason for the ambiguity between 'asymmetric' and 'hybrid' may be the fact that a lot of hybrid type designs (one battery- and the other capacitive-type electrode) are asymmetric in nature as well, because of using different types of active material on different electrodes. But this does not guarantee the fact that all the hybrid devices will be asymmetric in the configuration. This ambiguity is also clarified by the classification shown in Fig. 3.

Further, both the symmetric and asymmetric configurations may or may not form a hybrid device. This is dependent on the charge storage mechanism of the positive and negative electrodes used for fabricating the supercapacitor. The classification of supercapacitors based on their charge storage mechanism in their electrodes is shown in Fig. 4.

Asymmetric non-hybrid: Generally, asymmetric-non hybrid systems employ two carbon materials of different nature [69–71], or two dissimilar conducting polymers assembled as the positive and negative electrodes [72,73]. These asymmetric-non hybrids can be built by using two different capacitive-type materials on each electrode, which can be made of either EDL-type or faradaic-type. The most

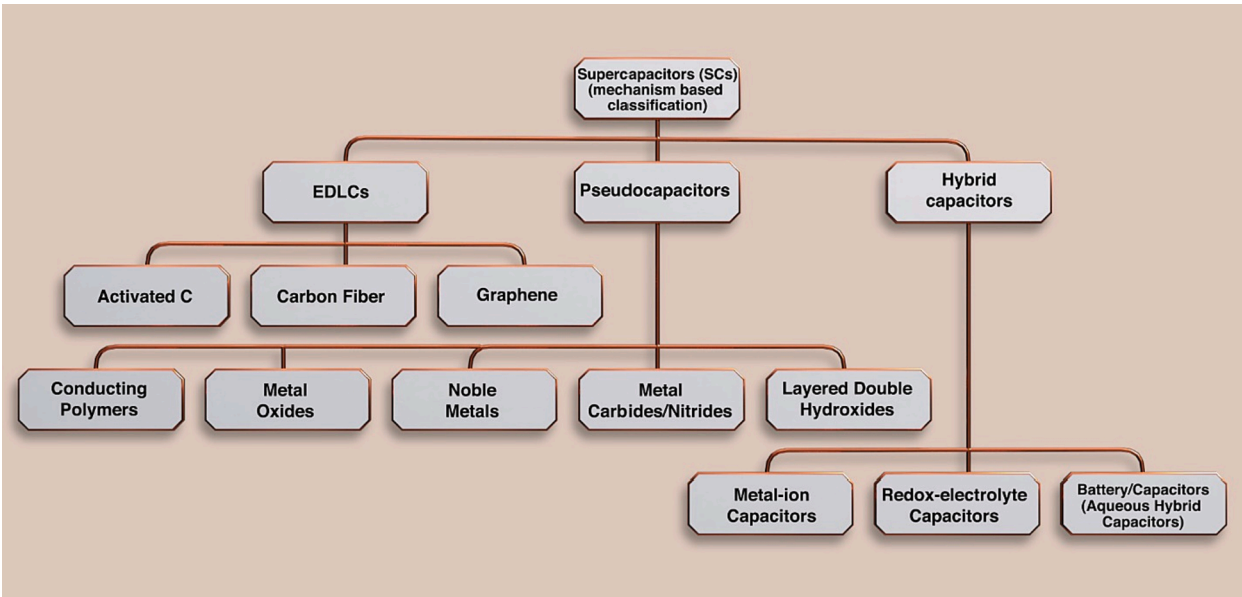

Fig. 4. Classification of supercapacitors based on the mechanism of charge storage.

popular assembly in this category is activated carbon/MO supercapacitor [59,74–78], or activated carbon/conducting polymer supercapacitor [79,80] and MO/MO supercapacitor [81].

Asymmetric hybrid: In the case of an asymmetric-hybrid design, one electrode is of capacitive-type, whereas the other one is of battery-type, which stores charge by solid-state ion diffusion. This type of configuration has recently attracted the attention of the scientific community as it is capable of enhancing the energy density of supercapacitors [64]. A well-studied Li-ion intercalation electrode, which is of battery-type, is the $Li_4Ti_5O_{12}$ reported by Amatucci et al. in 2001 [64]. Later on, battery-type electrodes such as $LiMn_2O_4$ or $LiCoO_2$ [82], $Li_2Ti_3O_7$ [83], $LiMnO_2$ [84], $LiNi_{0.5}Mn_{1.5}O_4$ [85], electronically conducting polymers [86,87] were also used to fabricate asymmetric hybrid supercapacitors.

It is important to note that even symmetric systems can be hybrid in nature.

Symmetric hybrid and non-hybrids: In a symmetric hybrid, both the electrode-active materials are the same and the mass of both the electrodes should be the same. Mostly carbonaceous material such as activated carbon is used as the electrode and an aqueous solution with the electrochemically active molecule is used as an electrolyte [88–92]. This electrochemically active molecule instigates a redox reaction on the surface of one of the electrodes, turning it into a battery. This category of symmetric hybrids is new and gives the benefit of using the same material on both electrodes. This means only one type of active material is needed, so it is advantageous for mass production of the device on an industrial scale. Symmetric non-hybrids are a simple system of two identical electrodes, among which none of the electrodes offers a redox or battery-type reaction for charge storage. Mostly, these are carbon-based electrodes that tend to store charge through EDLC mechanism [93,94].

2.2.2. Classification based on charge storage mechanism

Supercapacitors are also classified based on their charge storage mechanism. This is shown in Fig. 4. Some exemplary active materials that follow these mechanisms have also been listed under their respective category [61]. This classification is based on simply naming the supercapacitors by the charge storage mechanism they follow. We have discussed various charge storage mechanisms and schematically shown them in Figs. 1 and 2, so this classification can be easily derived from that discussion. Once we get a clear picture of the charge storage mechanism and classification of supercapacitors, it becomes easier to comprehend the operational mechanism of a supercapacitor from the point of view of its energy levels and work function of the active materials. This study would also help to understand the designing criteria of supercapacitors and how we can increase the performance of a supercapacitor based on its operational voltage window.

3. Energetics of the supercapacitor electrodes (in non-operational condition)

It is clear from Eq. (1) that the energy density can be enhanced either by increasing the specific capacitance or the operating voltage [95,96]. The specific capacitance primarily depends on the surface morphology of the supercapacitor electrodes and the type of charge storage mechanism, whereas the operating voltage depends on the electrolyte dissociation. By fabricating a symmetric supercapacitor with an organic electrolyte, one can effectively increase the operating voltage [96,97]. Organic electrolytes can sustain high operating voltage but are not environmentally benign. On the other hand, aqueous electrolytes are eco-friendly but have a limited voltage window (less than1.2 V in a symmetric configuration, which is discussed in detail in Section 4). But even by using aqueous electrolytes, the low operating voltage issue can be tackled by fabricating asymmetric supercapacitors with electrodes having a wide work function difference. The asymmetric supercapacitor electrodes may exhibit EDL-type or faradaic-type or a combination of both type charge storage, as discussed previously [6,98–100]. In this section, we will first discuss the factors affecting the work function and how the work function engineering of the MO electrode helps to achieve high operating voltage in asymmetric supercapacitors.

Recently, a strategy of enhancing the operating voltage window of an asymmetric supercapacitor by using MO-based electrodes with a maximum work function difference has achieved popularity. Among the family of supercapacitor electrode materials, MOs have been extensively used for fabricating asymmetric supercapacitors since they possess a wide range of work functions and hence high voltage can be achieved using aqueous electrolytes. Besides providing high voltage, MO-based asymmetric supercapacitors can also deliver high specific capacitance and energy density compared to carbon materials and conducting polymers [101]. The work function can vary from a low value (3 eV for ZrO_2) to a high value (7 eV for V_2O_5) in the case of MO electrodes [102]. The electrolyte decomposition at the respective electrodes depends primarily on their work functions, thereby directly affecting the output voltage [103,104]. This warrants a detailed discussion about the work function and the energetic requirement for moving an electron to and from an electrode material.

The work function is defined as the energy required to move an electron from an atom's fermi level to the local vacuum level. Once a supercapacitor starts its operation, work function plays a key role in determining the charge transfer process (either from the electrode to electrolyte or from the electrolyte to the electrode). A key point to note here is that the work function is not just the bulk material property but rather a property that is also influenced by the surface features of the material. This can be understood by examining the energies involved in the work function of the electrode material in a supercapacitor. Two contributing factors of the work function of an electrode:

(a) electrochemical potential of the active material (μ_e) and
(b) surface diploe moment (also known as surface potential) of the electrode (δ) [105].

Electron chemical potential (or simply electrochemical potential) of the electrode-active material is a bulk material property that arises from the Fermi level of the material. In contrast, the surface potential is purely a surface property that may vary locally within a

material. This surface potential acts as an additional energetic barrier/facilitator to the electron at the electrode surface or at the electrode/electrolyte interface when removing it from the bulk [105,106]. The reason for its origin lies in the distortion of the electron cloud around the nucleus of the atom (of the active material) present on the electrode surface, causing an electron density spilling out from the surface. This can make the surface side (towards vacuum) negative while the bulk side positive [106]. However, it can also happen due to dangling bonds or adsorption of impurity molecules at the electrode surface [17]. The dipole barrier caused by this distortion set-up an interfacial electrostatic field, which contributes to the surface potential. The surface potential may vary locally from point to point and thus causes a deviation in the work function of the material at different locations on the electrode's surface. Fig. 5 shows an illustrative diagram of how surface dipole affects the overall work function when the work function is measured along a line on the electrode's surface.

It is tough to control the work function of a given material and also to achieve reproducibility due to its extreme sensitivity to a number of factors. Some of these factors are studied well, but some others are yet unknown. Since the work function is a resultant of both the surface potential (surface property) and the electrochemical potential (bulk property) of the material, the work function of the supercapacitor electrode may vary even locally on the same electrode, as shown in Fig. 5. The surface potential found to alter the work function locally is primarily dependent on factors such as crystallographic orientation, [103] surface roughness, surface termination, and reconstruction. [103,104] It also depends on adsorbed foreign entities [107], which are hard to control. Hence, it is challenging to reproduce the work function of a given material. While the surface potential may just locally vary the work function, the electrochemical potential may change the work function in the bulk of the material. A number of factors like impurities, defects, dopants, crystal structure and chemical state may alter the bulk electrochemical potential that causes a change in the overall work function [108,109]. However, using high purity materials and implementing meticulous preparation methods, it is possible to minimize the effect of these factors on the electrochemical potential to a great extent. This may help the work function only dependent on surface potential, which still remains a challenge to control.

4. Principles of electrode material selection based on work function

In order to achieve a high voltage window for a supercapacitor, it is important to understand the origin of potential from an electrode redox reaction. Born-Haber cycle based on the first law of thermodynamics provides the overall energy change during a simple electrode reaction [14]. Consider an electrode material M in an aqueous solution with ferric ions (Fe^{+3}), which are getting reduced to ferrous ions (Fe^{+2}) during the redox reaction. The energy cycle of the above conversion is given by.

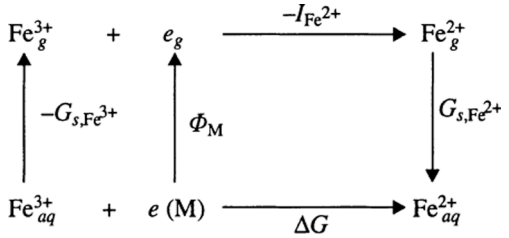

For the overall energy interaction of this half-cell reaction, change in Gibbs free energy can be given as

$$\Delta G = -G_{s,Fe^{3+}} + \phi_M + (-I_{Fe^{2+}}) + G_{s,Fe^{2+}}$$

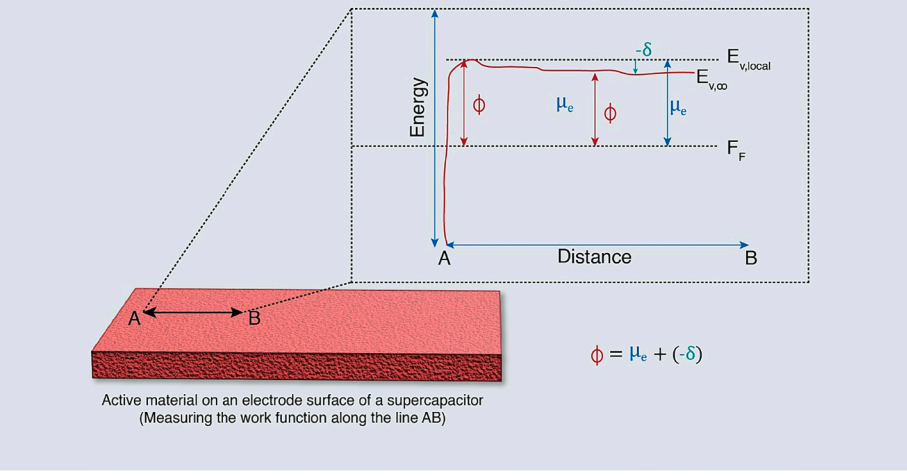

Fig. 5. Energy levels on the surface of a solid showing how the surface dipole (δ) and the electron chemical potential (μ_e) alter the work function (Φ) of the material (E_F is the fermi level, $E_{V,local}$ is the local vacuum level and $E_{v,\infty}$ is the absolute vacuum level).

where G_s is the Gibbs energy of solvation (hydration) of Fe^{+2} and Fe^{+3} ions. The G_s values of both Fe^{+2} and Fe^{+3} are large negative quantities. I is the ionization energy of the gas phase of Fe^{2+} ions getting converted to the gas phase Fe^{+3} ions. ϕ_M is the electronic work-function of the electrode material which directly enters this energy interaction. Hence the hypothetical electrode potential of this half-cell reaction is given by $E_{half\text{-}cell} = -\mathbf{\Delta G}/zF$, where F is the faraday constant, and z is the number of electrons transferred per half-cell reaction [14]. This is how the electrode's work function affects its electrode potential $E_{half\text{-}cell}$ in the half-cell reaction.

In an asymmetric supercapacitor, when two dissimilar electrode-active materials are used as positive and negative electrodes, the working potential window is given by Eqs. (3)–(6) [81,110–112].

$$E_{cell} = E_0 + \Delta E_1 + \Delta E_2 \tag{3}$$

$$E_{cell} = \frac{1}{F} \times \left(\omega^{\beta} - \omega^{\alpha}\right) \times N_A + \Delta E_1 + \Delta E_2 \tag{4}$$

where ω^{β} and ω^{α} are electrochemical potentials (derived from fermi level) of the positive and negative electrodes, respectively, N_A is Avogadro's constant, E_0 is the standard electrode potential, ΔE_1 and ΔE_2 are the surface dipole potentials of positive and negative electrodes, respectively and F is the Faraday constant.

$$E_{cell} = \left[\left(\frac{1}{F} \times \omega^{\beta} \times N_A\right) + \Delta E_1\right] - \left[\left(\frac{1}{F} \times \omega^{\alpha} \times N_A\right) + \Delta E_2\right] \tag{5}$$

Eq. (5) can thus be written as.

$$E_{cell} = [\text{Work function of Electrode 1}] - [\text{Work function of Electrode 2}] \tag{6}$$

For a symmetric supercapacitor, $\Delta E_1 = -\Delta E_2$ and $\omega^{\beta} = \omega^{\alpha}$ since the same material is used as the positive and negative electrodes. Hence, the additional potential window becomes zero for a symmetric supercapacitor. Therefore, the operating voltage is determined by the energy of dissociation of the electrolytes and a maximum of 1.23 V can be achieved when an aqueous electrolyte is used. However, it is different for an asymmetric supercapacitor because dissimilar electrode materials cause differences in the electrochemical potentials of the electrodes. Therefore, the work function difference becomes non-zero. The surface potentials are also not equal and opposite in the case of an asymmetric supercapacitor. It can be observed from eq. (2) that the higher the difference in the electrochemical potentials of the two materials, the wider the potential window for the asymmetric supercapacitor. By rearranging eq. (4), it can be seen that the potential window of an asymmetric supercapacitor is the difference in the work functions of the two electrodes. However, this should be analyzed based on (i) work function modifications due to solvated electrolyte ion adsorbed on the electrode surface, (ii) energy levels of the electrolyte used, and (iii) effects of hydrogen and oxygen evolution overpotentials on the electrodes. Based on the reported literature, we will discuss these factors in detail in the following sections. Fig. 6 lists the different MO-based electrodes used in the supercapacitors as either positive or negative electrodes, along with their work functions [113–116].

Symmetric configuration is not the focus of this review since this configuration has a limited potential window. However, all voltage-determining aspects pertaining to the electrolyte are equally applicable to symmetric design too.

Fig. 6 helps in designing a high-voltage supercapacitor based on the work function difference between the two MOs. From eq. (4), it can be perceived that the operating potential window is dependent on the difference in the work function of the electrode materials.

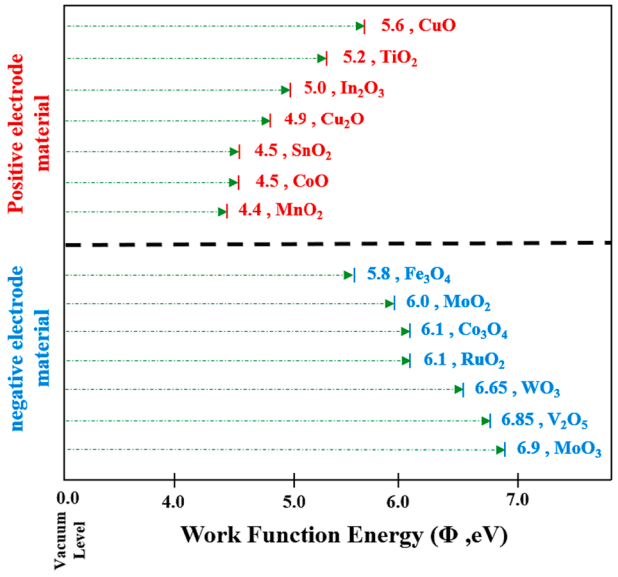

Fig. 6. Schematic of the work functions of various MOs used as supercapacitor electrodes.

However, it is also important to note that the operating potential window is not just equal to the work function difference of the two electrode materials as variations may occur due to other factors such as electrolyte energy levels, ionic mobility, operating temperature, etc. For example, from Fig. 6, if we want to design a high-voltage supercapacitor using MO electrodes such as MnO_2 as the positive electrode and MoO_3 as the negative electrode, theoretically, a wide potential window of 2.5 V (6.9 eV − 4.4 eV) can be obtained. In the case of d^0 MOs (where metallic ion has 0 e^- in their outermost d orbital), obtaining a work function same as its theoretical value is extremely difficult due to the oxygen vacancy defects [17,117]. A detailed explanation of the oxygen vacancy defect in the case of d^0 MOs is given in the forthcoming section. Since MoO_3 is an example of d^0 MO, due to the oxygen vacancy defect, the fermi level moves closer to the conduction band edge, thereby reducing the work function to a value of 6.2 ± 0.2 eV at standard temperature and pressure [17]. Hence, for an assembled asymmetric MnO_2//MoO_3 supercapacitor, an operating potential window of only 1.8 V can be achieved [81]. It is reported that the chemisorption of the hydroxide ion and the proton on the surface of MO electrodes may further extend the potential window by changing the work function [81].

5. Factors affecting the work function of electrode materials

5.1. Effect of oxidation states

While preparing the supercapacitor electrodes by different research groups, there have been inconsistencies in the reported values of the work function for transition metal oxides (TMOs)/other active materials. This is noticeable in the studies done by Henrich and cox on TMOs, though their research focus was not supercapacitor electrode materials [118]. This inconsistency owes its origin to a number of factors like multiple oxidation states, stoichiometry, surface chemistry, different preparation methodologies and the degree of purity. However, for TMOs, a general correlation has been observed by Mark et al. in their studies [17]. They found that as a metal's oxidation state increases, its work function tends to increase as well. This is also shown in Fig. 7. It is found that the drop in work function with the oxidation state happens for two reasons:

i) Lowering the oxidation state changes the electronegativity of the transition metal, which in turn brings a change in the electrochemical potential of the metal oxide and.

ii) Certain defect states within the bandgap (E_g) of these MOs act as donor levels to the conduction band, thereby shifting up the fermi level (towards vacuum). This, in turn, reduces the electrochemical potential.

These factors are discussed in detail in the following sections to help the reader understand the mechanism and energetics of the operation of the supercapacitors made of these TMOs as electrode material.

The first factor, which is the contribution of cation's electronegativity, is common to all TMOs and is discussed separately in the following subsection. The second factor, which is the contribution of defect states, is only specific to those TMOs where oxygen vacancy defect states are formed within the bandgap of the oxide. This is general to all d^0 transition metal oxide. The d^0 oxides are wide bandgap material in which the valence band maximum is comprised of O 2p states while the conduction band minimum is made up of metal d states [119]. The reason why they are called d^0 oxides is that the transition metal in these oxides is fully oxidized with their outer orbital, the d band, is completely empty. The scientific community studied several of these d^0 TMOs like MoO_3 [120], WO_3 [121], V_2O_6 [102], TiO_2, ZrO_2, etc., since they can be used as a charge injection buffer layer in various organic electronics.

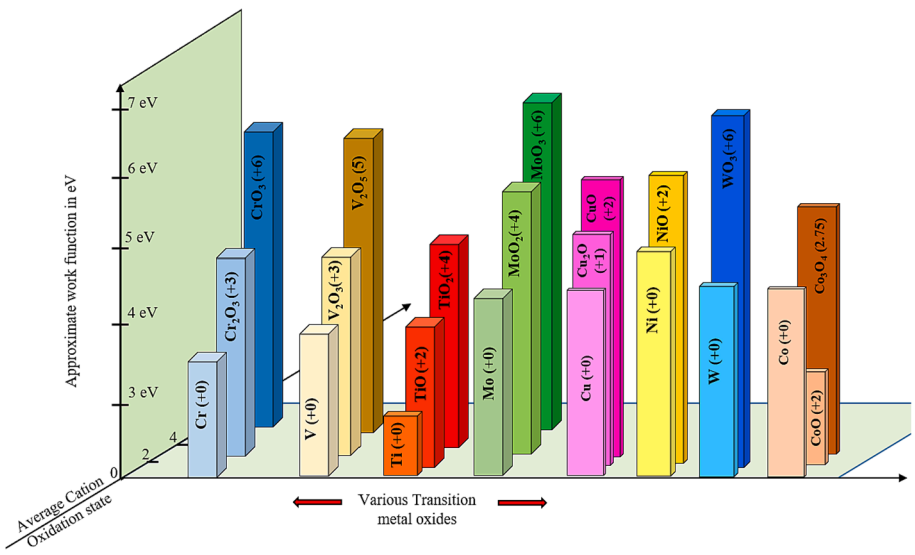

Fig. 7. Bar chart showing an increasing trend of work function with an increase in the oxidation state of several TMOs cations. These oxides have been grown as a thin film via in-situ oxidation [17].

5.2. Influence of electronegativity

In this subsection, we review the effect of electronegativity on the work function of the supercapacitor electrode materials, specifically the pseudocapacitive TMOs, and discuss how severely the electronegativity of the element controls its work function. It has been known for a very long time that a linear relationship exists between electronegativity and the work function of a metal. This is known as Gordy-Thomas relations [122]. They proposed an empirical relation of the form

$$\chi_{PG} = 0.44\phi_{exp} - 0.15 \tag{7}$$

where χ_{PG} is the proposed Thomas Gordy electronegativity, empirically derived in Pauling units and ϕ_{exp} is the experimentally obtained work function. Mulliken also theorized electronegativity as the mean of first ionization energy (IE) and electron affinity (EA) [123,124], as shown in Fig. 8(a). In pseudocapacitive metal oxides or other semiconductors form conduction bands and valance bands with a band gap in between. The first IE is given by the valence band maxima (VBM) while the conduction band minima (CBM) represents the EA [124]. Thus, by Mulliken's concept, the electronegativity should lie at the mid-gap position between VBM and CBM. For an undoped semiconductor, the fermi level lies in the exact center of the bandgap. Even when the effective mass of the electrons and holes differ by orders of magnitude, there is only a slight deviation in the fermi level from the mid-gap position in the bandgap [125]. Hence fermi level could be easily approximated for Mulliken's electronegativity for an undoped semiconductor. Indirectly, for metal oxides, the electronegativity of the central atom governs its fermi level. Going forward, Fig. 8(b) explains how Nethercott's electronegativity can be written for a binary compound, which has a cation and an anion (like metal oxides/hydrides/nitrides) [126]. It can be represented as a geometric mean of the electronegativity of cation and the anion. The fermi level (which in turn relates to the work function) of the compound can be empirically equated to this obtained electronegativity. This information is very useful in the modeling of work function during a redox reaction [17].

A review of the published articles in this direction [126–130] reveals that the work function did possess some linear empirical relationship with the electronegativity of the host element. This is very much understandable since.

- the work function is a measure of the minimum energy required to **pull out an electron** from the solid bulk (fermi level) to outside its surface, [131]

whereas,

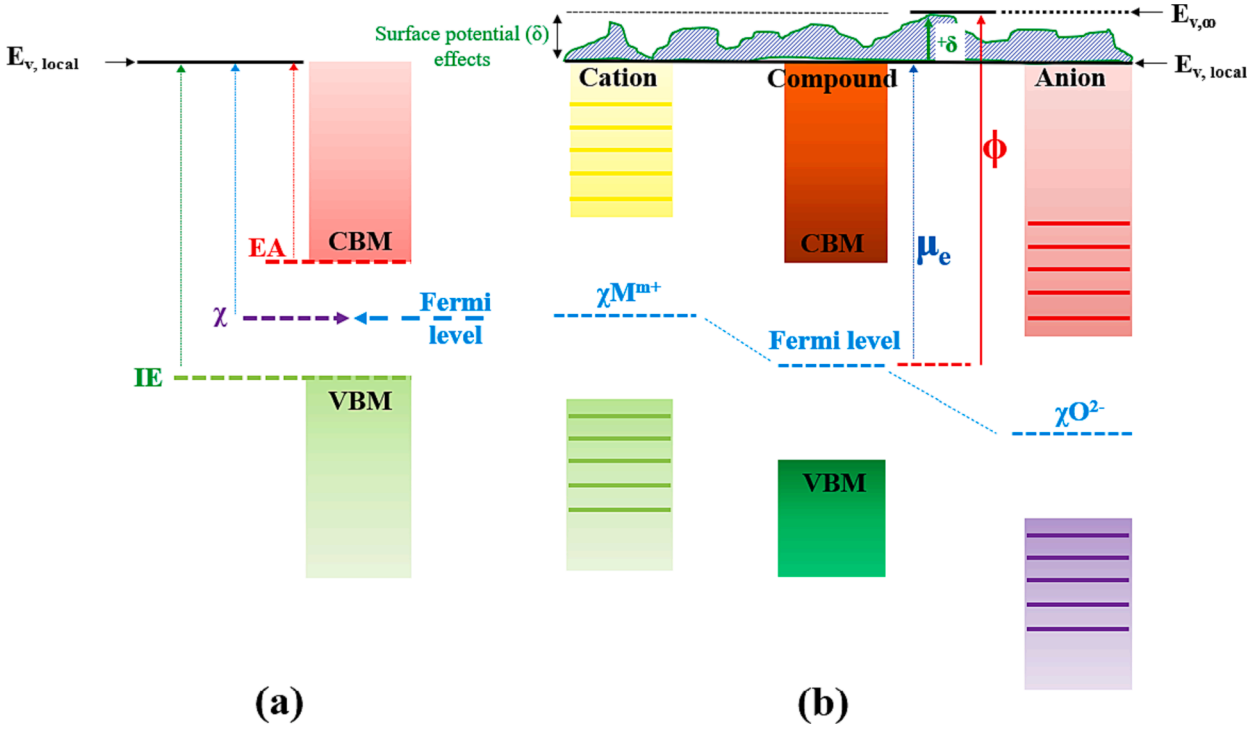

Fig. 8. (a) Shows electron affinity (EA), first ionization energy (IE) and Mulliken's electronegativity (χ) schematically with respect to the energy at the vacuum level. For a semiconductor, fermi level can be approximated to the electronegativity value. (b) shows group χ for a metal oxide/compound (electrode active material) and its equivalence to the fermi level. It also shows how group χ is related to fermi level, electrochemical potential, surface potential and the local work function of the electrode active material.

- electronegativity is a measure of the **attraction between a valence (outer) electron** and an atom's nucleus [132].

Once a transition metal starts to reduce, its oxidation number decreases. The newly accepted electrons add to the shielding effect (σ). Thus effective nuclear charge (Z*) which is given by the relation $Z^* = Z - \sigma$ (where Z is total nuclear charge), tend to reduce for the outer most valence electrons [133,134]. As the charge is reduced, the pull force from the nucleus to the valence electron decreases, which is reflected by a decline in its electronegativity value. Thus, pulling out the valence electron becomes easier, reducing the electron's chemical potential and reducing the work function.

5.3. *Influence of crystallographic orientation, surface termination and roughness*

Though the major factors affecting the work function in pseudocapacitive materials are their oxidation states and electronegativity of the central atom, some morphological factors like crystal orientation, surface termination and roughness also alter the work function to certain extent.

Titanium dioxide (TiO_2) has been a popular choice of pseudocapacitive material for almost a decade now [135,136]. Some studies have been published suggesting its work function dependency on its crystallographic orientation. Kashiwaya et al. have studied the anatase (0 0 1), anatase (1 0 1), rutile (1 1 0), and rutile (0 0 1) phases of TiO_2 for its work function [137]. In the anatase phase of TiO_2, the terminal crystallographic planes of (0 0 1), (1 0 1) and polycrystalline surface showed a work function of 4.70, 4.62, and 4.51 eV, respectively. This minor variation in the work function was attributed to the change in the oxygen vacancy concentrations for the different planes of the anatase phase, which correspondingly altered the ionization potential and the fermi level within the bandgap of TiO_2, resulting in the variation of the work function. Other pseudocapacitive materials like zinc oxide (ZnO) have also been studied for their dependency of work function on its crystallographic orientation [138,139]. Moormann et al. studied the hexagonal wurtzite

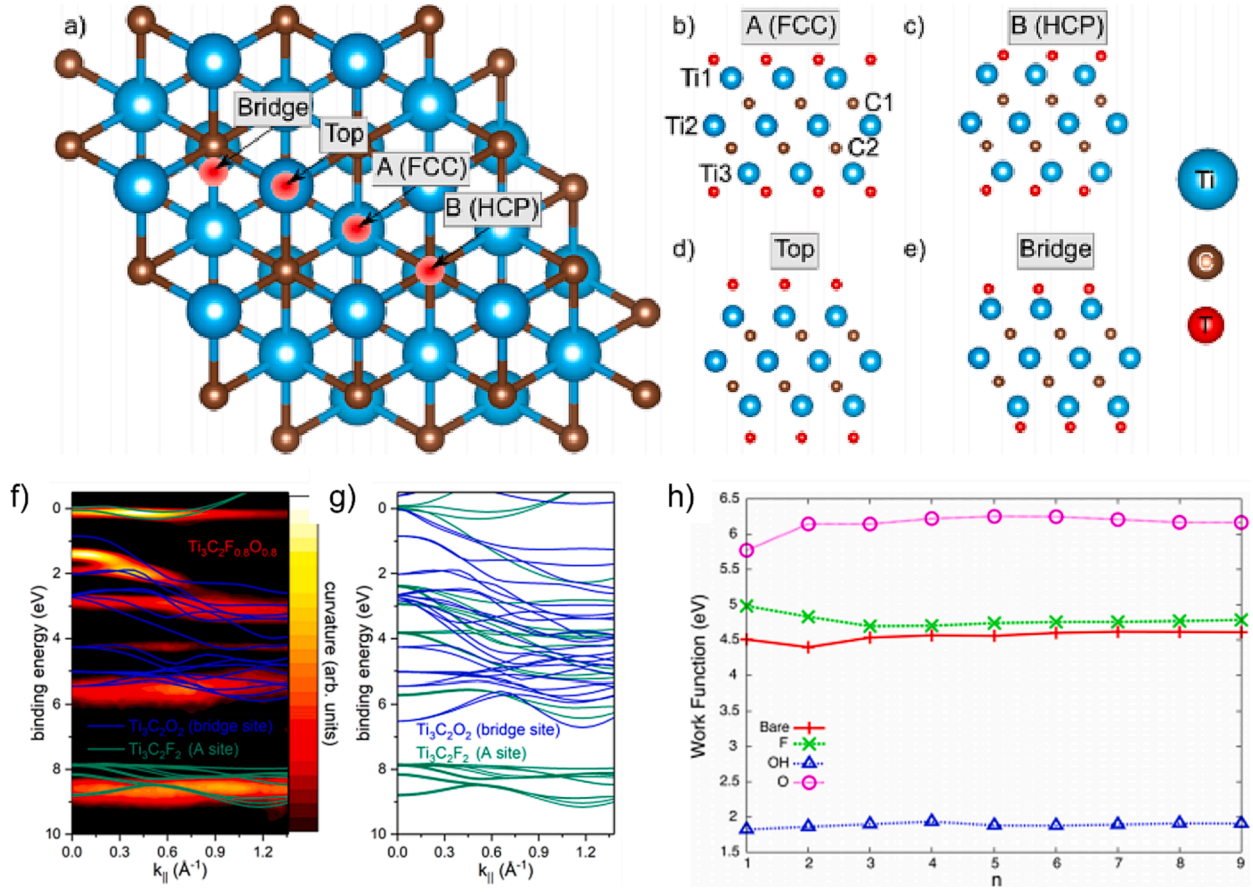

Fig. 9. Schematic illustration of different adsorption sites in $Ti_3C_2T_x$. (a) Top view of $Ti_3C_2T_x$. (b) Side view of the adsorption site of A(FCC) position (third atomic layer, top of the Ti atom), (c) Side view of the adsorption site of B(HCP) position (second atomic layer, top of carbon atom), (d) Side view of the top adsorption site (first atomic layer, top of Ti atom), (e) Side view of the bridge adsorption site (between the topmost Ti and C atom). (f) and (g) Measured ARPES curvature spectrum and band strength calculation of $Ti_3C_2F_{0.8}O_{0.8}$, $Ti_3C_2O_2$ and for $Ti_3C_2F_2$. Reproduced with permission copyright 2019 [141]. (h) work function of bare and functionalized $Ti_{n+1}C_n$ with -F, –OH and -O surface terminations for the MXene. The n represents the number of C atoms. Reproduced with permission copyright 2015 [142].

structure of ZnO for its three low indexed planes and named it as zinc face (0001), prism face (10 $\bar{1}$ 0), and oxygen face (000 $\bar{1}$) [140]. Using a Kelvin method (vibrating gold wire), the work functions were measured for zinc face (4.25 eV), prism face (4.64 eV), and oxygen face (4.95 eV). Again, a minor variation is observed due to the changes in crystallographic orientation.

Similar to crystallographic orientation, surface terminations by various moieties also impact the work function of a material. MXene, a newly discovered material, is now gaining popularity for its superior pseudocapacitive properties and low electronic resistance due to its high metallic behaviour [143]. MXenes belong to the family of 2D transition metal carbides and nitrides and have been studied for their surface termination dependency of work function. Shultz et al. investigated the electronic properties of $Ti_3C_2T_x$ using a combination of ultraviolet photoemission spectroscopy (UPS), X-ray photoelectron spectroscopy (XPS), and inverse photoemission spectroscopy (IPES) [141]. First Ti_3AlC_2 was etched using a mixture of LiF and HCl to introduce the F terminations. Further, the samples are annealed at different temperatures and the adsorption sites of the surface terminations. Fluorine was found to be occupying the face-centered cubic adsorption site A(FCC) and oxygen initially occupied the bridge site and the hexagonal closed packing site B(HCP), as shown in Fig. 9 (a-e), followed by a rearrangement to the face centered cubic side after F desorption at the higher annealing temperatures. Using the angle resolved photoemission measurements (ARPES), as shown in Fig. 9 (f), a good agreement was obtained between the calculated band structure and a dispersion of more than 1 eV depending on the surface termination. While annealing the samples, the work function increases from 3.9 eV to 4.8 eV due to the desorption of water, carbon-dominated contamination and hydroxyl (OH) species, but decreases again to 4.1 eV at elevated temperatures due to F desorption. In a similar density functional theorem (DFT) based study performed by Khazaei et al., three types of surface terminations (-O, –OH, and -F) were studied for MXenes [142]. It was found that OH terminated MXenes exhibit ultra-low work function of 1.6 eV to 2.8 eV. Also, depending on the type of transition metal and the amount of C in the MXene lattice, the functionalization of F and O modulate the work function. This is shown in Fig. 9 (g). As discussed previously, this change in the work function was linearly proportional to the change in the surface dipole potential associated with each functional group. This study showed that the work function for -F and -O terminated MXenes is controlled by two factors: a) the induced dipole moment due to charge transfer between F/O and the substrate and b) the change in the dipole moment due to surface relaxation upon functionalization. However, in the case of –OH group, in addition to the above two factors, the intrinsic dipole moment of the –OH also affects the surface potential, thereby affecting the work function.

Though, to some extent, surface roughness affects the work function of the electrode structure, the effect seems to be very minimal, of course, dependent upon the degree of roughness. A pseudocapacitive material, Indium tin oxide (ITO), popularly known for making transparent electrodes, was studied by Lin et al. for the correlation between surface roughness and its work function [144–146]. A KrF excimer laser was irradiated for 25 mins on an ITO-coated glass substrate, reducing the root mean square surface roughness (R_{rms}) value from 1.04 nm to 0.51 nm. This reduction in the surface roughness after the laser irradiation also correlated to an increase in the work function. An as-cleaned-unexposed sample exhibited a work function of 5.02 eV, while the 25 mins irradiated sample showed a work function of 5.15 eV. Quite similar results were also observed by Li et al. when they used copper substrate and created different surface roughness using silicon carbide sandpapers and alumina slurries [147]. Their findings suggest that as the roughness increases from 10 nm to 100 nm, the work function value dipped from 4.76 eV to 4.53 eV. It was theoretically demonstrated that the surface roughness could reduce the average work function. However, fluctuations in the local work function tend to increase with increasing the surface roughness. Such fluctuations could be attributed to the formation of microelectrodes onto the surface having their own dipole potential, which could alter the existing surface potential.

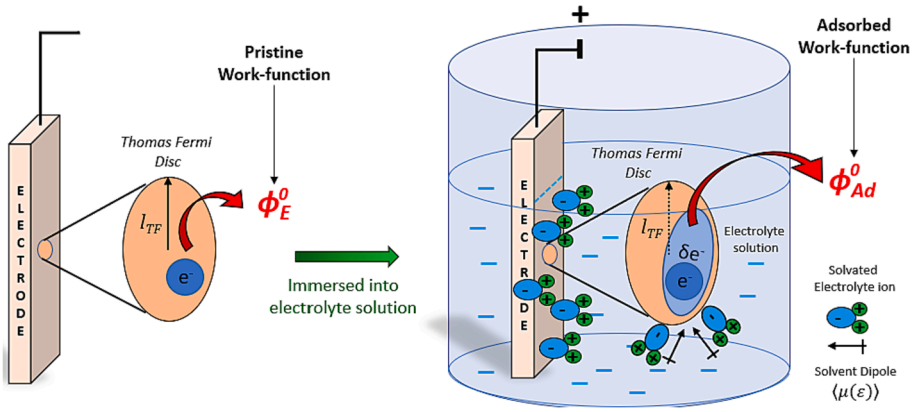

Fig. 10. Schematic showing how the work function of the electrode changes when dipped into an electrolyte solution. The electrode's pristine work function (ϕ_E^0) has been derived from the self-capacitance of an assumed Thomas Fermi (TF) disc (at the electrode's surface) having the radius given by screening length (l_{TF}). Once the electrode is immersed into the electrolyte solution, the solvated electrolyte ions (having the dipole moment $\langle\mu(\varepsilon)\rangle$) get adsorbed onto the surface of the electrode and the effective work-function is now modified to "Adsorbed Work-function" ($\Delta\ \phi_{ad}^0$).

5.4. Effects of electrolyte adsorption: Work function of immersed electrodes

When two different phases are in contact, there is a subsequent moderation in the interfacial properties of these two phases, e.g., an electrode immersed in a water-based electrolyte or any liquid/solid electrolyte [148,149]. One of the key features to be modified is the electronic work function. The reason for this modification is the solvated ions that are adsorbed on the surface of the electrodes [150–152]. Therefore, in electrochemical systems, the effective work function that controls the charge transfer is that of an electrode with ions adsorbed (ϕ_{ad}). This change in the work function is generally attributed to two aspects: i) the adsorbed solvated ions may possess a permanent or induced dipole moment, and ii) a redistribution of the electron density of the surface atoms of the electrodes due to the induced field of adsorbed species [153,154]. The first change happens on the electrolyte side of the interface, while the second change occurs on the electrode side of the interface. This concept of the field-dependent orientation of the dipoles [155,156] and its effect on the dielectric constants have been extensively studied for water-based adsorbates [157,158]. Kaur et al. have presented a model to formulate the work function of immersed electrodes for different shapes and morphologies [159]. It would be interesting to look at this model before trying to understand the energy interactions of supercapacitor electrodes with electrolyte during operation.

When an electrode comes in contact with a different phase electrolyte, the energy expense for the electron exchange gets modified for the electrode due to the surrounding electrolyte, as shown in Fig. 10. Therefore, for an immersed planar electrode with an adsorbed solvated ion, the adlayer modifies the work function (ϕ^0_{ad}) and can be written in terms of interface-induced correction ($\Delta\ \phi^0_{ad}$) as follows:

$$\phi^0_{ad} = \phi^0_E + \Delta\,\phi^0_{ad} \tag{18}$$

In the above eq., ϕ^0_E is the work-function of the pristine (non-immersed) electrode. To model, the interface-induced correction ($\Delta\ \phi^0_{ad}$), it needs to comprehend the combined effect of:

(i) Orientation of the solvent dipoles (with the assembly of solvated ions) adsorbed on the surface of the electrode (solution side of the interface).
(ii) Eelectron density redistribution of the surface atoms (electrode side of the interface) due to the influence of adsorbed solvent dipoles [153,154].

Both these effects have their own potentials, which are likely to be opposite in nature, as the effect (ii) is induced by the effect (i) and therefore opposing in nature. If the change in potential of surface atoms of the electrode due to electron density redistribution is given by $\delta\,\chi^M_0$ and the potential modification due to adsorbed solvent dipoles is represented by g^0_s, the interface induced correction ($\Delta\ \phi^0_{ad}$) for a submerged electrode can be given as:[153]

$$\Delta\,\phi^0_{ad} = \delta\chi^M_0 - g^0_s \tag{19}$$

Hence eq. (8) can be written as

$$\phi^0_{ad} = \phi^0_E + \delta\chi^M_0 - g^0_s \tag{20}$$

Therefore, the work function of an immersed electrode (with adsorbed solvated ions) ϕ^0_{ad} is a combined effect of three terms as shown in the above equation (Eq. (20).

6. Voltage window in metal oxide-based pseudocapacitors

As we have discussed previously, pseudocapacitors are a class of supercapacitors that operate on the mechanism of charge storage via faradaic reaction. These faradaic reactions often involve interactions of the work function of the anode and cathode. During the oxidation and reduction processes, multiple mechanisms could play a role in determining the fermi levels of the electrodes, thereby modulating the work functions of individual electrodes. This, in turn, governs the running voltage window. To better understand this energy interaction, we have chosen an asymmetric system of MnO_2//MoO_3 based supercapacitor.

6.1. Energetics of supercapacitor electrodes in Operation: MnO_2//MoO_3 system

So far, we have reviewed the energetic aspects of the isolated electrodes or electrodes in contact with the electrolyte. In this section, we review how the energetics change as the supercapacitor operates.

Since this review focuses on the working mechanism of high voltage asymmetric supercapacitors, which generally operate via pseudocapacitance, we discuss the studies focused on asymmetric supercapacitors made using one of the most commonly used transition metal oxide MnO_2 as the positive electrode material and MoO_3 as the negative electrode material.

The rationale behind selecting MoO_3 is that in a d^0 transition metal oxide, as previously stated, the two underlying mechanisms causing the reduction in the work function are:

(1) Lowering of electronegativity when the reduction process (redox) starts, as shown by Nethercott's postulate [126]. This happens because of the increase in the concentration of the lower electronegative cations as the redox reaction proceeds.
(2) Effects of the defect states present in between the bandgap of d^0 TMOs because of oxygen vacancy formation, which acts like donor levels shifting the Fermi level up, thereby reducing the work function [119]

Since Mn in MnO_2 does not come in the category of d^0, it only works by the first mechanism, i.e., while performing the redox reaction, a change in electronegativity of the transition metal ion alters the fermi level, thereby altering the work function, which was given by Nethercott's postulate [126]. However, MoO_3 performs its redox reaction via both the mechanisms (1) and (2). So, in this section, we will be discussing both of these mechanisms in detail through a modeling study done by Mark et al. [17].

6.1.1. Redox process in a d^0 metal oxide electrode: MoO_3 as the anode

When a pseudocapacitor with MoO_3 as one of the electrodes starts to function, it is driven by a rapid redox reaction on the MoO_3 electrode [81]. As MoO_3 starts to reduce to a lower oxidation state, say $MoO_{(3-x)}$, the molybdenum cation Mo^{+6} starts to convert to a state, say $Mo^{+(6-2x)}$. Both mechanisms (1 and 2) kick in, but the mechanism (2) dominates in the initial phase. Hence, along with this reduction of the Mo ion, oxide ions (O^{2-}) are removed rapidly in the initial phase (creating oxygen vacancies) from the lattice and the ingested electrons of the molybdenum ion start partially filling the 4d band of Mo^{+6} ion (which was previously empty). Thus, new gap states (defect state/donor state) seed in the bandgap and start to grow [160]. These gap states become more and more prominent and increase their energy. As a result, the fermi level moves up and gets closer to the conduction band, which causes a reduction in the work function. Let the reduction in the work function because of the development and growth of these donor states be represented as $\Delta\phi_d$.

While mechanism (1), which is a decline in the overall electronegativity, keeps working parallel to the mechanism (2), its effect on the overall work function is less prominent during the initial phase. From the previous discussion, it has been observed that the decline in electronegativity means raising the Fermi level, thereby reducing the work function ($\Delta\phi$). So, when MoO_3 gets reduced to $MoO_{(3-x)}$, let the reduction in the work function because of the increased concentration of lower electronegative molybdenum cation be equal to $\Delta\phi_\chi$. Now, if ϕ_0 represents the initial work function of the MoO_3 as a stoichiometric oxide, the work function, ϕ, during the reduction process account for both mechanism (1) and (2), which is given by

$$\phi = \phi_0 + \Delta\phi_\chi + \Delta\phi_d \tag{28}$$

The combined effect of these two mechanisms on the work function of MoO_3 during the reduction process has been shown in Fig. 11 [17]. It can be seen that the overall work function decreases exponentially in the initial phase due to the dominating effect of mechanism (2), i.e., the oxygen vacancy formation (oxygen deficiency), but later decreases with constant slope when mechanism (1) takes over as the mechanism (2) becomes feeble.

In eq. (8), we can derive expressions for $\Delta\phi_\chi$ and $\Delta\phi_d$, which would relate them to the degree of non-stoichiometry due to which there is a change in the overall work function. Using the Kröger-Vink notation and Nethercott postulates, Mark et al. [17] estimated the value of as $\Delta\phi_\chi$ as:

$$\Delta\phi_\chi = \left(\left(\chi_{Mo}^{+6}\right)^{1-2x} \left(\chi_{Mo}^{+5}\right)^{2x} \left(\chi_{O}^{2-}\right)^{3-x} \right)^{1/(4-x)} \tag{32}$$

In the above equation, x represents the degree of reduction/oxygen deficiency, χ_{Mo}^{+6} is the electronegativity of Mo^{+6} ion, χ_{Mo}^{+5} is the

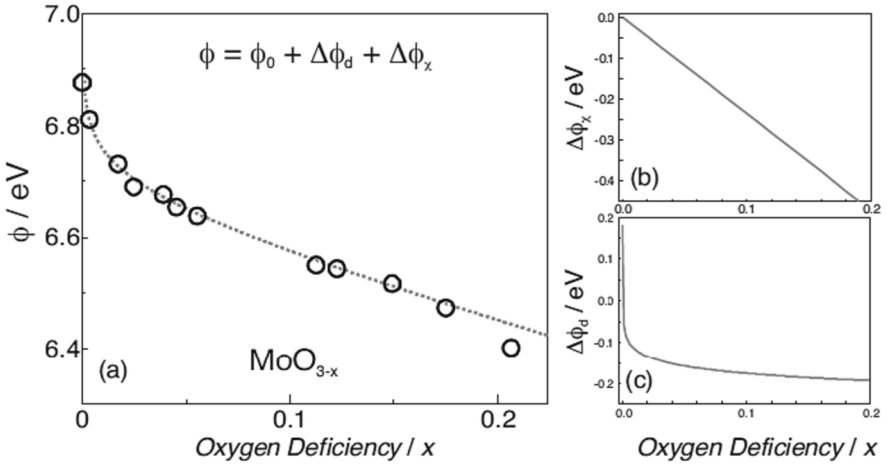

Fig. 11. A drop in the work function value, as MoO_3 or any d^0 TMOs starts to reduce; (a) combined effect of the drop in work function because of the exponential drop, as oxygen vacancies are formed during reduction, which is individually shown in (c) and constant gradient drop because of an increase in the concentration of lower electronegative cation, which is individually shown in Fig. 11 (b). Image reproduced with copyright reference [17].

electronegativity of Mo^{+5} ion, and χ_O^{2-} is the electronegativity of oxygen anion. The above eq. (32), $\Delta\phi_\chi$ vs. $\times$, has been plotted in Fig. 11(b) and it shows a pretty linear drop with a constant slope. Now in order to determine the overall work function, since MoO_3 is a d^0 transition metal oxide, the effects of donor states should also be incorporated.

This effect of donor states is very specific to d^0 TMOs. The electronic configuration of Mo is given by $[Ar]sd^{10}4s^24p^64d^55s^1$. The outer electron shells, which are $4d^5$ and $5\ s^1$, are partially filled. When Mo forms MoO_3, the Mo atom goes to the Mo^{+6} ion state, emptying all of the electrons in 4d and 5 s bands. This 4d band, which is now completely empty, forms the CBM. But when this Mo^{+6} (in MoO_3) starts to reduce to Mo^{+5} as the doubly positive oxygen vacancies start to appear, the ingested electrons again start to fill in the low-lying $4d^0$ bands, forming the donor states. These donor states shift the fermi level closer to the vacuum, thereby reducing the work function. Fig. 12 shows the schematics of the upward movement of the fermi level as the donor states start to appear during the reduction process.

In order to explain their model, Mark et al. [17] have developed a series of equations on the basis of the reduction of MoO_3 and the appearance of the defect band in the bandgap of MoO_3. After a series of deductions, they have been able to derive a relationship between changes in the work function with respect to oxygen vacancy generation. This is given by

$$\Delta\phi_d = \frac{-1}{2}kT\ln\left(\frac{x}{x_0}\right) \tag{33}$$

where, x = oxygen deficiency in the reduced oxide, x_0 = oxygen deficiency in the reference oxide (i.e. MoO_3), k is the Boltzmann constant and T is the absolute temperature. Now we can combine eq. (28), (32) and (33) and write the general work function for MoO_3 as the supercapacitor operates as

$$\phi = \phi_0 + \left(\left(\chi_{Mo}^{+6}\right)^{1-2x}\left(\chi_{Mo}^{+5}\right)^{2x}\left(\chi_O^{2-}\right)^{3-x} \right)^{1/(4-x)} + \frac{-1}{2}kT\ln\left(\frac{x}{x_0}\right) \tag{34}$$

As described in Fig. 11 (a), this work function for MoO_3 shows an exponential drop during the initial phase when the defect state pushes the fermi level closer to the conduction band (CB) rapidly **(Mechanism 2)** but later attains a constant gradient drop as the declining group electronegativity pushes the fermi level further closer to CB **(Mechanism 1)**.

A supercapacitor may employ two TMO electrodes with a large work function difference. For example, theoretically, MnO_2 (ϕ = 4.4 eV) as the positive electrode (cathode) and MoO_3 (ϕ = 6.9 eV) as the negative electrode (anode) should give a large work function difference of 2.5 V [81]. However, due to the oxygen vacancy defect in MoO_3, its work function drops to 6.2 eV [81]. Hence, following eq. (6) we can make a supercapacitor device with 1.8 V potential window using these two electrodes. However, once the energy levels

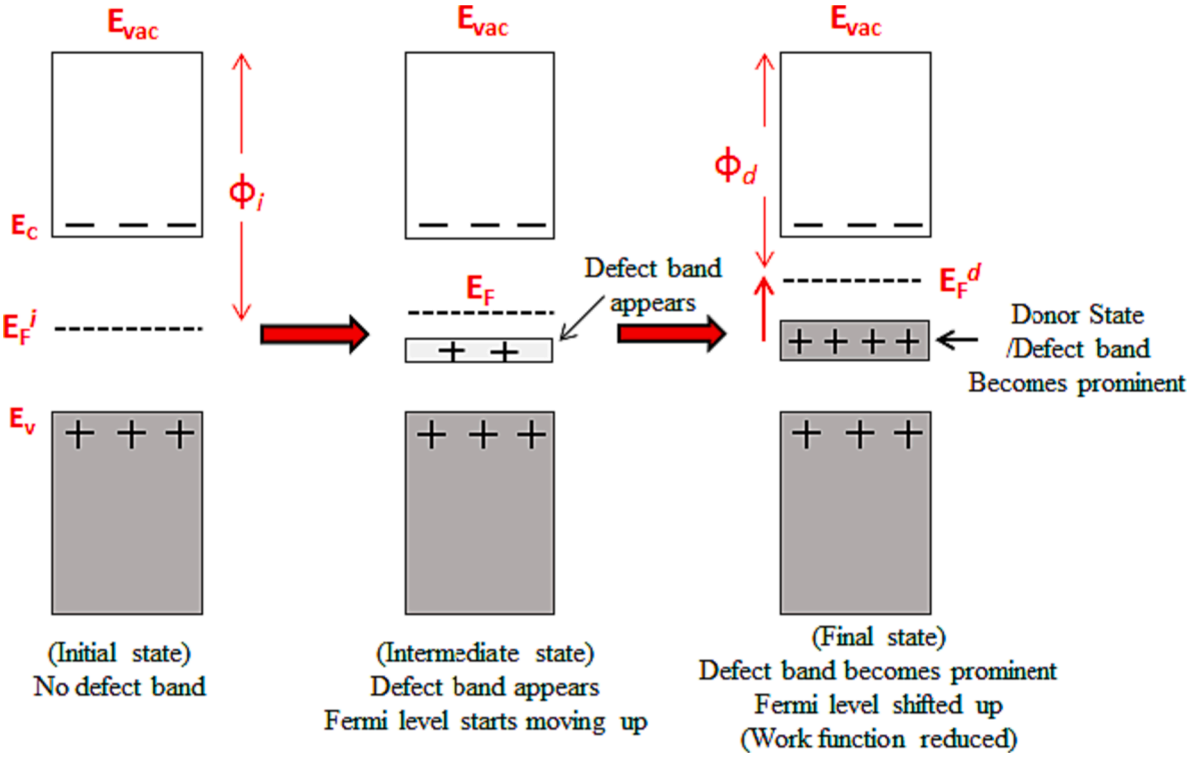

Fig. 12. Schematics of the upward movement of the Fermi level towards the conduction band as the donor states start to appear because of the formation of oxygen vacancies during the reduction process.

and slower diffusion kinetics of electrolytes come into the picture, this voltage window can again be expanded due to overpotential effects, which is discussed in the following sections.

6.1.2. Redox process in a non-d^0 metal oxide electrode: MnO_2

When MnO_2 is used as an example electrode (cathode), its work function will increase (contrary to MoO_3, where it reduces) as the supercapacitor starts to discharge. As we have explained the model for change in the work function of MoO_3 in section 6.1.1, we can also develop a model for MnO_2. Since MnO_2 is not a d^0 metal oxide, it should only follow Mechanism 1 while increasing its work function. So $\Delta\phi_d = 0$, for MnO_2 electrode, and only $\Delta\phi_\chi$ and ϕ_0 would be needed to model the overall work function ϕ, which could be modeled as discussed in section 6.1.1. As a result, when the supercapacitor discharges, the work function of the MnO_2 electrode (positive electrode) increases only linearly, following eq. (32), as shown in Fig. 14 [161]. However, before starting the discussion about the charge/discharge mechanism of MnO_2, it is necessary to discuss all other aspects that directly affect them, like crystal structure, gap states and electrolyte ion interactions.

MnO_2 exists in several crystallographic forms like α, β, γ, and δ [163]. All of these allotropic forms consist of a series of MnO_6octahedra as the building blocks arranged in a different fashion in different allotropic forms. This MnO_6octahedron consists of an

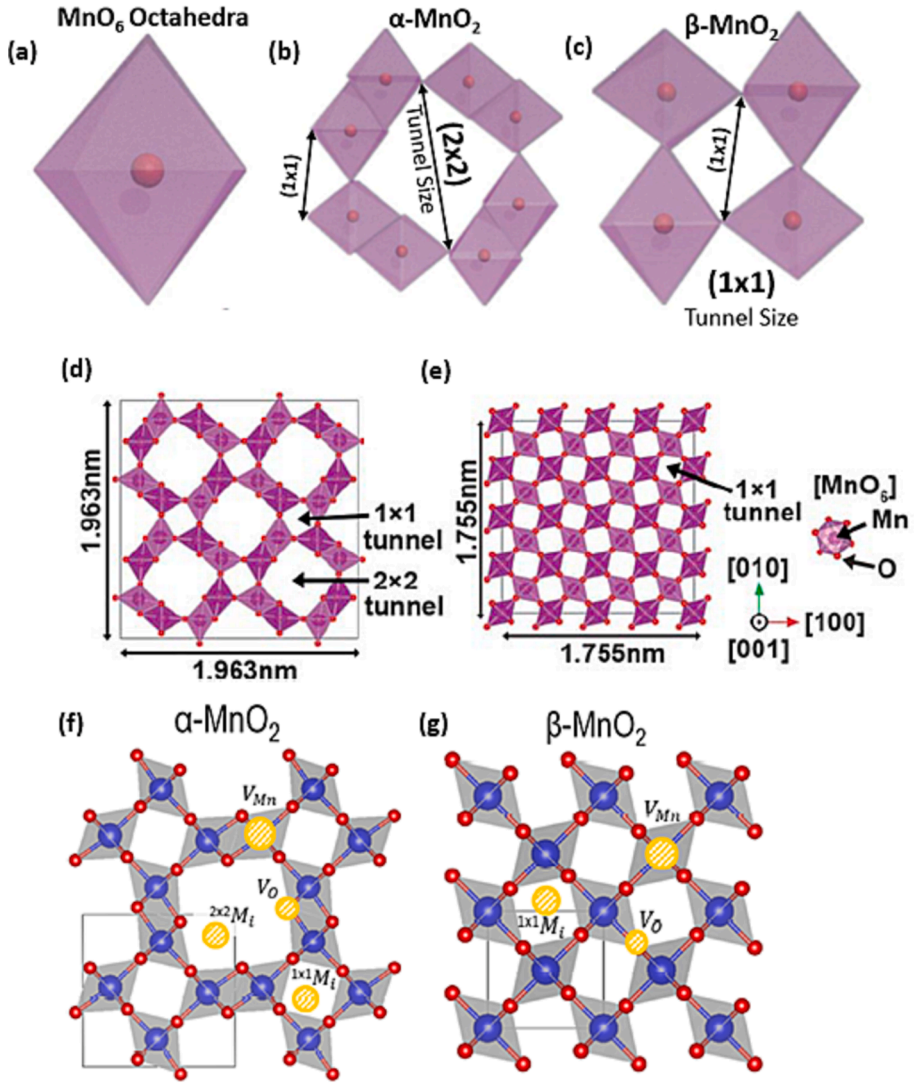

Fig. 13. (a) MnO_6 octahedra with Mn atom at the center and O atom at six corners of the octahedra. (b) Double edge-sharing octahedra to form (2 × 2) tunnel in α-MnO_2. (c) Single edge-sharing octahedra to form (1 × 1) size tunnel in β-MnO_2. [(a) (b) and (c)Reproduced with permission from [162] copyright 2015. (d) and (e) Space lattice for α and β MnO_2, respectively. This formation shows that α-MnO_2 possesses both (1 × 1) size and (2 × 2) size tunnels. (f) Interstitial (M_i) and Vacancy (V_{Mn} & V_O) mechanism by which electrolyte cations like H^+, Li^+, Na^+, K^+, NH_4^+, etc., intercalate and de-intercalate in α-MnO_2. (g) Interstitial (M_i) and Vacancy (V_{Mn} & V_O) mechanism by which electrolyte cations intercalate and de-intercalate β MnO_2. (f) and (g) reproduced with permission from [161] copyright 2015.

Mn atom at the center and 6O atom at six corners of the Octahedra, as shown in Fig. 13 [162]. The Order in which MnO_6octahedra are piled up makes one, two, or three-dimensional structures with connected interstitial spaces as "tunnels" through the structure. The size of these tunnels is characterized by the number of subunits of MnO_6octahedra in the form of ($m \times n$). When MnO_2 is used as an active electrode material, these tunnels provide a good pathway for intercalation/deintercalation of the electrolyte cations like H^+, Li^+, Na^+, K^+, NH_4^+, Ba^{2+} or H_3O^+ [164]. During the charge–discharge of the supercapacitor electrode, once these ions intercalate into the interstitial spaces via these tunnels or at vacancy/substitutional sites in the MnO_2 lattice, their electronic levels start to interact with those of the host MnO_2 within its band-gap (E_g). Therefore, these electronic levels are termed as gap states (or charge switching states), very similar to those of defect states of MoO_3.

As MnO_2 starts to undergo oxidation, an increase in its work function results, as discussed previously. As per the studies done by Young et al. [161], during the redox activities of MnO_2 (α, β, and γ), the electrolyte cations intercalate and de-intercalate in its lattice. Using the density functional theory, these cations were incorporated as extrinsic impurities and were modeled using solid-state defect theory. This helped in the identification of the cation-induced electronic levels that were occurring within the bandgap (E_g) of the MnO_2. These cations induced electronic levels (which are shown in Fig. 14 as E_1^0, E_2^0, and E_3^0) are able to accept and donate electrons as the externally applied potential shifts the fermi level (ε_f) above and below the charge-switching potential of these electrolyte ions. Fig. 14 (a) also shows a conductive current collector with its work function as eϕ also lying somewhere in between the E_g of the active material MnO_2. The electrolyte has also been shown to have a known potential stability range beyond which either it oxidizes or reduces. Hence, the operable potential lies in the range where the electrolyte stability window overlaps with the E_g of the active material, MnO_2. These cations induced electronic levels (charge-switching states E_1^0, E_2^0, and E_3^0) are broadened as they interact with the surrounding energy levels and give out almost a linear relationship between the potential of the electrode and the charge transferred, with a constant capacity. This is shown in Fig. 14 (b).

Fig. 15 represents a hypothetical elucidation of the work-function-based voltage window of an operational asymmetric supercapacitor. It is hypothetical because it is drawn without considering any energy interaction of electrodes with electrolyte and overpotential effects. However, it shows the ideal electrode work function-based voltage window during the first discharging half cycle. Fig. 15 (a) shows the initial state of supercapacitor electrodes at their open-circuit potentials. The voltage window at this state is only attributed to the difference in their work function. Once the supercapacitor starts to discharge, an intermediate state having a smaller voltage window results, as shown in Fig. 15 (b). Upon discharging further, it reaches a state where the work function of two electrodes becomes equal and the voltage window is theoretically zero. This is the state of a fully discharged supercapacitor, shown by Fig. 15 (c), where two electrodes are now in thermodynamic equilibrium ($\Delta G = 0$, G is Gibb's free energy).

6.2. *Voltage window in various asymmetric pseudocapacitor*

In this section, we discuss the high voltage asymmetric supercapacitors (ASCs) fabricated with wide work function difference metal

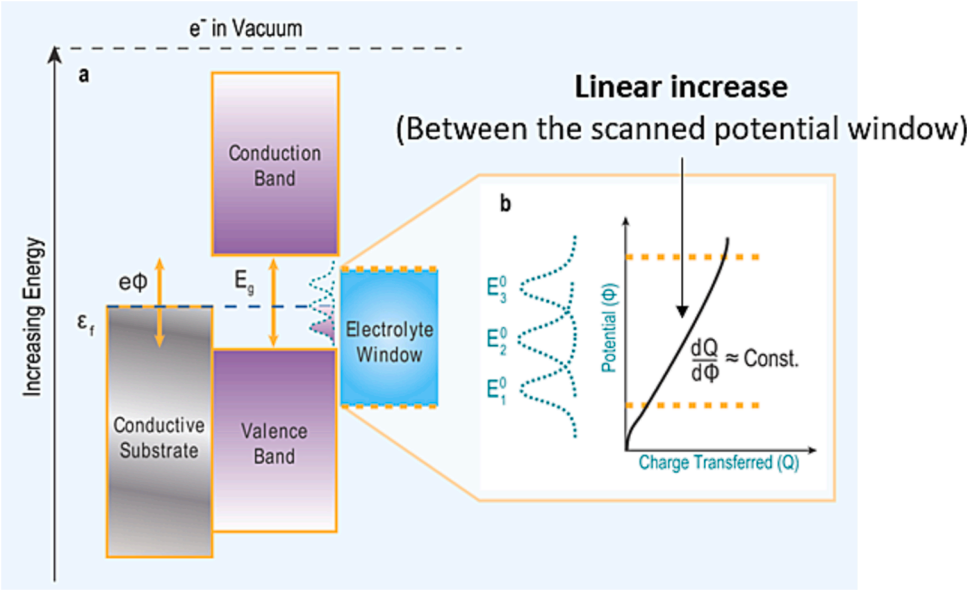

Fig. 14. (a) Band diagram of a functioning supercapacitor electrode, with energy levels of electrolyte and current collector. The charge-switching states E_1^0, E_2^0, and E_3^0(similar to the defect states of MoO_3) induced by intercalating electrolyte ions like H^+, Li^+, Na^+, and K^+ into the bandgap of MnO_2. (b) As the voltage sweeps across the potential window of the electrolyte, the charge-switching states get activated and deactivated. In this process, only a linear relationship is observed between the potential increase and the charges transferred to the electrode. Reproduced with permission from [161] copyright 2015.

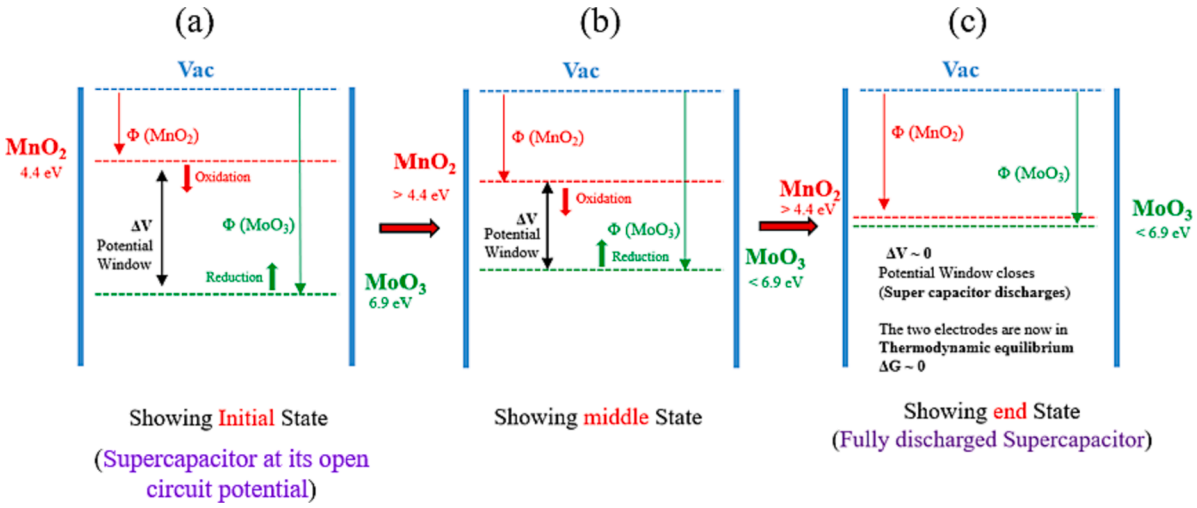

Fig. 15. Schematic representation of a hypothetical asymmetric supercapacitor in operation (without any interaction with electrolyte energy levels). (a) Supercapacitor electrodes at their open-circuit potentials. (b) Intermediate state of discharging, (c) Fully discharged supercapacitor.

oxide (MO) electrodes chosen as cathode and anode. We also briefly discuss the influence of the current collector, overpotential, concentration and pH of the electrolyte on the low or additional potential window obtained compared to the actual work function difference. Most of these high-voltage ASCs have been constructed by wisely choosing either using a low work function cathode material, a high work function anode material, or in some cases, a combination of both [165]. Engineering the asymmetric supercapacitor configuration based on wide work function difference MO electrode materials has proven to be very effective as they were able to deliver a higher voltage range from 1.6 to 2.6 V, which aids in overcoming the low energy density challenges encountered by supercapacitors [166–168]. Typical in ASCs, low work function MOs such as manganese oxides (MnO_2, Mn_3O_4), tin oxide (SnO_2), zirconium oxide (ZrO_2), etc. are employed as cathodes and high work function MOs such as iron oxides (Fe_2O_3, Fe_3O_4), molybdenum oxide (MoO_3), vanadium oxide (V_2O_5, VO_2), bismuth oxide (Bi_2O_3), cobalt oxide (Co_3O_4), etc. are employed as anodes. The metal oxides that store charges via pseudocapacitive mechanism have higher theoretical capacitance and energy density than carbon-based electrodes. The only issue with the metal oxide electrodes is the low electrical conductivity, leading to lower power density than carbon-based electrodes. This issue can also be addressed by making composite electrodes of metal oxide and carbon. At the end of this section, a table (Table 1) comparing the asymmetric supercapacitors fabricated based on a wide work function difference of MOs is also given.

MnO_2, being one of the low work function MOs (4.4 eV), is widely used as a cathode in most high-voltage ASC systems. Apart from being the low work function metal oxide, MnO_2 offers environmental stability, high theoretical capacitance, low cost, and ease of development in various nanostructure forms [169]. The most common ASC system developed with MnO_2 is MnO_2//Fe_2O_3, where a work function difference of 1.4 eV is observed [170–172]. Though this work function difference is not very high, several factors played a key role in obtaining a voltage as high as 2 to 2.3 V in some devices [173–176]. In most high-voltage ASCs developed, the performance of the negative electrode material is inferior to that of the positive electrode material. The charge balance then always depends on increasing the amount of the negative electrode material to match the performance of the positive electrode material. This may cause an increase in the total weight of the supercapacitor. In such cases, improving the electrode's performance via doping, making composites, and developing conductive scaffolds is vital [177,178]. These strategies will eventually lead to a high-performing supercapacitor with charge-balanced high capacitance ASC, where the maximum voltage window goal is achieved by choosing materials with a wide work function difference.

For instance, Fe_2O_3 (5.8 eV) nanoneedle branches on Nickel (Ni) nanotube array template (NiNTA@Fe_2O_3) are developed via the electrodeposition process as a strategy for improving the performance of the negative electrode material [177]. The highly conductive Ni helps in moving the electrons faster to the external circuit. Also, the hybrid core-branch structure developed provides many active sites for charge storage via EDLC and redox reaction. Synergistically, it led to a high capacitance of 418.7F/g at a scan rate of 10 mV s^{-1}. Another strategy for improving the negative electrode material's charge storage capability involves phosphine plasma activation of Fe_2O_3 nanorods [179]. The plasma treatment of Fe_2O_3 nanorods formed an amorphous layer of iron phosphide/phosphate layer on the surface without varying the bulk morphology and composition of the nanorods. The plasma treatment introduced defects sites in the nanorods, which increased the number of charge-storing active sites. This was evident from the electrochemical performance of Fe_2O_3-P nanorods exhibiting a capacitance of 369F/g at a current density of 1 mA cm^{-2}, four times enhancement compared to Fe_2O_3 nanorods (90F/g). In another strategy for developing high-performing negative electrode material, highly conductive nanoneedle arrays made of $NiCo_2S_4$ are used as a scaffold to deposit Fe_2O_3 nanorods [180]. This hierarchical nanostructure provides a vast surface area for pseudocapacitive charge storage with good rate capability. A high specific capacitance of 342F/g was achieved for this hybrid structure at a scan rate of 5 mV s^{-1}. Here MnO_2 deposited on carbon cloth synthesized via hydrothermal route was chosen as the positive electrode material. The presence of carbon cloth as the current collector substrate helps in extending the oxygen evolution

Table 1
Asymmetric Supercapacitors fabricated based on metal oxides with a wide work function difference. *WFD – Work function difference.*

Cathode// Anode	WFD (eV)	Positive electrode	Negative electrode	Current collector	Electrolyte	Voltage window (V)	Ref
MnO_2// Fe_2O_3	1.4	MnO_2	Fe_2O_3	Si/SiO_2	1 M KOH	1.2	[205]
		NiNTA@MnO_2	NiNTA@ Fe_2O_3	Titanium foil	1 M Na_2SO_4	1.6	[177]
		MnO_2	Fe_2O_3 - P	Carbon cloth	1 M Na_2SO_4	1.6	[179]
		MnO_2 NWs	Fe_2O_3 NTs	Carbon cloth	PVA/LiCl	1.6	[172]
		MnO_2	N- Fe_2O_3	Carbon cloth	PVA / LiCl	1.6	[171]
		MnO_2	Ti- Fe_2O_3@PEDOT	Carbon cloth	PVA / LiCl	1.6	[206]
		MnO_2	Fe_2O_3@C	Carbon fabric	PVA / LiCl	1.6	[207]
		MnO_2	Fe_2O_3	RGO	0.5 M Na_2SO_4	1.8	[170]
		MnO_2	Fe_2O_3	Stainless steel	1 M Na_2SO_4 / CMC	2.0	[175]
		MnO_2	Fe_2O_3	Stainless steel	PVA / $LiClO_4$	2.0	[174]
		MWCNTs/ MnO_2	Fe_2O_3	Stainless steel	$K_3[Fe(CN)_6]$ in 1 M Na_2SO_4	2.0	[208]
		MnO_2/ CNT	Fe_2O_3/ CNT	PDMS	PVA / Na_2SO_4	2.0	[209]
		MnO_2/ FGS	Fe_2O_3/ FGS	Ti foil	1 M Na_2SO_4	2.0	[173]
		MnO_2	$NiCo_2S_4$@ Fe_2O_3	Carbon cloth	1 M Na_2SO_4	2.3	[180]
MnO_2// Fe_3O_4	1.4	MnO_2	Fe_3O_4	Stainless steel grid	0.1 M K_2SO_4	1.8	[182]
		PEDOT@ MnO_2	C@ Fe_3O_4	Stainless steel fiber	PVA / LiCl	2.0	[183]
MnO_2// MoO_3	2.5	MnO_2/ rGO	MoO_3/ rGO	stainless steel strip	PVA / H_3PO_4	1.6	[186]
		CF/ MnO_2	CF/ MoO_3	Carbon fiber	PVA / KOH	2.0	[188]
		CNT/ MnO_2	CNT/ MoO_3	Filter paper	1 M Na_2SO_4	2.0	[187]
		RGO/ MnO_2	RGO/ MoO_3	Nickel foil	1 M Na_2SO_4	2.0	[81]
MnO_2// V_2O_5	2.45	MnO_2/C	CNT/ V_2O_5	Nickel foam	1 M Na_2SO_4	1.6	[191]
		MnO_2-PPy-CF	V_2O_5-PANI-CF	Carbon fiber	4 M LiCl	2.0	[193]
MnO_2// Bi_2O_3	1.8	MnO_2	Bi_2O_3	Carbon nanofiber paper	1 M Na_2SO_4	1.8	[195]
MnO_2// Co_3O_4	1.7	MnO_2	S-Co_3O_4	Carbon cloth	PVA / LiCl	1.8	[197]
MnO_2// WO_3	2.25	MnO_2	WO_3	Stainless steel	PVA / $LiClO_4$	1.8	[198]
MnO_2// V_6O_{13}	2.45	MnO_2/ graphene	S-doped V_6O_{13-x}@C	Carbon cloth	5 M LiCl	1.8	[192]
Mn_3O_4// Fe_2O_3	1.4	RGO/ Mn_3O_4	RGO/ Fe_2O_3	RGO paper	3 M KOH	1.8	[178]
Mn_3O_4// VO_2	2.45	RGO@ Mn_3O_4	RGO@ VO_2	Carbon cloth	1 M Na_2SO_4	2.2	[199]
Na_xMnO_2// MoO_2	1.6	Na_xMnO_2	MoO_2	Carbon cloth	1 M Na_2SO_4	1.8	[200]
$NaMnO_2$// Fe_2O_3	1.4	$NaMnO_2$	α- Fe_2O_3	CNT fiber	Na_2SO_4 / CMC	2.2	[176]
$NaMnO_2$// MoO_2	2.0	$NaMnO_2$	MoO_2	Carbon fiber	1 M Na_2SO_4	2.5	[168]
$Na_{0.5}MnO_2$// Fe_3O_4	1.4	$Na_{0.5}MnO_2$	Fe_3O_4@C	Carbon cloth	1 M Na_2SO_4	2.6	[202]
SnO_2// V_2O_5	2.35	SnO_2/ MWCNT	V_2O_5/ MWCNT	Graphite sheet	0.5 M Li_2SO_4	1.8	[203]
SnO_2// MoO_3	2.4	RGO/ SnO_2	RGO/ MoO_3	Titanium mesh	2 M Li_2SO_4	1.8	[204]
ZrO_2//WO_3	3.35	MWCNT/ZrO_2	MWCNT/ WO_3	Graphite sheet	7.5 mmol KI in 1 M Li_2SO_4	2.2	[210]

overpotential window of the electrolyte, thus providing an extended potential window of 1.3 V from MnO_2 with a capacitance of 283.7F/g at a scan rate of 10 mV s^{-1}. The fabricated ASC using these electrodes provided a stable operating window of 2.3 V, delivering a specific capacitance of 60F/g with an energy density of 45 Wh kg^{-1} at a power density of 10.8 kW kg^{-1}. Also, good cycling stability of 90% retention was achieved after 6000 cycles.

Another phase of iron oxide, which is studied as a supercapacitor electrode, is magnetite (Fe_3O_4). Fe_3O_4 is an attractive anode material due to its large theoretical specific capacitance, natural abundance, low cost, and high potential window [181]. The work function difference of 1.4 eV between MnO_2 and Fe_3O_4 is encouraging for developing high-voltage ASCs using these electrodes [182]. Further developing high voltage fiber-shaped energy storage devices helps in knitting or weaving them into the wearer's clothes for powering sensors and electronics [4]. A fiber ASC developed with PEDOT@MnO_2 and C@Fe_3O_4 electrode delivered an output voltage of 2 V in PVA/LiCl electrolyte [183]. For fiber-shaped and flexible energy storage devices, the effective way of developing electrodes is to directly deposit or grow the electrode-active materials on the current collector substrates. This approach eliminates the non-conductive binders, which makes the overall electrode rigid and impedes flexibility. Electrodeposition is followed for making MnO_2 and Fe_3O_4 electrodes on stainless steel fibers, which resulted in nanosheet morphology providing a huge surface area for charge storage. The overall conductivity and charge storage abilities of the MnO_2 and Fe_3O_4 electrodes were enhanced by adding conductive

materials like PEDOT, carbon coating, etc. An ASC device fabricated with these fiber-based electrodes using the gel electrolyte delivered a maximum areal and volumetric capacitance of 73.2 mF cm^{-2} and 8.78F cm^{-3} at a scan rate of 20 mV s^{-1}. The fiber ASC still suffered from stability issues due to the mechanical expansion during cycling. It could retain only 80% of initial capacitance after 800 cycles. The fiber ASC exhibited a better charge storage ability under various mechanical deformation conditions, making it a promising energy source for wearable electronics.

Manganese oxide and molybdenum oxide (MnO_2 // MoO_3) as the positive and negative electrode material respectively is another highly explored asymmetric configuration system due to their wide work function difference of 2.5 eV [184–187]. Such a wide work function difference means this ASC system has the potential to deliver a very high output voltage along with higher energy density. Molybdenum oxide is a low-cost energy storage material offering high electrochemical activity. Although the work function difference between MnO_2 // MoO_3 system is very high, MoO_3, being a d^0 metal oxide, forms oxygen vacancies. This causes their work function value to drop considerably from 6.9 eV to 6.2 eV in ambient conditions, providing an approximate work function difference of 1.8 eV. This is one of the prime reasons for the MnO_2 // MoO_3 system to deliver an output voltage range of 1.6 to 2 V. This is a general characteristic in all the high work function d^0 MOs such as MoO_3, V_2O_5, etc. An asymmetric supercapacitor fabricated with MnO_2 and MoO_3 as positive and negative electrode materials, respectively, delivered a voltage window of 2 V in PVA/KOH gel electrolyte [188]. A simple electrodeposition process was followed to develop petal and spine-shaped nanostructures directly on carbon fibers. Though this device delivered a higher voltage of 2 V due to the microstructure dimensions of the electrodes, they lacked the surface area for storing charges. This caused them to deliver a poor capacitance of 4.86 mF cm^{-2} at a current density of 0.5 mA $cm^{-2,}$ which in turn led to a low energy density of 2.7 μWh cm^{-2} at a power density of 0.53 mW cm^{-2}.

One of the attractive approaches for tackling the poor conductivity in MOs is encapsulating or wrapping the carbonaceous materials around the MOs, which would provide a conductive network facilitating shorter diffusion paths for ions [189,190]. A self-assembly synthesis method followed to develop rGO-wrapped MnO_2 nanospheres and MoO_3 nanosheets resulted in a high-voltage ASC assembled with 1 M Na_2SO_4 electrolyte with a voltage window of 2 V [81]. The wrapping of the rGO around mesoporous MnO_2 nanospheres improves the overall electrical conductivity and provides a better capacitance of 350F/g at a current density of 200 mA g^{-1}. The self-assembly of the MoO_3 nanosheets on rGO layers offers a platform for enhanced electron transport with a capacitance of 291F/g at 2 mV s^{-1} scan rate. The overall advantage obtained from the individual electrodes was clubbed into ASCs, delivering a voltage of 2.0 V, which is even higher than the work function difference of 1.8 eV between the electrodes. The chemisorption of the H^+ and OH^- ions on the surface of the electrodes can be credited to the modified work function of electrodes, which helps in achieving the higher voltage.

Another combination of metal oxide // metal oxide ASC providing a high voltage is manganese oxide and vanadium oxide due to a wide work function difference of 2.45 eV [191,192]. Again, the formation of the oxygen vacancy defects reduces the work function of V_2O_5 and has an adverse effect on the final voltage obtained from the fabricated ASC. An electrochemical deposition method followed to deposit the active materials of MnO_2-PPy and V_2O_5-PANI on carbon fiber delivered an output voltage of 2 V in 4 M LiCl electrolyte [193]. The fiber-shaped ASC device exhibited a volumetric capacitance of 19.5F cm^{-3} and an energy density of 10.8 mWh cm^{-3}. The fiber ASC was also able to perform well under bending conditions with little capacitance drop. A stable cycle life (up to 5000 cycles) was achieved with no degradation. Bismuth oxide is a promising negative electrode material with high theoretical capacitance, low cost, and electrochemical stability. Moreover, it shows a high work function of 6.2 eV suitable for achieving high voltage ASC when combined with the low work function positive electrode material [194]. An ASC assembled with MnO_2 as the positive (4.4 eV) and Bi_2O_3 (6.2 eV) as the negative electrode material on carbon nanofiber (CNF) paper delivered a stable voltage window of 1.8 V in 1 M Na_2SO_4 electrolyte [195]. The obtained voltage window corresponds to the work function difference between the electrodes. The individual electrodes prepared via wet chemical methods had a porous nanoflower structure made of interconnected nanosheets. Such nanostructures are vital for enhancing the active surface area and shortening the ion diffusion path for charge storage. The assembled ASC delivered an areal capacitance of 97 mF cm^{-2} with an energy density of 43.4 μWh cm^{-2}. Using CNF paper as the substrate gives the advantage of flexibility and mechanical stability for developing a flexible energy storage device.

Cobalt oxide, with a work function value of 6.1 eV, is another promising negative electrode material for developing high-voltage ASCs. Though they are high theoretical capacitance materials, they still suffer from poor conductivity and low rate capability [196]. To overcome these drawbacks, in some instances, they have been developed as composites with other conductive materials or synthesized into nanostructures onto conductive scaffolds [197]. Sulphur (S) doping of Co_3O_4 nanowires via hydrothermal method has proven to be enhancing the electrochemical performance of cobalt oxide electrodes. Electrochemical studies showed that capacitance value increased significantly with S doping, reaching 0.55F cm^{-2} at a scan rate of 10 mV s^{-1}. Also, the IR drop was minimal (12 mV) for S-Co_3O_4 compared to 163 mV in Co_3O_4. The enhancement after S-doping can be attributed to the carrier concentration and conductivity of the electrodes. When an ASC was fabricated with S-Co_3O_4 and MnO_2 in PVA/LiCl electrolyte, it reached a stable voltage window of 1.8 V, slightly higher than the theoretical work function difference of 1.7 eV between the Co_3O_4 and MnO_2. The assembled ASC device had a maximum volumetric capacitance of 1.92F cm^{-3} at a current density of 1 mA cm^{-2} and an energy density of 0.86 mWh cm^{-3} at a power density of 0.79 W cm^{-3}. Tungsten oxide (6.65 eV) and manganese oxide (4.4 eV), when combined to form an ASC, have a work function difference of 2.25 eV. Lokhande et al. developed a flexible solid-state ASC using the thin films of these materials deposited on stainless steel substrates [198]. The assembled ASC in PVA-$LiClO_4$ gel electrolyte reached an operable voltage window of 1.8 V. One of the possible reasons the voltage window is low even with a higher theoretical work function (WF) difference is the use of metal substrate as current collectors. As we have seen, the presence of metal as the current collector induces the overpotential at an early potential. Also, the presence of d^0 metal oxide brings down the overall work function difference due to the formation of oxygen vacancy defects. The assembled ASC delivered a capacitance of 115F/g with an energy density of 52 Wh kg^{-1}.

Suppressing the OER and HER activity at the cathode and anode is an effective approach to enhancing the output voltage of aqueous

ASCs [199]. In-situ activation of the electrodes induces the formation of specific oxidation states. Conversion of RGO/Mn_3O_4 to RGO/α-MnO_2 forms Mn^{7+} oxidation state, which is essential for the enhanced overpotential or increased OER potential of the cathode. The surface-activated cathode material with mixed Mn_3O_4 and α-MnO_2 state was able to deliver a −0.1 to 1.2 V potential window in 1 M Na_2SO_4 electrolyte. The RGO/VO_2 composite developed had majorly V^{3+}, V^{4+} oxidation states and the reduction of V^{3+} to V^{2+} occurring near the HER potential allowed the electrode to operate at a higher negative potential window from 0 to −1 V in 1 M Na_2SO_4 electrolyte. Thus, the driven route providing overpotential for suppressing OER and HER potential gives an insightful study on enhancing the available voltage window. Here, an ASC device fabricated was able to reach 2.2 V with no evolution in 1 M Na_2SO_4 electrolyte, delivering a maximum energy density of 42.7 Wh Kg^{-1} and power density of 11260 W Kg^{-1}.

The positive electrode material can also be modified to reduce its work function. For example, pre-inserting sodium ions in MnO_2 helps in decreasing the mean oxidation state of Mn, which in turn lowers the work function of the electrode**.** This is an effective approach towards enhancing the work function difference between the electrodes for developing high-voltage supercapacitors. Recently, research showed improvement in the potential window of MnO_2 via cation doping [168,200]. An approach to studying the work function change in MnO_2 electrode via various cation insertions (Li^+, Na^+ and K^+) has successfully demonstrated that the work function of MnO_2 can be effectively reduced by Na^+ doping to develop a high voltage aqueous asymmetric supercapacitor [168]. When a cation is pre-inserted into MnO_2, a decrease in the mean oxidation state of Mn may result in a reduced work function of the material. However, depending on the cation size and MnO_2 crystal structure, a different trend was observed in the work function change. The work function of all the materials developed was found via KPFM analysis [201]. It was found that the $NaMnO_2$ showed the lowest work function amongst all the compounds ($LiMnO_2$ and $KMnO_2$) formed. This is due to the Na^+ ion size, which can localize perfectly in the center of the 2 × 2 tunnel of MnO_2 compound. An asymmetric supercapacitor developed with this work function engineered $NaMnO_2$ and MoO_2 has exhibited a high voltage of 2.5 V in 1 M Na_2SO_4 electrolyte. Further, the asymmetric device has shown a maximum energy density of 78 Wh kg^{-1} at a power density of 4.6 kW kg^{-1} with capacitance retention of 98.6% after 5000 cycles. Recently, in another pre-insertion study involving $NaMnO_2$ electrodes, a very high voltage aqueous ASC of 2.6 V delivering an energy density of 81 Wh Kg^{-1} was reported by Xia et al., as shown in Fig. 16. This high voltage was achieved by choosing $Na_{0.5}MnO_2$ and Fe_3O_4 as the electrodes [202]. A low work function difference between MnO_2 and Fe_3O_4 electrodes was tackled by pre-inserting sodium ions into the MnO_2 crystals. The insertion of Na^+ ions into the MnO_2 crystal will decrease the mean oxidation state of Mn, thus decreasing the actual work function of MnO_2. Hence, the work function difference between $Na_{0.5}MnO_2$ and Fe_3O_4@C will go beyond the theoretical value of 1.4 eV. This is the prime reason behind the higher voltage window from this asymmetric supercapacitor compared to the actual work function difference values. In addition, the amount of pre-inserted cations in MnO_2 has an influence on the formation of Mn^{3+}/Mn^{4+} redox couple and therefore high Na/Mn ratio will provide higher pseudocapacitance. The $Na_{0.5}MnO_2$ synthesized has a porous nanowall array structure providing a high surface area for charge storage with an individual electrode's potential range of 0 to 1.3 V and high specific capacitance of 366F/g. Here, the negative electrode made of Fe_3O_4 nanorod arrays was coated with a very thin layer of carbon to prevent the dissolution of the electrode. Thus, a negative electrode provided a potential range

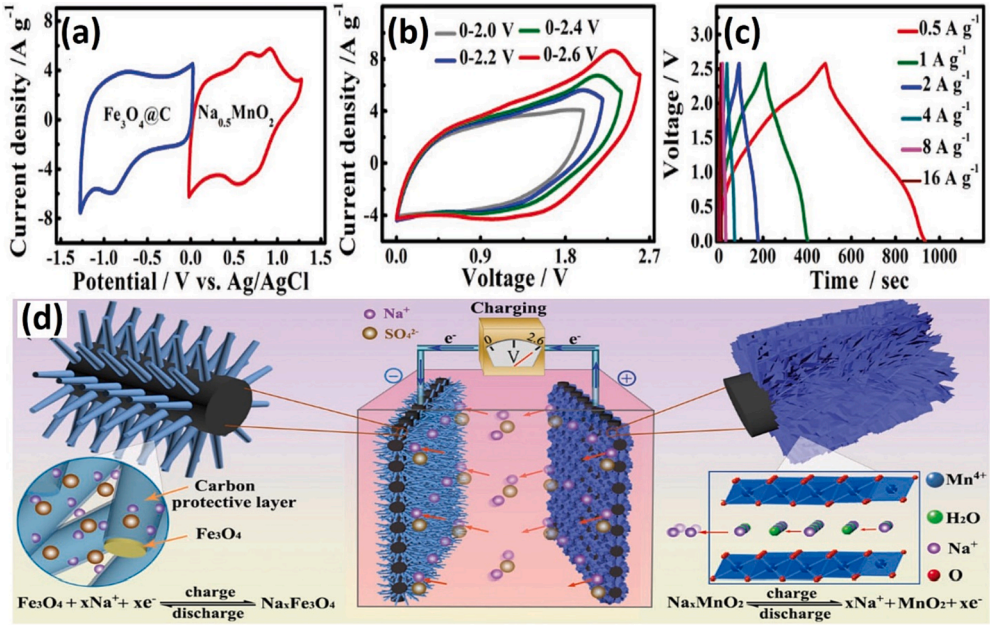

Fig. 16. (a) CV curves of the $Na_{0.5}MnO_2$ and Fe_3O_4@C electrodes in separate potential windows at a scan rate of 10 mV s^{-1}. b) CV curves of the $Na_{0.5}MnO_2$//Fe_3O_4@C ASC in different voltage windows at a scan rate of 50 mV s^{-1}. c) GCD curves of the $Na_{0.5}MnO_2$//Fe_3O_4@C ASC at different current densities. (d) Electrode designs and charge-storage mechanism of the $Na_{0.5}MnO_2$ cathode and the Fe_3O_4@C anode in the ASC system. Reproduced with permission from reference [202] copyright 2017 Wiley.

of −1.3 to 0 V with a high specific capacitance of 344F/g. With a large work function difference and a high potential range of individual electrodes, a high operating voltage of 2.6 V was achieved from a single ASC device. Also, one of the main reasons to accomplish this feat was using carbon cloth as a substrate, which is crucial in increasing the water decomposition potential (1.3 V) compared to metal substrates, which induces them even at a lower potential of 0.8 V for individual electrodes.

Apart from MnO_2, SnO_2 is another low work function metal oxide cathode suitable for developing high-voltage ASC. They can be combined with high work function MOs to develop supercapacitors, which can provide a potential higher than 2 V. In a recent work involving a combination of SnO_2 (4.5 eV) as positive and V_2O_5 (6.85 eV) as the negative electrode material, a work function difference of 2.35 eV was attained [203]. Here, an aqueous neutral electrolyte (0.5 mol/L Li_2SO_4) with high hydration energy was used. With the work function difference of 2.35 eV and the high hydration energy of the electrolyte, an operational voltage window of >2.3 V was expected. However, the ASC was able to deliver only 1.8 V. This limitation was caused due to the usage of d^0 oxide, V_2O_5, which has the tendency to form oxygen vacancies. The presence of oxygen vacancies leads to the formation of other phases, such as VO_2, which changes the d^0 state to the d^1 state, eventually reducing the work function. The final device delivered a specific capacitance of 198F/g at a current density of 1 A g^{-1} with an energy density of 89 Wh Kg^{-1}. Another interesting ASC electrode with SnO_2 is a combination with high work function metal oxide, MoO_3, for achieving a wide work function difference of 2.4 eV [204]. As mentioned before, being a d^0 oxide, MoO_3 tends to form oxygen vacancy defects, causing their work function to reduce. Hence, the ASC system fabricated was able to deliver only 1.8 V in a neutral aqueous electrolyte of 2 M Li_2SO_4. The assembled ASC achieved a specific capacitance of 73.9F/g with a maximum energy density of 33 Wh kg^{-1}. Moreover, it had an excellent cycle life of 20,000 cycles with only 7.5% capacitance loss. This excellent cyclic stability can be attributed to the good electrical contact between MOs and RGO and the low crystallinity nature of the electrodes preventing the volume change during cycling.

7. Voltage window in double-layer capacitors

As discussed previously, EDLCs represent a unique class of supercapacitors where the capacitance arises from a double layer formation of dielectric solvent and a solvated electrolyte ion on electrically conductive, high surface area porous materials such as porous carbons [211]. Theoretically, EDLCs exhibit very low degradation of material during charge–discharge cycles and offer high columbic efficiencies. However, in regards to their application, they are limited by their energy density due to their low operational voltage window [50]. Fortunately, in recent years, the charge storage ability of these double-layer capacitors has been significantly enhanced due to effectively increasing the specific surface area, optimization of pore sizes and their distribution throughout the active material. This has been achieved by synthesizing hierarchal porous structures without compromising electrical conductivity [212,213]. On the other hand, electrolytes' composition has also been studied to enhance the density of adsorbed ions on the electrode's surface [214,215]. As discussed previously, voltage has a quadratic effect on the energy density of supercapacitors (eq. (1). Hence, voltage window is a critical factor for EDLCs to be able to cater to the growing energy needs of the market.

Active material-based voltage windows in EDLCs can be broadly studied based on: 1) the effect of surface functional groups on the voltage window, 2) the effect of the electrode–electrolyte interface on voltage window, and 3) hybrid design in double-layer capacitors.

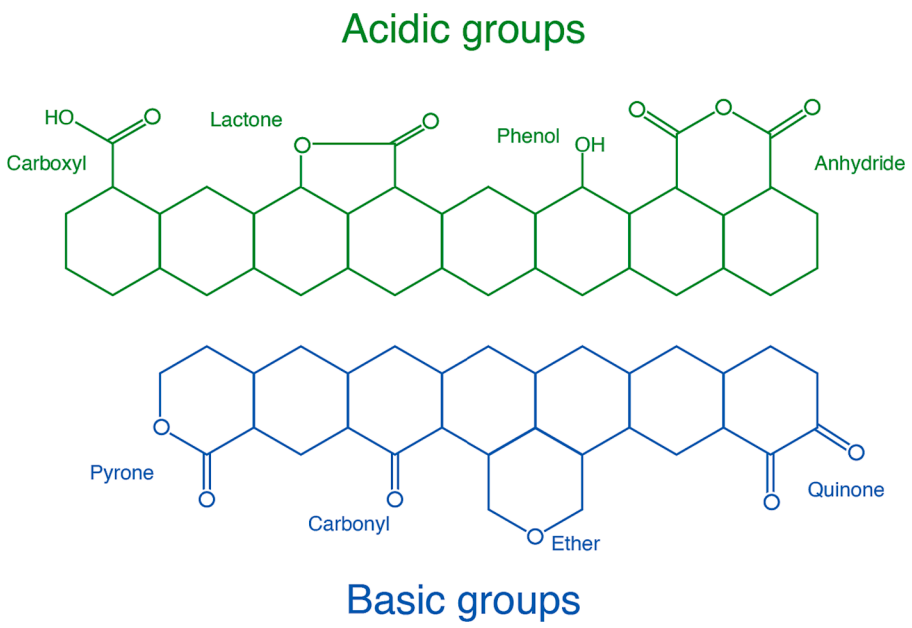

Fig. 17. The figure shows various types of oxygen-containing functional groups present on the nanostructured surface of activated carbon. Based on the type of bond between oxygen, carbon, and hydrogen, these functional groups can be either acidic or basic in nature.

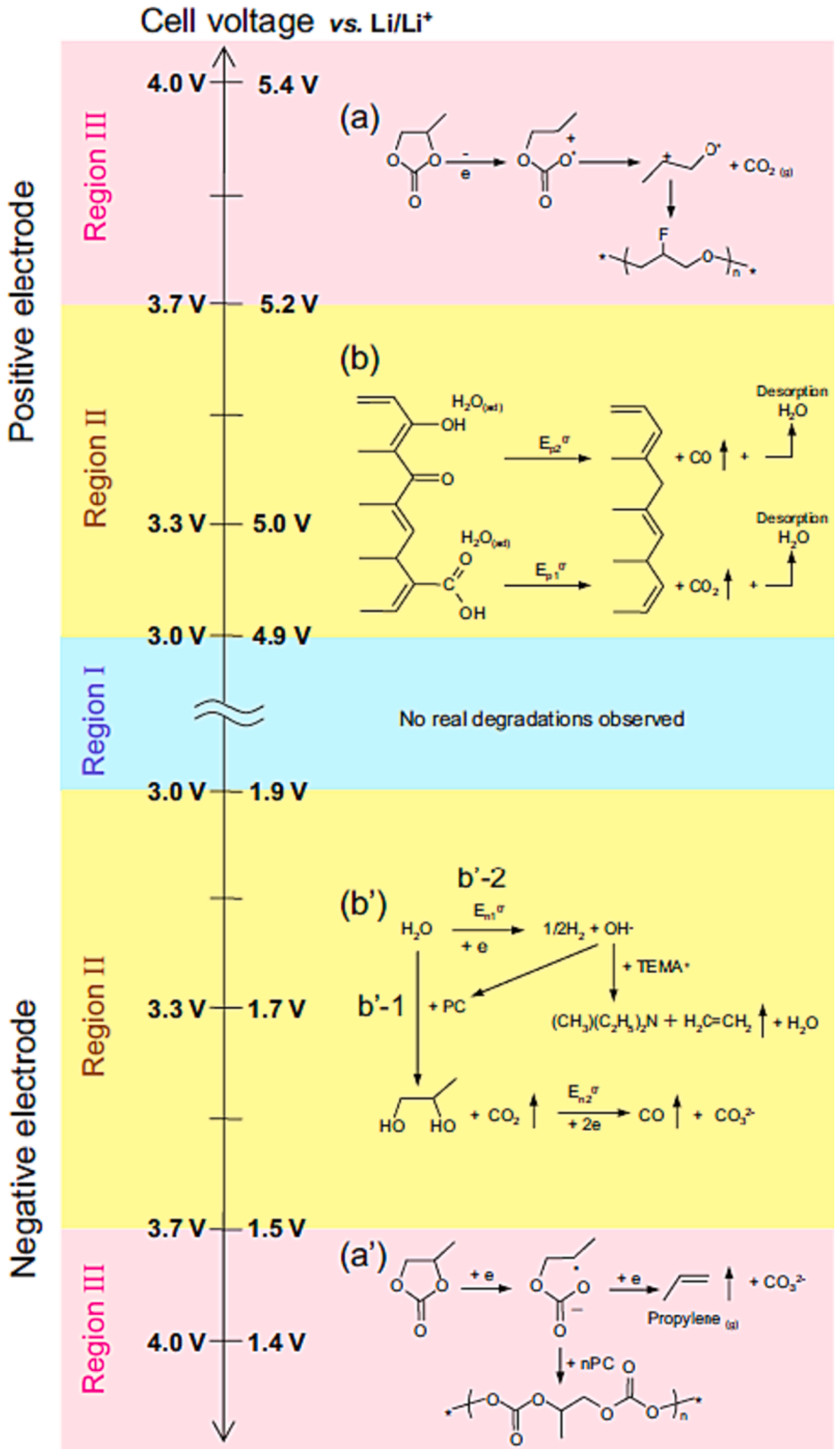

Fig. 18. Probable side reaction mechanisms based on their occurrence voltage on a positive electrode. Region II (b) shows surface functional groups like carboxyl, phenol and ketone getting attacked by water molecules at their respective oxidation potentials. Reproduced with permission [218].

7.1. Effect of surface functional groups on voltage window

Many advanced nanostructured carbon materials like graphene, activated carbons & carbon nanotubes have been widely studied for their double-layer capacitance. These carbon-based materials possess surface functional groups that can significantly govern the voltage window as they directly influence the electron donor/acceptor levels of the electrolyte or the carbon material itself. Based on the formation history of carbon material and its carbonization and activation temperature, two types of surface oxygen-containing functional groups (SOGs) can be developed on these activated carbons: [216] acidic or basic (as shown in Fig. 17 below). The acidic functional groups are formed when carbon is heated in the presence of oxygen between a temperature range of 200 to 700 °C or by reaction with oxidizing agents at room temperature. These acidic functional groups are generally less stable and are comprised of carboxyl, lactone, phenol, and anhydride groups. However, the basic groups have less oxygen content, making the edge reactive outwards nanostructures less polar. Moreover, these basic SOGs also make the surface hydrophilic in nature, with positive charge sites perfect for anion adsorption [217]. This increases the wettability of electrolytes and facilitates redox reactions, enabling redox capacitance.

The voltage window generally ranges between 2.5 and 2.7 V when activated carbon electrodes and organic electrolytes are used. Beyond 2.7 V, the capacitance starts to decrease following an increase in the internal resistance, which leads to rapid aging of the assembled supercapacitor. The most critical factors that cause this rapid degradation of supercapacitor above a certain voltage are the undesired faradaic reactions at the electrode surface marked by gas evolution and surface film formation [218]. There have been a few reports regarding this quick aging mechanism in activated carbons with organic electrolytes when operated above their ideal voltage range. A cell voltage study done by Ishimoto et al. found that CO_2 and CO are evolved beyond a voltage range of 3.0 to 3.5 V due to the oxidation of propylene carbonate (PC) and surface functional group on the carbon as the positive electrode [218]. The probable reaction mechanisms are shown in Fig. 18. As shown in region II (b), the oxidative phenolic group tends to support higher potentials up to 3.6 V, whereas carboxyl groups start oxidizing at 3.0 V, making the voltage range smaller.

In a recent work performed on EDLCs, Morimoto et al. [219] and Yoshida et al. [220] have suggested that the oxygen-containing surface functional groups adversely affect the electrodes' stability and tend to increase the leakage current. Their studies have concluded that these oxygen-containing surface functional groups tend to increase the oxidation or reduction rate of electrodes or the electrolyte, leading to high leakage current and quicker decomposition of electrode material. In order to extend the voltage window of EDLCs, these oxygen-containing surface functional groups must be removed. Yong et al. [221,222] used -temperature treatment (HTT) to remove these functional groups, which improved stability at higher voltages. They used commercially available MSP20 activated carbon which was heat-treated at 900 °C under argon atmosphere. This process also improved the electronic conductivity by reducing the impedance and showed 95% capacitance retention during the GCD cycling test performed at a voltage range from 1.0 V to 2.7 V. Results also showed that this surface modification helped to further enlarge the voltage window from 2.7 V to 3.1 V with high cycling stability.

Thus, in order to achieve a larger voltage window in EDLCs, surface treatment of the electrodes is a good option. The surface treatment can be either a physical method or a chemical method. High-temperature treatment is an example of a physical method of surface treatment. Though it is very effective and straightforward to perform, it could cause some complications, like disruption in the pore structure or dimensions of the pores in the carbon substrate. Moreover, high-temperature treatments usually involve treatment under the flow of hydrogen or some inert gas [221], during which the removal of these surface functional groups would never be complete. Hence, some chemical modification methods have also been suggested to solve this issue. Some organosilicon compounds can be coated on the activated carbons via a liquid chemical reaction or by using gas-phase fluorination (plasma) with the help of fluorocarbons (like C_2F_4 or C_2F_6), making the surface hydrophobic [223]. Thus, saving the electrode surface from trace water molecules helps to achieve higher overpotential on the electrodes, extending the voltage range of the supercapacitor. In another chemical mode of achieving hydrophobicity, Fang and Binder [224] used vinyltrimethoxysilane (vtmos) functional group to replace oxygen functionalities on the Norit (SX plus) activated carbon electrode. Vtmos acts as a surfactant and to place on the activated carbon, the electrode surface was soaked into the 0.25 wt% of the aqueous surfactant solution. The water-attracting hydroxyl groups are replaced by alkoxysilane molecules in a silylation reaction. Depending on the surface density of the hydroxyl groups, one, two, or three of them together may form the bridging structure to bind vtmos on the surface of activated carbon [225–227]. This grafting mechanism of vtmos not only induces the hydrophobicity on the surface of carbon but also increases the affinity of the organic molecule of electrolyte PC towards the carbon electrode. This was also confirmed by a 68% increase in specific capacitance and a 196% increase in energy density at a higher discharge rate of 100 mA/cm^2. The use of vtmos to improve the hydrophobicity of carbon electrodes has also been investigated in a few other studies like Budarin [228] and Cosnier [225]. Though their studies were not linked to supercapacitor performance, their work revealed that too much vtmos leads to a dramatic decrease in the pore volume of the carbon electrodes, thus making them unsuitable for applications in EDLCs. However, using vtmos to improve the hydrophobicity of activated carbon electrodes results in an extended voltage window of organic electrolytes, thereby improving the overall voltage range of the device.

As seen in the preceding discussions, the surface chemistry of activated carbon is an important parameter determining the overall capacitance, voltage range, and aging rate (cycle life). These oxygen-containing surface functional groups could significantly lower the voltage limit of the electrodes by having hydrophilic characteristics. In order to suppress the effect of these functional groups and enhance the performance of the electrodes, these carbon-based electrodes can also be doped with hetero atoms like nitrogen, phosphorous and sulfur. This could enhance the capacitance by improving charge mobility, better wettability of electrolyte [229,230], and electronic conductance [231]. However, putting these dopants on the surface of carbon electrodes shows almost no improvement in the cycle life. This could be associated with the existing oxygen-containing surface functional groups, which are prone to moisture adsorption, resulting in gas evolution from the decomposition of the electrolyte [232]. In a study conducted by Chi. et al. [233] based

on nitrogen doped-vertically grown graphene nanowalls (NGNW), showed that nitrogen doping led to an increase in the number of defects on the graphene lattice. This significantly raised the oxygen content on these nanowalls, which resulted in irreversible oxidation of the organic electrolyte at more positive potentials. Interestingly, when this NGNW was used as a negative electrode material, the irreversible redox reactions of electrolytes were suppressed, which helped in the extension of the voltage window of the device. These N-based surface functional groups have been used many times to significantly enhance the electrochemical performance of the EDLCs by various routes. Shiraishi et al. [234] used nitric oxide and performed a heat treatment of the activated carbon electrode at a temp of about 800 °C under an inert atmosphere of helium. They performed the high voltage cycling stability study on three samples: pristine activated carbon (AC), heat-treated activated carbon (Heated AC), and nitric oxide – heat-treated activated carbon (NO-AC). Both heated AC and NO-AC showed improvement in capacitance retention during high-voltage cycling studies of up to 3 V. However, the heated AC (but not treated with NO) sample showed only slight improvement. This could be owed to the partial removal of the oxygen functional group during the heat treatment. The NO-AC electrode significantly improved capacitance retention during the high-voltage cycling. This was also confirmed by the XPS analysis. It showed no change in content and the chemical state of nitrogen on the activated carbon electrode. In another study performed by salina-Torres et al. [235], which involved carbonization of polyaniline (PANI) electrodes, it was found that due to this surface treatment of electrodes, N containing surface functional groups were able to prevent the nucleophilic attack on the electrolyte. This helped to extend the voltage range of electrolyte. Also due to the presence of these aromatic N species on the surface, the electrochemical decomposition of carbon electrode is prevented, which was reflected in the reduced leakage current. Similarly, in some of the other works, besides improving high voltage cycling stability, nitrogen doping has also helped to improve electron transfer rate [236,237], wettability of electrolyte [238,239], lowering of the ESR [238] and enhancing the capacitance via pseudocapacitance [240].

Similar to nitrogen-based functional groups, some halides and sulfur groups can also be doped onto the surface of EDLC electrodes, improving cyclability and capacitive performance at a higher voltage range. Doping the surface of activated carbon-based electrodes with chlorine/fluorine-based groups could help bring down the surface polarity caused by the oxygen involving surface functional groups. Pinkert et al. [241] used ordered mesoporous carbide-derived carbon (OM-CDC) electrodes and performed surface functionalization via air oxidation and chlorine treatment in two separate experiments. This helped to perform a comparative study between the electrochemical behaviors of the oxygen functional group and the chlorine functional group. Ionic liquid (IL; 1-ethyl-3-methylimidiazolium tetrafluoroborate), also known as $EMIBF_4$ was used as an electrolyte. It was found that surface chlorination helps to remove the oxygen functional group and guards against further reoxidation. It also mitigates the surface polarity caused by the oxygen functional group and reduces the number of acidic protons that are attracted to adsorbed water vapor molecules, as shown by XPS. Overall, the rate capability was increased by 27% compared to pristine porous electrodes, even at the scan rates equal or greater than $10 mVs^{-1}$. This is shown in Fig. 19 (a). On the other hand, the OM-CDC-oxygen treated sample showed a 50% reduction in specific capacitance at scan rates greater than or equal to $10\ mVs^{-1}$.

**Similarly, using a fluorine-based surface functionalization technique, Kim et al. [242] were able to enhance the electronic conductivity of the activated carbon electrode within a voltage range of 0 to 2.7 V (Fig. 19(b)). Commercially available activated carbon MSP20 (R-AC) was treated with hydrofluoric acid, which resulted in the evolution of C-F bonds over the pre-existing surface functionalities like C—O, C═O, and O—C═O bonds on the activated carbon. This resulted in countering the detrimental effects of oxygen functionalities and obtaining the R-AC electrode's capacitive performance in a non-aqueous electrolyte in the voltage range of 2.7 V.

7.2. *Effect of an electrode–electrolyte interface on the voltage window*

As discussed previously, electrode surface properties could alter the stability of the electrode and the electrolyte in high-voltage

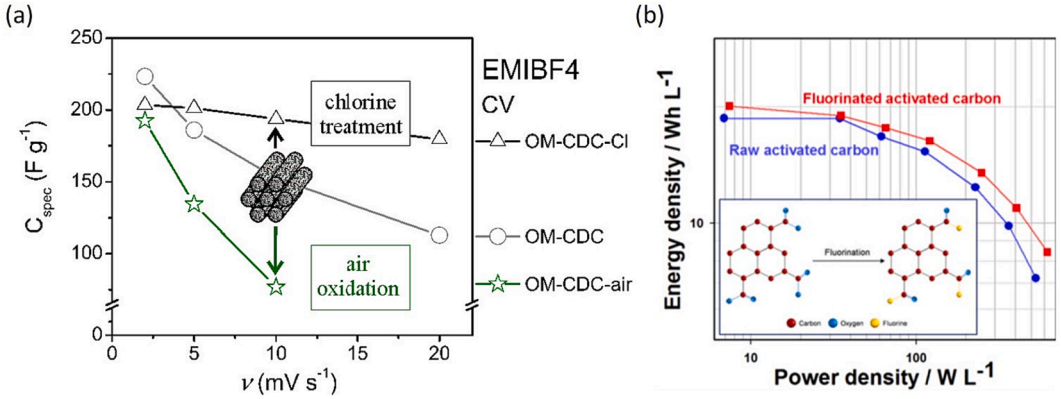

Fig. 19. (a) The increase in specific capacitance due to surface functionalization of OM-CDC electrode via chlorine doping compared with air oxidized OM-CDC electrode. Reproduced with permission [241] copyright 2014. (b) Improvement in energy and power density due to fluorine doping on the surface of activated carbon. Reproduced with permission [242] copyright 2014.

applications. Also, considerable changes can happen at the electrode–electrolyte interface that could affect the overall voltage window of the device. When used with (untreated) activated carbon electrodes, PC-based electrolytes generally start to decompose beyond 3.0 V [218]. Many decomposition products like CO, CO_2, H_2 start to bubble out from the electrolyte solution. With the help of scanning electron microscopy and X-ray photoelectron spectroscopy, it has been found that a thin film is formed at the electrode–electrolyte interface. This is due to a byproduct formed as a result of the electrolyte/electrode decomposition, which led to capacitance fading [243,244]. We can observe in the studies performed by Ruch et al. [243] that the degradation product of PC and acetonitrile (ACN) resulted in a thin layer on the electrode surface when the symmetric configuration was tested at a constant, elevated voltage of 3.5 V. This was also confirmed by nitrogen adsorption isotherms which showed that the exposed surface area of the positive electrode being

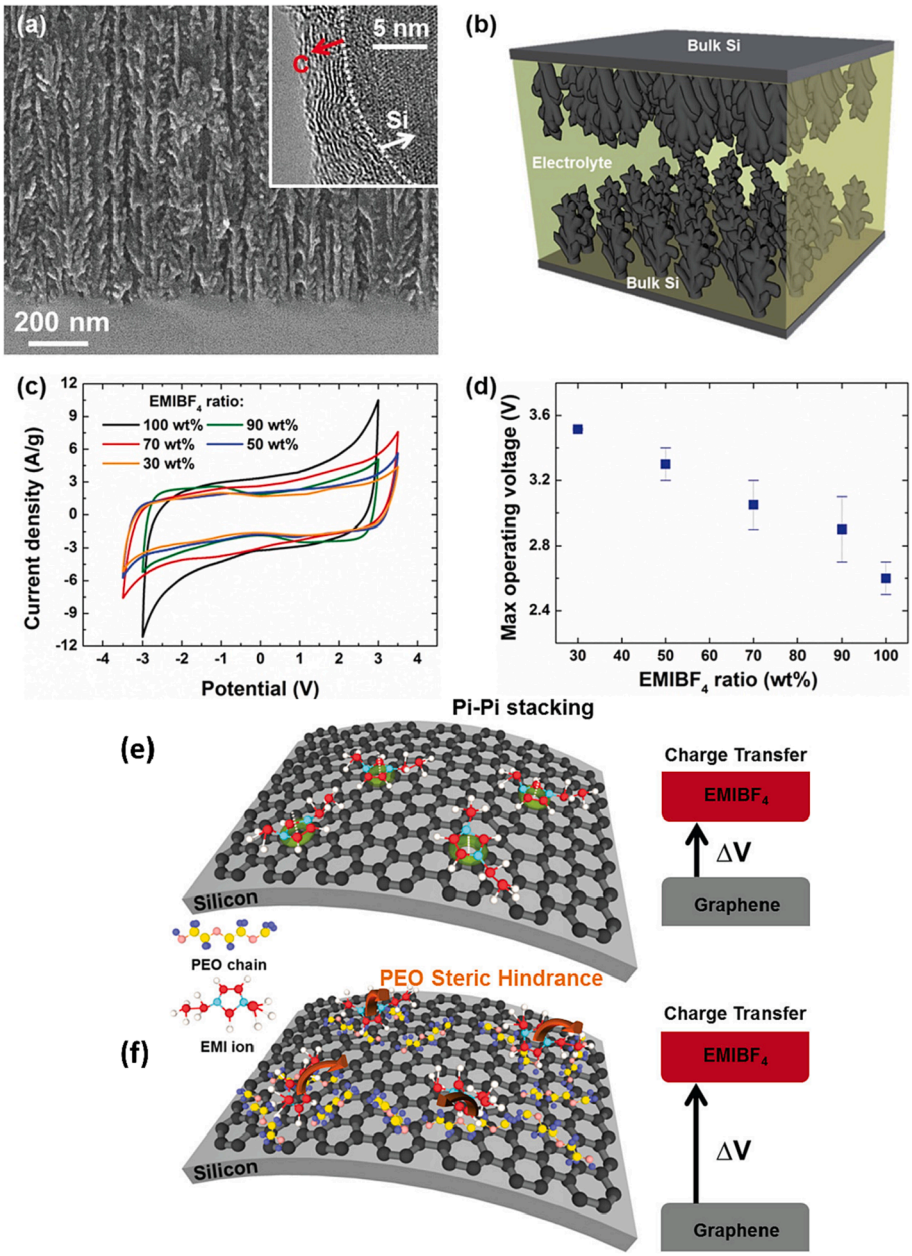

Fig. 20. (a) SEM with inset TEM image of the porous silicon material with the carbon layer interfaced with the electrolyte; (b) schematic illustration of the supercapacitor device; (c) CV comparison and (d) corresponding electrochemical voltage window of devices with different ratios of $EMIBF_4$ and PEO in the electrolyte. (e) Schematic illustration of pi-stacking between EMI + ions and a silicon-supported carbon surface; (f) illustration of the role that PEO polymer plays in disrupting the pi-stacked configuration of electrolyte at the carbon–electrolyte interface through steric hindrance. In both cases, energy diagrams on the right represent the observation that pi-stacked configurations lead to lower operating voltage windows (ΔV) than in cases where the PEO sterically inhibits pi-stacking. Reproduced with permission [255] copyright 2016.

reduced from 1503 m^2/g to 1007 m^2/g in PC electrolyte and dropping down to 319 m^2/g in ACN. This deposition not only impacted the exposed surface area but also led to a significant blockage of the available porosities, which were brought down from 0.5 cm^3g^{-1} to 0.34 cm^3g^{-1} in PC electrolyte and 0.13 cm^3g^{-1} in ACN electrolyte. The film formation was owed to the probable reduction reaction of trace water on the negative electrode, generating H_2 gas and OH^- ions. The H_2 gas would bubble and exit the system. At the same time, OH^- ions initiate the Hoffman elimination reaction and the hydrolysis of propylene carbonate, forming thick fluorinated films on both electrodes. However, this film formation is not necessarily bad for all electrodes; e.g., in the case of lithium-ion batteries (LIBs), the formation of solid electrolyte interface (SEI) film is very important for stable voltage performance.

In one of the works performed by Shen et al. [245], the electrolyte decomposition led to the formation of irreversible redox byproducts, which helped to enlarge the voltage window of the overall device. This work used activated carbon as the electrode material with 1 M tetraethylammonium tetrafluoroborate/PC ($TEABF_4$/PC) as an electrolyte. When activated carbon was treated with a positive potential of more than 0.1 V (vs. $Ag/AgNO_3$) in the 1 M $TEABF_4$/PC electrolyte, the decomposing electrolyte led to byproducts that passivized some hyperactive (reactive with trace water) areas of the electrode surface. Morphological characterization showed a rough, thick film covering the electrode surface composed of C, O, N, B, and F, as confirmed by the XPS spectra. Although they could not confirm the exact composition of the passivation layer, they argue that the layer should be composed of both types of solvent molecules and both ions of supporting electrolyte (i.e., the TEA^+ and BF_4^-). The high voltage cycle test was performed for about 400–500 cycles between a voltage range of −1.9 V to 0.5 V, which allowed the passivation layer to achieve a certain thickness that eventually led to the enlargement of the voltage window by 0.5 V. Going beyond, the researchers used this passivated AC electrode (+ve) and a pristine AC electrode (-ve) to fabricate an asymmetric supercapacitor, which helped to further enlarge the voltage window. This shows that some oxidized films of the electrolyte can prevent further damage to the electrode/electrolyte and facilitate the extension of the voltage window.

Similar to the additives of LIBs, which facilitate the formation of SEI, some additives can also work well for lithium-ion capacitors (LICs) [246]. These additives, like fluoroethylene carbonate (FEC) and vinylene carbonate (VC), could help in the formation of SEI, thereby suppressing the decomposition reaction of electrolytes in high-voltage applications. Using the FEC could help prevent the formation of inorganic compounds like Li_2CO_3, $Li_2C_2O_4$, and HCO_2 Li, which are non-conducting. In a study performed by Xu et al. [247], FEC has shown that it could suppress the degradation of $LiPF_6$ electrolytes. Based on the suggested decomposition mechanism of $LiPF_6$ [248], the presence of higher fluorinated phosphoric oxide as the initial decomposition product quickly interacts with the salt. It forms a stable SEI layer, which prevents further degradation of $LiPF_6$ even at higher voltages. In a recent study performed by Boltersdorf et al. [249], it was found that VC and tris-trimethylsilyl phosphate (TMSP), when used as additives, tend to increase cycle life and the rate capabilities of LICs. These additives serve a special purpose of hindering the redox reaction of the electrolyte at the electrode surface. They do so by quickly forming a stable SEI on the electrode electrolyte interface to protect the bulk electrolyte during the high voltage operations. TMSP has a lower reduction potential, thus saving the electrolyte by sacrificially reducing itself to form a low impedance SEI on the interface, giving high efficiency [250–254].

In another work, Li et al. [255] experimentally demonstrated that π- π bond stacking at a carbon electrode with an ionic liquid electrolyte interface can alter the device's voltage window by using steric hindrances introduced by polyethylene oxide (PEO) electrolyte additive. Refer to Fig. 20. They fabricated an all-solid-state supercapacitor device using porous silicon templated 3-D interconnected graphene electrodes in a symmetric configuration using $EMIBF_4$ ionic liquid electrolyte. Under the normal π- π bond stacking at a carbon interface, the device operated at a voltage of 2.6 V. However, when PEO was introduced as an additive in the electrolyte, the steric hindrances caused by the PEO molecules led to a 30% increase in the operational voltage, ramping it up to 3.5 V. The observation was supported by Raman spectroscopy, electrochemical impedance spectroscopy and differential scanning calorimetry, which elucidate the signature of the pi-pi stacking between imidazole species in the ionic liquid and the carbon surface -which is the effect usually shown at the carbon ionic liquid interface. This effect leads to a stronger chemical interaction between the carbon and the electrolyte, causing a lower energy barrier at the charge transfer reactions, resulting in lower operating voltage. This pi-pi stacking also lowers the specific capacitance due to an increase in the average distance of the stern layer from the carbon surface. The PEO chains disrupt this pi-pi stacking and increase the energy barrier for the charge transfer reactions, leading to increased potential and charge storage without the parasitic faradaic reactions occurring. Fig. 20 (a) shows porous silicon material's SEM and TEM (Inset) with carbon interface -electrode material. The schematics of the electrode architecture are shown in Fig. 20 (b). Corresponding CVs and electrochemical voltage windows of different devices with various ratios of $EMIBF_4$ and PEO electrolyte are shown in Fig. 20 (c) and (d), respectively. Fig. 20 (e) shows schematic illustrations of pi stacking between silicon-supported carbon surfaces. Fig. 20 (f) shows the PEO polymer layer disrupting the pi-stacked configuration and receiving the extended voltage range.

Apart from functionalizing the electrode–electrolyte interface, the ionic distribution at the electrode–electrolyte interface also tends to affect the voltage window and energy density in the carbon-based supercapacitors [256]. Researchers are also looking into studying the kinetics and distribution behavior of the electrolyte ions beyond the conventional electrode material improvements to enhance the performance of supercapacitors. Theoretically, three electrolyte ion distribution models have been popular in the field of electrochemical capacitors namely Helmholtz model, Gouy-Chapman (GC) model, and Gouy-Chapman-Stern (GCS) model [257,258]. Among these, the Helmholtz model proposed the concept of a double-layer formation of the solvated electrolyte for the first time. Later, Gouy and Chapman revised the Helmholtz model and suggested that the electrolyte distribution at the electrode interface is in a much thicker region than predicted by the Helmholtz model. In 1924, Stern combined the Helmholtz and the Gouy-Chapman models and suggested that there are two specific types of distribution of ion regions at the interface. The inner monolayer is called the stern, where all the polarized electrolyte solvent molecules are electrostatically stick at the electrode surface. Beyond this stern layer is a wider diffusion layer where both electrostatic and kinetic action occur. This GCS model is the widely accepted model to describe the interfacial ion distribution at the electrode electrolyte interface.

Exploring the utilization of this ionic distribution, Chen et al. [259] studied the ionic distribution using the classical density functional theorem (CDFT) and attempted to tune the ionic concentration at the electrode–electrolyte interface. They constructed a symmetric supercapacitor model with porous carbon as the electrode and potassium hydroxide solution as the electrolyte. They found that with the increase in the electrolyte concentration, the anions and cations arrange themselves in a better oscillatory multilayer distribution, which in turn helps to increase the overall capacitance of the system. In fact, this increase in capacitance is again due to an interplay of a type of potential change in the diffusion layer of the interface. In the CGS model, the theoretical capacitance of the double

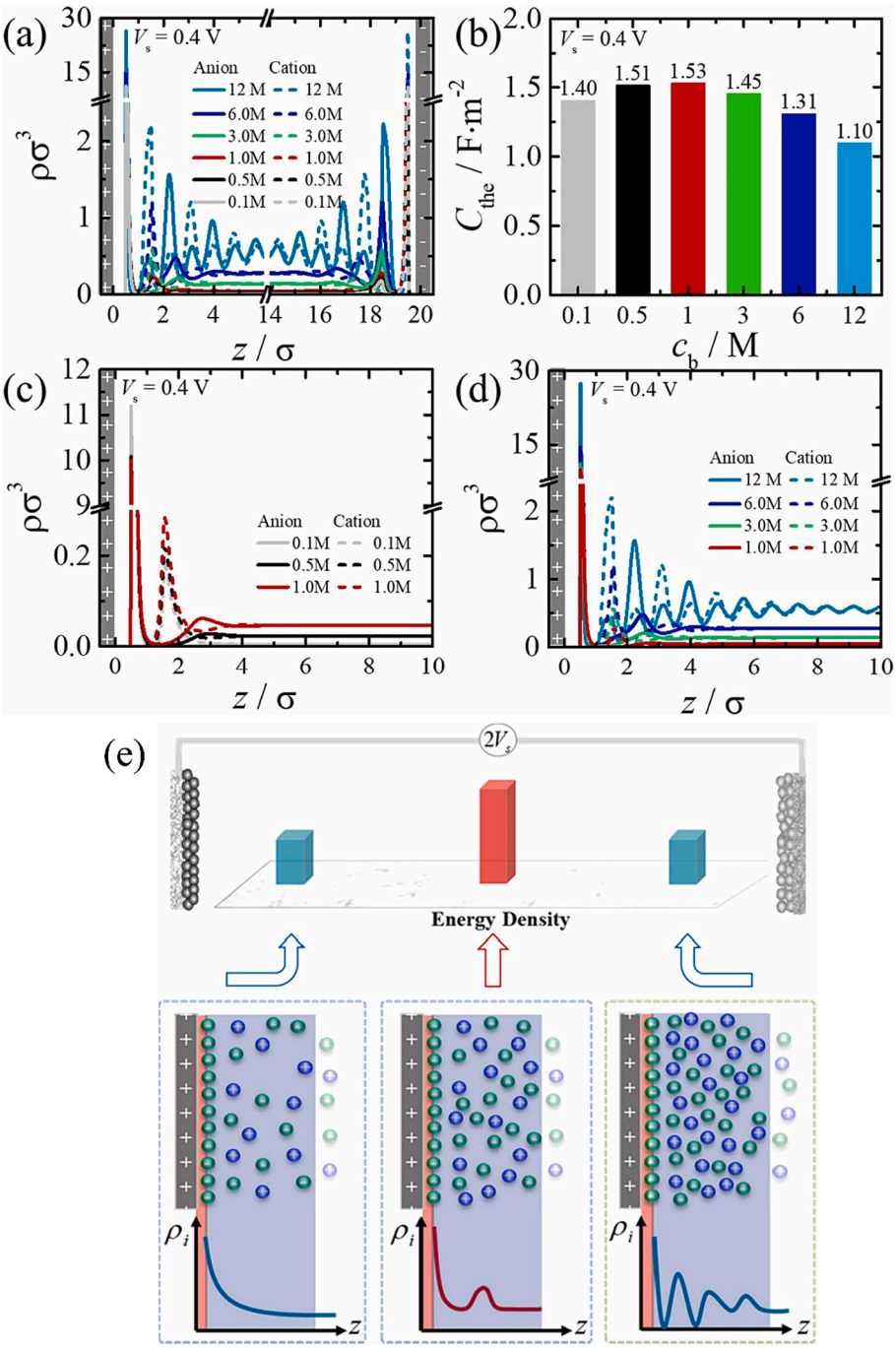

Fig. 21. (a) Theoretical prediction of ions distribution and (b) theoretical capacitance at different concentrations of electrolyte. (c, d) The ions distribution at the positively charged surface. (e) An illustration of how the ion distribution at the interface of electrodes influences the energy density of supercapacitors. A few multilayered stackings of ions near the electrode surface are supposed to have a high energy density. Reproduced with permission [259] copyright 2022.

layer is a reciprocal sum of the capacitance of the stern layer "Cs" and the capacitance of the diffusion layer "Cd." The stern layer capacitance, namely $Cs = \varepsilon_o\varepsilon_r/d$, where ε_r is the relative permittivity, ε_o is the permittivity of free space and "d" is the space set as half of the diameter of the solvated ions σ. The electrolytes were represented by a restricted primitive model (RPM)[260] where anions and cations were modeled as solid hard spheres having an identical solvated dimension ($\sigma_+ = \sigma_- = \sigma = 0.425$ nm). Cd is set as the capacitance of the diffusion layer with relation Cd = Qs/Vd, where Qs is the surface charge density in the diffusion layer and Vd is the drop in potential across the diffusion layer. They also defined a quantity ρ(r), which stood for a series of spatial density distribution for all ionic components and a charge valence state by "Z" (For monovalent ions $Z\pm = \pm 1.0$). The CDFT model predicted different density distributions of the cations and the anions at different concentrations of the electrolyte, as shown in Fig. 21 (a). When the concentration is 0.1 M, the anions (i.e., the hydroxide ions) closely stack themselves at the positively charged surface and the cations (i.e., the potassium ions) arrange themselves in close proximity to the negatively charged surface just like the EDL, which is followed by a diffusion layer. It was clearly visible that there were hardly any other distribution intensity peaks between the cathode and the anode (with 0.1 M). However, when the concentration was increased beyond 0.1 M, the other peaks started to appear. The multiple peaks obtained in the study at higher concentrations correspond to an alternating multilayer distribution of cations and anions. The cation distribution peaks are pretty similar to the anion distribution peaks, with the only difference being that they are found close to the

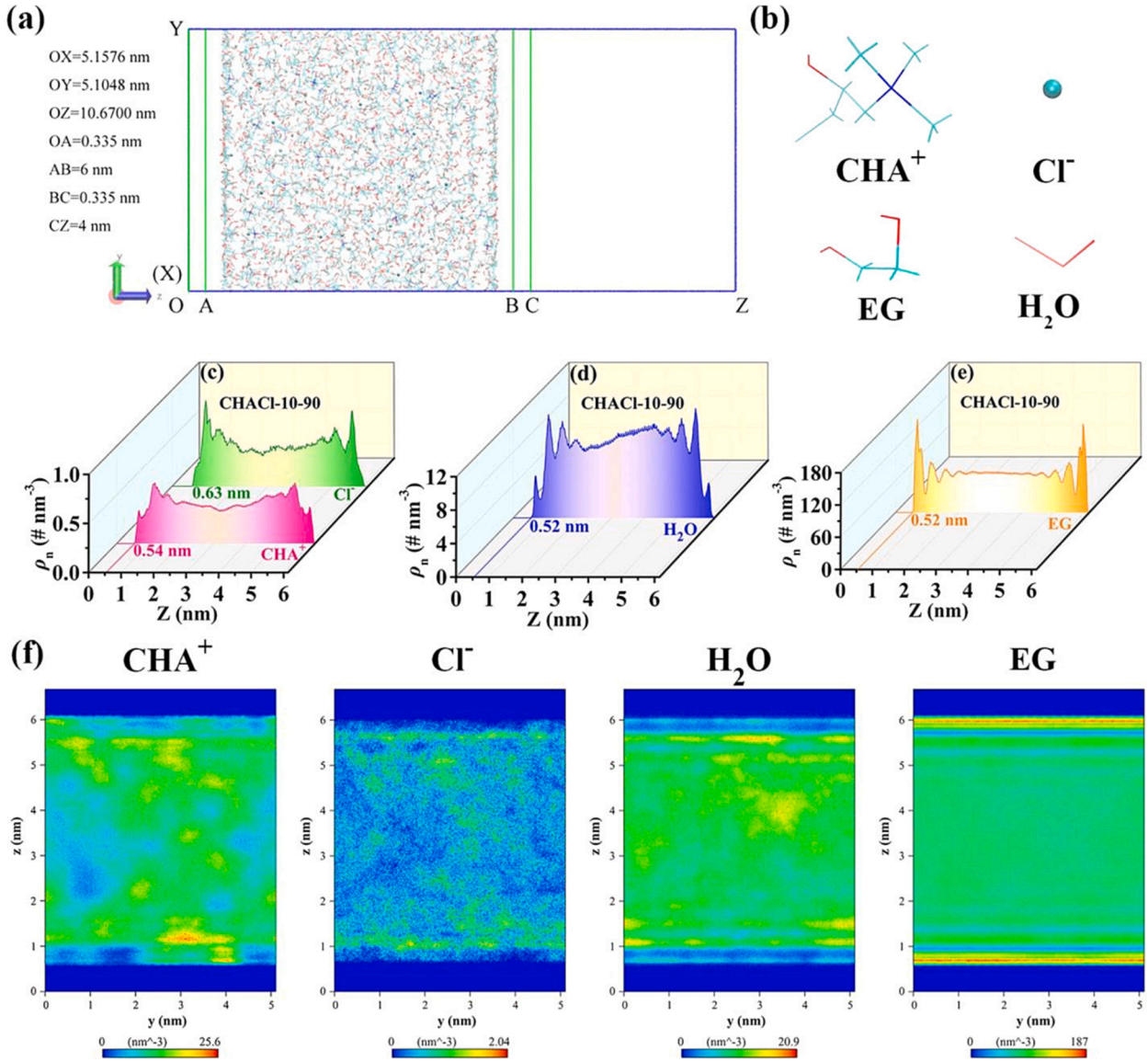

Fig. 22. (a) Schematic of the simulation system composed of the electrolyte surrounded by two planar carbon electrodes. (b) Individual components in the electrolyte. (c–e) Number density distributions of CHA+, Cl–, H2O, and EG in CHACl-10–90 simulation as a function of distance from the electrode (z) under 1.8 V. (f) Number density distribution maps of CHACl-10–90 as a function of the YZ plane under 1.8 V. Reproduced with permission [262] copyright 2022.

negatively charged electrode.

As the concentration of ions is increased from 0. 1 M to 1.0 M, an interesting phenomenon is observed at both electrode surfaces (Fig. 21 (b)). The distribution is shown in Fig. 21 (c) and 21 (d). At the positive electrode, clearly, the interfacial density of the anions decreases, but at the same time, in the adjacent layer (in the multilayer distribution), the density of cations increases. This phenomenon results in the "decrement" of the "potential drop Vd" in the diffusion layer (at the positive electrode). When Vd becomes smaller in the diffusion layer at the positive electrode, simultaneously on the negative electrode, the interfacial distribution of cations reduces, and an increase in anion distribution is observed. This, in turn, reduces the "potential drop Vd" in the diffusion layer (at the negative electrode). Since Cd = Qs/Vd gives the diffusion layer capacitance, the Cd value is increased on both electrodes. This increased Cd value also increases the total capacitance of the device. However, when the electrolyte concentration is increased from 1.0 M to 12 M (shown in Fig. 21 (d), the interfacial density of anions and cations increases monotonically. Hence, the corresponding potential drop in the diffusion layer (Vd) and surface charge density (Qs) increase by the same factor. Therefore, even if there is an advantage due to potential drop, it gets nullified by increased surface charge density. Thus, no capacitance increase is observed because of the increasing electrolyte concentration beyond a certain critical value (of 1.0 M in this case). This is an important finding in interfacial ion distribution and kinetics study. This finding is schematically represented in Fig. 21 (e).

Molecular crowding is also an emerging concept to enhance the voltage window of the supercapacitors (especially in aqueous media) using the delayed kinetics at the electrode–electrolyte interface [261]. Wu et al. [262] demonstrated an extension in the voltage window of activated carbon-based symmetric supercapacitors using a simple strategy of surrounding the H_2O molecules electrolyte solvent with a small molecular crowding electrolyte (SMCE) via ethylene glycol (EG) agent. Different formulations of SMCEs were prepared by continuously adding and separately mixing EG to 3-Chloro-2-hydroxypropyltrimethyl ammonium chloride (CHACl, 60%

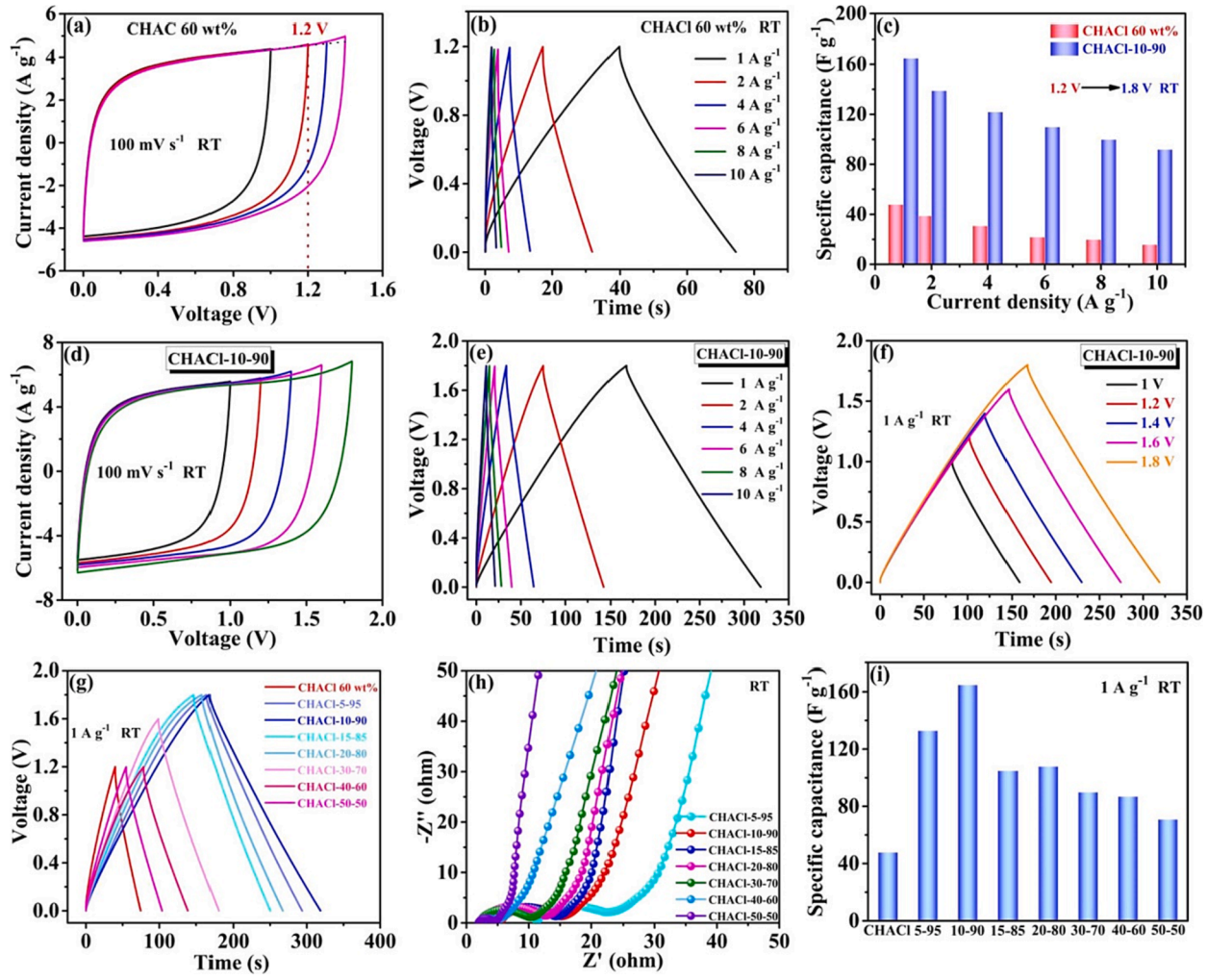

Fig. 23. (a and b) CV and galvanostatic charge–discharge (GCD) curves for the pristine CHACl measured at RT. (c) Specific capacitances for CHACl and CHACl-10–90 electrolytes. (d and e) CV and GCD curves for the CHACl-10–90 electrolyte measured at RT. (f) GCD curves measured from 1 to 1.8 V. (g–i) GCD curves at 1 A g–1, Nyquist plots, and specific capacitances at 1 A g–1 for the pristine CHACl and different CHACl-H2O-EG electrolytes. Reproduced with permission [262] copyright 2022.

mass fraction in H_2O), with H_2O: EG in the weight ratio of 5:95, 10:90, 15:85, 20:80…50:50. Further these SMCEs were sandwiched between activated carbon electrodes and assembled in the form of CR2032 type coin cells which were tested for electrochemical performance. Molecular dynamic studies were also performed, as shown in Fig. 22, revealing some critical arrangements of molecules at the electrode–electrolyte interface, which could drastically impact the voltage window of the device. Through molecular simulation dynamics Wu et al. [256] dissected the number density of CHA^+, Cl^-, H_2O and EG at the electrode electrolyte interface among the pristine, CHACl, CHACl-10:90, and CHACl-5:95 electrolytes. Fig. 22(a) shows the rearrangement of the electrolytes, which is closer to real physical states when a potential is applied between two carbon electrodes. The participating ions and molecules are shown in Fig. 22(b). The number density distribution of these participating ions and molecules at the electrode–electrolyte interface for CHACl-10:90 electrolyte is shown in Fig. 22 (c-e). CHA^+, Cl^-, H_2O, and EG present a multilayer distribution at the surface of the electrode owing to their Vander-wall and coulombic interactions, as shown in Fig. 22(f). Notably, the ordered CHA^+, Cl^-, H_2O and EG appear at a distance of 0.54, 0.63 and 0.52 nm from the electrode surface, as shown in Fig. 22 (c-e). The distribution of CHA^+ and CL^- shift more towards the bulk of electrolyte at about 1.2 and 1.8 nm away from the electrode surface, respectively. The important point to note here is that the H_2O and EG exhibit distinct alternating layered distribution and the number density of the first layer of EG (175 #nm^{-3}) is much higher than the first layer of H_2O (5# nm^{-3}), which is also in agreement with the result of Fig. 22(f). Interestingly, when pristine CHACl was run through the same molecular simulation dynamics, the ordered H_2O, CHA^+ and Cl^- began to appear at 0.5, 0.52 and 0.63 nm distance from the electrode surface. It is revealed that the number density of H_2O molecules was 10 times higher (47# nm^{-3}) than that of CHACl-10:90 at the electrode–electrolyte interface in the typical bilayer distribution model. These results indicate that the presence of EG significantly affects the distribution of H_2O molecules at the electrode–electrolyte interface. EG squeezes out the H_2O molecules from the interface; hence, when the voltage window at the interface crosses the theoretical decomposition limit of H_2O (i.e., 1.23 V). The overall electrolyte composition still survives to an extended voltage range since there is very little H_2O presence at the electrode–electrolyte interface junction.

In order to assess the electrochemical performance of the CHACl pristine vs. CHACl-10:90 electrolyte with molecular crowding, Wu et al. [262] performed the rate capability tests, cyclic voltammetry (CV) at different scan rates and galvanic charge–discharge (GCD) tests at various current densities on the fabricated activated carbon-based symmetric CR2032 type coin cells. The results are shown in Fig. 23. Fig. 23 (a-c) shows the results on pristine CHACl where the cell was scanned from 0 to 0.8, 1.2 and 1.4 V. Though in Fig. 23 (b), the iR voltage drop in the GCD performed (at 1.2 V) was less than 0.05 V exhibiting no obvious water decomposition, the rate capability and coulombic efficiency (51%) was inferior when estimated using the integral area of the discharge curves. On the other hand, when the same CV and GCD tests were conducted on the CHACl-10:90 electrolyte (which had EG in it), the voltage window could be easily extended to 1.8 V with columbic efficiency greater than 74%, as shown in Fig. 23 (d-f). This extension in the voltage window was clearly attributed to the small molecular crowding effect caused by EG molecules over water.

Overall it can be argued that the actions happening on the electrode–electrolyte interface could severely impact the potential window of the device. It often occurs due to the formation of an artificial interface like SEI, which passivates the pre-existing detrimental surface functionalities. On the other hand, researchers have confirmed that the other forms of carbon, like graphene and carbon nanotubes (CNT), are more stable in the larger voltage range (than the AC) because of reduced surface defects and functionalities [233]. Similarly, soft carbon, hard carbon, and carbon black can also help in the extension of the voltage window owing to a lower density of surface defects [263,264].

In comparison to surface modification treatments, electrochemical activation of the electrode surface gives many impressive results of electrode performance in a higher voltage range. Morita et al. [265] figured out that KOH-activated soft carbon offers a much superior specific capacitance value of 130 Fg^{-1} than its pristine form. Soft carbon already possesses a larger voltage window due to the low density of surface defects through electrochemical activation. However, they further attain more stability due to the intercalation of activating agents forming sporadic depositions on the defect sites and, blocking them and establishing ion channels within the electrode material. This inhibits electrolyte decomposition at a larger voltage window, extending the overall voltage range of the device.

7.3. Effect of electrode configuration on the voltage window

Though asymmetric supercapacitors already enlarge the voltage window in pseudocapacitors (like metal oxides) by virtue of the difference in their work function, electrode configuration of a hybrid nature can extend the voltage window in the double-layer capacitors [61]. Hybrid configuration refers to an arrangement where one electrode exhibits charge storage via diffusion controlled-solid state ion intercalation/de-intercalation (battery type) while the other electrode stores charge on the surface (like capacitors) [266]. Among the two types (battery and capacitor) of electrodes, the capacitor electrode must show a wide, stable potential window in this configuration [267]. A typical example of a hybrid supercapacitor for carbon-based materials would be a lithium-ion capacitor (LIC), which initially has activated carbon and graphite as positive and negative electrodes, respectively. Since the intercalation potential of Li^+ is very negative (0 V vs. Li/Li^+) and the upper potential limit of positive AC electrode can go as high as 4.3 V (vs. Li/Li^+), the combination of both electrodes could give a high cell voltage of 3.8 V to 4.1 V [268]. Due to the Li^+ ion intercalation and de-intercalation, this hybrid configuration provides much superior energy density and has shown its potential to be used as future supercapacitors replacing organic EDLCs [64,269,270]. There is another promising combination of electrodes for this hybrid configuration: LTO//AC, where LTO is lithium titanium oxide ($Li_4Ti_5O_{12}$), which is an excellent negative electrode material exhibiting high rate (for LIBs) and shows “zero strain” effect during charging and discharging [271]. This enables a superlong cycle life even at elevated voltages. But using it in combination with graphite(-ve electrode), the overall specific energy of the device is reduced because the potential plateau of Li intercalation–deintercalation in LTO (1.55 V vs Li/Li^+) is much higher than that in graphite (~0 V vs Li/Li^+).

A carbon-based, hybrid supercapacitor design that utilizes alkali-ion intercalation–deintercalation on materials like graphite, hard carbon, and soft carbon can further endure the lower potential limit on these negative electrode materials. Due to this reason, the design can achieve a much higher energy density due to its extended stable potential window and enhanced charge storage ability. At the same time, the other electrode must exhibit a capacitor-type performance, which could facilitate achieving high power density and quick reversibility for full-cell performance. Meanwhile, if materials like soft carbon could be used as positive electrode material, the positive potential can be further extended. This would help to achieve a high voltage window for the overall device [272]. However, in order to achieve a high practical working voltage, the upper and lower limits of the overall device should be optimized and checked for stability [249,273].

In order to verify the high voltage range of any electrode configuration, conducting a floating-GCD cycling test is recommended. In this test, the devices are first kept at a high constant voltage supply for a prolonged period of time, then periodically cycled at a rate of 10C for 50 cycles. This floating-GCD cycling test is a high-stress condition test. The device is kept at an extreme voltage for a reasonably long time, which is enough to initiate the irreversible reactions that could degrade the electrodes if it is not naturally stable in that voltage range. If the electrode is not stable during the sustained higher voltage, with the onset of GCD cycling, its capacitance decreases dramatically, signaling the material degradation and its inability to show a large voltage window. However, in a hybrid configuration, since the charge storage mechanisms are different on different electrodes, it could be challenging to get a stable performance during a float test. However, a few studies, like that of Cao et al. [273], have demonstrated the method to correctly determine the charge capacities of both positive and negative electrodes, simultaneously improving the power and energy density of the hybrid configuration.

8. Influence of electrolytes on the voltage of supercapacitors

Generally, supercapacitors can use a wide variety of electrolytes, but they can be broadly classified into three categories based on the electrolytes used [274] (i) aqueous electrolyte based, which means ions in water (ii) organic electrolyte (OE) based, which means ions in an organic solvent, and (iii) ionic liquid (IL) based (which is pure liquid salts). The stability of the electrolyte is one of the most important factors in determining the operating voltage in the design of a supercapacitor. The ionic conductivity and electrochemical stability of the electrolytes may also determine the rate capabilities and cyclic performance of the supercapacitors.

Aqueous electrolytes have a specific salt or combination of salts dissolved to obtain the necessary ions [275]. These aqueous electrolytes may further be classified into acidic (e.g., H_2SO_4), alkaline (e.g., NaOH), and neutral (e.g., Na_2SO_4) electrolyte categories. Generally, aqueous electrolytes show excellent ionic conductivity (~1 S cm^{-1}), non-flammability, low cost, and processability. Due to their higher electronic conductivity, high dielectric constant, smaller size ions and larger accessible surface area, supercapacitors using aqueous electrolytes show better capacitance compared to the devices with the same electrode in OEs. However, due to the smaller thermodynamic stability potential window of water (~1.23 V), aqueous electrolyte usage may restrict the electrodes' operational voltage range [93,276–280]. Also, aqueous electrolytes show moderate stability and durability for a long-term cycling life compared to other electrolytes. On the other hand, using alkaline or acidic electrolytes may corrode the active electrode material. Hence, a combination may be wisely chosen while working with acidic or alkaline electrolytes. Thus, it is essential to understand the requirement of the electrolyte to be used with a given set of electrodes. Though a smaller potential range of aqueous electrolytes may limit their capability to enhance higher energy densities, they can be very useful if priority is given to factors like high power density, handling safety, large-scale production, and low cost.

ACN

Recently, researchers have reported that neutral aqueous electrolytes successfully sustain a wide potential window of about 1.6 to 1.9 V [278,279]. It is beyond the theoretical limits of the stable potential range of water decomposition, 1.23 V [280]. This is because of the high hydrogen evolution overpotential and the OH^- ion generation potential within the neutral aqueous electrolyte. Considering a potential beyond 2 V, the aqueous electrolytes are replaced with OEs and ILs. Supercapacitors that employ OEs can easily reach up to 2.5 ~ 3.5 V. Upon using ILs, they can sustain up to 4 V [70,274,281–283]. Energy density can be significantly enhanced by increasing the potential window. Another advantage is that it is necessary to employ fewer devices in series while using these high-voltage supercapacitors (with ILs) to get the same target voltage. The high potential window of these OEs and ILs depends on several key factors, like the type of conducting salts (i.e., anions and cations) and solvents and traces of impurities (e.g., water).

Different types of OEs have been used in the supercapacitor community. ACN and PC have been very popular among them. ACN has a very high solubility for different salts and has the highest ionic conductivity than most other OEs. Unfortunately, it is highly toxic, not environmentally benign, and poses a challenge during waste disposal and recycling. Though not all OEs may pose environmental hazards, their flammability leads to fire hazards in energy storage devices. On the other hand, PC is much more environmentally friendly but lower in ionic conductivity. However, it can also provide a high operating temperature range and a wider operating potential window. But it must be sealed very well to keep moisture levels below 3–5 ppm [274]; otherwise, it will undergo severe performance degradation, reduce the voltage window, and pose some safety issues.

An IL is a salt that remains in a liquid state above a certain temperature when the surroundings can provide enough thermodynamic energy greater than its lattice energy, causing the salt to melt. These ILs have shown phenomenal properties for supercapacitors, like very low vapor pressure, low flammability, high thermal and chemical stability and a very high working potential range of 2 to 6 V, which typically is around 4.5 V [284]. Though, in comparison to aqueous and OEs, ILs suffer from low ionic conductivity. Nevertheless, it is a good candidate for high-performance and high-voltage supercapacitors. Also, since IL does not include any solvent and solvated

ions, no solvent atom-shell is formed around the ions. As a result, the size of the ions is well-defined. Therefore, ion dynamics study is easier for charge storage mechanism via EDLC behavior.

Though OEs and ILs (non-aqueous electrolytes) are better in terms of operational voltage compared with aqueous electrolytes, due to their higher viscosity, ionic transport becomes sluggish. The ionic conductivity is reduced at least by an order of magnitude in OEs and ILs. This is also marked by an increase in the internal resistance of the supercapacitor. Thus, supercapacitors made with OEs and ILs generally do not go beyond 200F/g and exhibit comparatively lower power density.

8.1. *Energetics of electrolytes*

Along with the redox potential window of the active electrode materials, the stability of the electrolyte also determines and often limits the output voltage of the supercapacitor. While choosing the best combination of active electrode materials, selecting the appropriate electrolyte material that should thermodynamically sustain the potential window of the supercapacitor is also essential. The electrolyte provides the necessary cations, anions, and a liquid medium, which is a platform for the ionic movement. Each electrolyte is stable within a potential range and may breakdown if the operating potential of the device goes beyond that range. This stable potential range may be affected by factors like the type of ions generated, solvent, and degree of purity [274].

It can be observed that, in general, pseudocapacitive supercapacitors work in a voltage range that goes beyond the very narrow electron transfer potential range of the individual electrodes. However, methods and principles to determine the overall potential range in pseudocapacitive supercapacitors remain very similar to batteries. Fig. 24 explains the potential window of the active electrode materials and their interaction with the energetics of the electrolyte. It shows the highest occupied molecular orbital (HOMO) and lowest unoccupied molecular orbital (LUMO) of the electrolyte solvent/medium (water in the case of aqueous electrolyte). The bandgap (E_g) provides the separation gap between LUMO and HOMO. The term μ_C and μ_A represents the electrochemical potentials of the cathode and anode, respectively. The Φ_C and Φ_A show the cathode and anode work functions, respectively. Electrolyte solvent remains thermodynamically stable as long as the potential of the device sweeps within this range of E_g [285].

As discussed in the previous sections, any material's electrochemical potential arises from its fermi level. Therefore, when these materials are chosen as electrodes for a supercapacitor, they are carefully examined in combination with a certain electrolyte solvent, which is thermodynamically favorable in terms of their energy levels. For a redox reaction to happen at the interface of the electrode and the electrolyte, depending upon the direction of charge transfer, the energy levels at or near the fermi level (in the electrode) must match with a suitable empty (LUMO) orbital or an occupied orbital (HOMO) of the electrolyte solvent. At the same instant, there should be an applied potential (V) on the electrode, which must change the electron work function of the electrode active material from ϕ to $\phi \pm neV$ to achieve a facile electron transfer between the electrode and electrolyte ions. This potential V is equivalent to the electrochemical potential (μ) $\pm$ the surface dipole (δ), equating it to the work function for the electrode material. As shown in Fig. 24, when the LUMO energy level of the electrolyte matches with the electrochemical potential μ_C for the positive electrode (cathode) and the HOMO energy level of the electrolyte solvent matches with the electrochemical potential for the negative electrode (anode), we observe a charge transfer across the electrode–electrolyte solvent interface which is undesirable for supercapacitors. This picture shows an ideal selection of materials for a very conducive and effective charge transfer. However, it may not be viable while making an actual supercapacitor device. Suppose the value of μC becomes smaller than the LUMO level of the electrolyte. In this case, the electrolyte solvent will undergo a reduction reaction unless it forms a passivation layer to counter the transfer of electrons from the

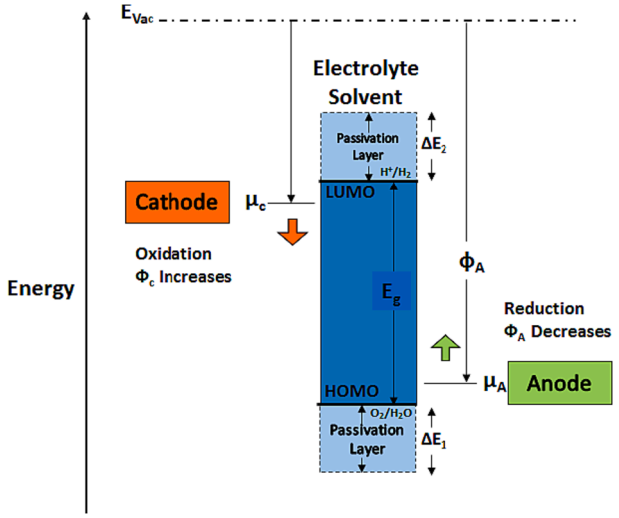

Fig. 24. Schematically represents the energetics of an electrolyte and its interaction with the electrodes for electrolyte solvent decomposition. In the figure, μ_C and μ_A represent the cathode and anode electrochemical potentials, respectively. Φ_C and Φ_A are work functions of the cathode and anode, respectively.

cathode to the LUMO of the electrolyte.

Similarly, if the value of μ_A becomes higher than the value of HOMO of the electrolyte solvent, the electrolyte solvent will be oxidized unless it forms a passivation layer to obstruct the electron transfer from the HOMO of the electrolyte to the anode [286]. Thus, an attempt is made such that both electrochemical potentials (μ_C and μ_A) for the positive and negative electrodes should lie within the range of HOMO and LUMO of the electrolyte solvent, which is nothing but E_g. In an aqueous electrolyte system, generally, the operation voltage range is limited by the low thermodynamic stability potential window of water. However, for an actual working device, a passivation layer is formed on the interface of the electrode and electrolyte solvent, giving kinetic stability to the electrolyte and causing an overpotential for H_2 and O_2 evolution. In other words, because of this passivation layer of the electrolyte, the actual device can operate in a voltage range beyond the thermodynamically stable potential window of the electrolyte solvent. In the next section, we discuss the causes of the formation of this passivation layer and the overpotential resulting from it.

8.2. *Overpotential and passivation layer formation in aqueous electrolyte-based supercapacitor electrodes*

As discussed above, in an aqueous electrolyte system, the operational voltage range of the device can further be extended because of

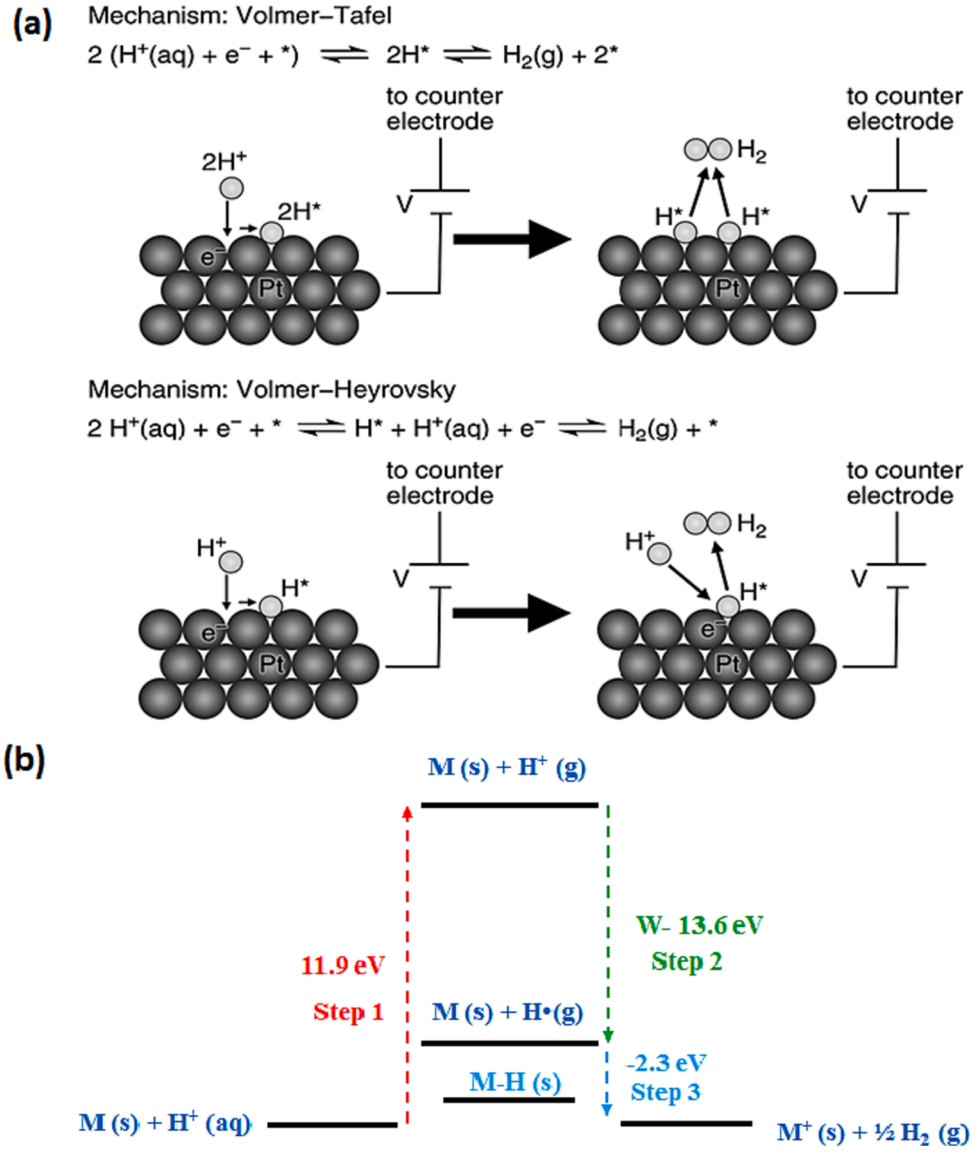

Fig. 25. (a) Schematic illustration of the two possible mechanisms for hydrogen evolution on platinum (Pt) electrode (1) Volmer-Tafel and (2) Volmer-Heyrovsky. The (*) represents a free active site, while H* indicates the neutralized hydrogen atom attached to the free active site. Reproduced with permission from ref. [292] (b) Energetics of the multistage hydrogen evolution process, where M is any metallic electrode and H is hydrogen. Reproduced with permission from ref. [293].

the overpotential generated for H_2 and O_2 evolution at the negative and positive electrodes, respectively [277,279,287–289]. For example, hydrous RuO_2 shows a reversible cyclic voltammogram with peaks at 0.05 V and 1.4 V (range vs. reversible hydrogen electrode, RHE). This range exceeds the thermodynamic decomposition limit of water [40]. Overall, three key factors determine the operating voltage range of a supercapacitor: i) standard potential range of each electrode, which is based on μ_p ($_p$ = positive, cathode) and μ_n ($_n$ = negative, anode), ii) stable thermodynamic potential range of the electrolyte, iii) passivation layer formed at the electrode–electrolyte interface, which causes the overpotential for H_2 and O_2 evolution on the negative and positive electrodes respectively (in case of aqueous electrolyte). Fig. 24 shows how an asymmetric supercapacitor using an aqueous electrolyte achieves the overpotential (ΔE_1) for O_2 evolution at the positive electrode (e.g., RuO_2 and MnO_2) and the overpotential (ΔE_2) for H_2 evolution at the negative electrode (e.g., VN or Fe_3O_4), further extending the practical potential window of water decomposition and thus expanding the window up to 2 V [287,290]. Extending the potential window will significantly enhance the energy density of the device.

Overpotential is defined as the excess potential from the thermodynamically determined half-reaction reduction potential that needs to be applied to observe the reduction phenomenon on an electrode experimentally [291]. In simple words, it means that the electrode (while charging) requires more energy to drive the redox phenomenon (in regards to electrolyte) than expected. The quantity of overpotential is specific to each supercapacitor design and varies across the device depending upon multiple factors like the reaction rate of each step in evolution reaction, mobility of ions, rate of accumulation of ions on the electrodes, the ratio of current density (i) and exchange current density (i_0). To understand the influence of these factors, we need to understand the mechanism of H_2 or O_2 evolution reactions on any general electrode. Fig. 25 (a) shows two possible mechanisms for hydrogen evolution reaction (HER), which are given by (1) Volmer-Tafel and (2) Volmer-Heyrovsky [292]. From both mechanisms, it is clear that the evolution reaction is not a one-step but rather a multistage energy exchange process. Fig. 25 (b) schematically shows the energy exchange for each step in the HER [293]. All of these steps have different energy requirements and also different reaction kinetics and rate. Generally, the slowest step is the rate-determining step and may delay the process of evolution, causing the accumulation of H^+ ions (waiting to discharge), which prevents further incoming H^+ ions. This chemisorption of H^+ ions forms the passivation layer on the cathode [293].

Like hydrogen evolution, oxygen evolution is also a multistage energetics process and involves multiple steps with its own reaction kinetics. Generally, the slowest step determines the rate of OH^- ion adsorption and the oxygen evolution at the anode. So, in general, any evolution reaction at the electrode can be divided into the following stages [294].

(1) Mass transport: i.e., the transport of the reactant ions from the bulk electrolyte to the electrode–electrolyte interface.
(2) Surface conversions precede the electron transfer, i.e., rearrangement of reactant molecules/ions, adsorption of ions to the electrode surface, chemical reactions such as protonation or complex dissociations, etc.
(3) Electron transfer process between the electrode and the electrolyte solvent.
(4) Surface conversion after the electron transfer: which includes chemical reaction via bond formations, complex formations, desorption from the electrode surface, etc.
(5) Mass transport: i.e., the product movement from the electrode surface to the bulk electrolyte.

Out of these five steps, the slowest step generally determines the rate of the overall evolution reaction and is the main cause of the formation of the passivation layer. In practice, every step occurs at a non-infinite rate and could be the source of overpotential. If the "current density i (A/m^2)" entering/leaving the electrode is higher/lower than the "exchange current density i_0 (A/m^2)"-which is involved in the electron exchange between the electrode and electrolyte, we could get an overpotential given by Tafel eq. [294]

$$\eta = A \times log\ (i\ /\ i_0) \tag{35}$$

where A is Tafel slope and η is the measured overpotential. The overpotential can be divided into three main categories: Ohmic overpotential (η_o), activation overpotential (η_a), and concentration overpotential (η_c). In any electrode–electrolyte setup, the overpotential could be calculated by the summation of these three contributions.

8.3. Effects of electrolyte's pH on overpotential and voltage window of the supercapacitor

The pH of an electrolyte is a measure of the concentration of H^+ and OH^- ions in the solution, which actively take part in the charge storage mechanisms of a supercapacitor by either 1) solvating electrolyte ions (for EDLC mechanism) or 2) directly taking part in the redox charge transfer process (for pseudocapacitance). Mathematically, it is defined by the negative decimal logarithm of the activity of hydrogen ions [295].

$$pH = -log_{10}(a_{H^+}) = log_{10}\left(\frac{1}{a_{H^+}}\right) \tag{36}$$

Similar to pH, the concentration of OH^- ions is given by $pOH = pK_w - pH$ (where K_w is the self-ionization constant of water). We have discussed previously that both HER and oxygen evolution reaction (OER) in a supercapacitor electrolyte are highly dependent on the kinetics of the process because of the involvement of multiple steps like ion transport, adsorption, charge transfer, bond-formation and release. Any increase or decrease in the concentration of these ions (reflected in the pH) affects the onset of HER and OER. The H^+ and OH^- ions in many of the reported aqueous supercapacitors directly participate in the charge storage by redox reactions [296,297]. Since pH is a direct measure of the concentration of H^+ ions and OH^- ions in an electrolyte solution, it can be established that pH plays a pivotal role in determining the overpotential and thereby affecting the voltage window.

For an aqueous electrolyte, a pH of 7 indicates its neutral nature. Any value above it makes the electrolyte alkaline, while anything below makes it acidic. Considering a simplified model of only double-layer capacitance, acidic or alkaline electrolytes in carbon-based supercapacitors can reach a maximum of 0.8- 1.2 V. In contrast, the ones with neutral aqueous electrolytes have reached a much higher value of 1.4–2.0 V [93,277,279,298,299]. In order to investigate this, Abbas et al. [276] studied the mechanism of overpotential for an activated carbon electrode in 1 M Li_2SO_4 (pH = 6.5) and 1 M $BeSO_4$ (pH = 2.1) electrolytes (refer Fig. 26). The thermodynamic potential for HER was first confirmed using the Nernst eq. (P_{HER} = -0.059 pH) against the standard hydrogen electrode (SHE). For 1 M Li_2SO_4(pH = 6.5), it reached around −0.384 V vs SHE, while for 1 M $BeSO_4$ (pH = 2.1), it reached about −0.124 V vs SHE. These are marked with dashed red lines in Fig. 26. It was observed that the perturbation in the current due to HER in 1 M Li_2SO_4 (pH = 6.5) started only after −0.8 V, indicating a high overpotential of 416 mV, while in 1 M $BeSO_4$ (pH = 2.1), only 176 mV of overpotential was observed due to early HER at −0.3 V. Hence it is clear that near-neutral aqueous electrolyte with pH around 6.5 has a higher overpotential when compared to acidic aqueous electrolyte with pH 2.1.

Whitacre and his co-workers investigated large overpotential in neutral aqueous electrolytes by a unique in-situ mechanism [299]. They used a needle-tip micro pH sensor within a tiny region, very close to the electrode–electrolyte interface while charging an activated carbon electrode. A range of electrolytes (with different pH from 1.89 to 10.48) was chosen for cathodic charging. Interestingly, all the pH tends to approach a value of 11 except the most acidic 1.89. This was attributed to the fact that with the onset of charging, H^+ ions near the electrode–electrolyte interface are quickly consumed, or there is a high production of OH^- ions near the electrode–electrolyte interface, accompanied by the production of nascent hydrogen (as shown in Fig. 25 (a)). But in the case of the highly acidic or basic environment, with moderate consumption of H^+ ions or production of OH^- ions, it might go undetected. However, in the case of neutral aqueous electrolytes, since the excess concentration of H^+ and OH^- ions are too low, there might be a sudden change in the pH at the interface as the H^+ ions are produced by slight water reduction, which again diffuses into the solution. Therefore, through classical Pourbaix behavior, a gradual transition of the potential results in a large overpotential for HER, in neutral aqueous electrolytes. Very similar behavior is observed for OER in neutral aqueous electrolytes, which extends the upper limit of the stable potential window [93,277,300]. This effect could be more prominent in the case of porous electrodes, where the movement of both ions and electrons is diffusion-controlled.

As we discussed in section 6.2, HER is a multistep process that involves: Mass transport of H^+ ion from the bulk of electrolyte (to electrode surface), adsorption/ chemisorption, bond formation, and release; one step may be favored over others. For example, 'adsorption of hydrogen ion' may be favored over 'formation of nascent hydrogen' since the latter can only be achieved once the potential is high enough to supply the necessary activation energy. This causes an accumulation of H^+ ions near the electrode surface, which is depicted by a sharp decrease in pH near the electrode surface. Particularly, in neutral aqueous electrolytes, these accumulated excess H^+ ions may also facilitate and increase the pseudocapacitance by directly participating in the redox charge transfer. Therefore, an enhanced hydrogen storage capability may be observed in a neutral pH electrolyte, which would be marked by an increase in capacitance. This could be directly attributed to hydrogen evolution overpotential. Hence, the pH of an electrolyte could be a critical factor in determining overpotential (thereby affecting voltage window) and increased redox activity of H^+ and OH^- ions, increasing capacitance. However, due to the lack of a quantitative study in this area, the entirety of the effect of pH is still poorly understood.

8.4. Aqueous electrolyte systems

The aqueous electrolyte-based supercapacitors have several advantages over other electrochemical energy storage devices that

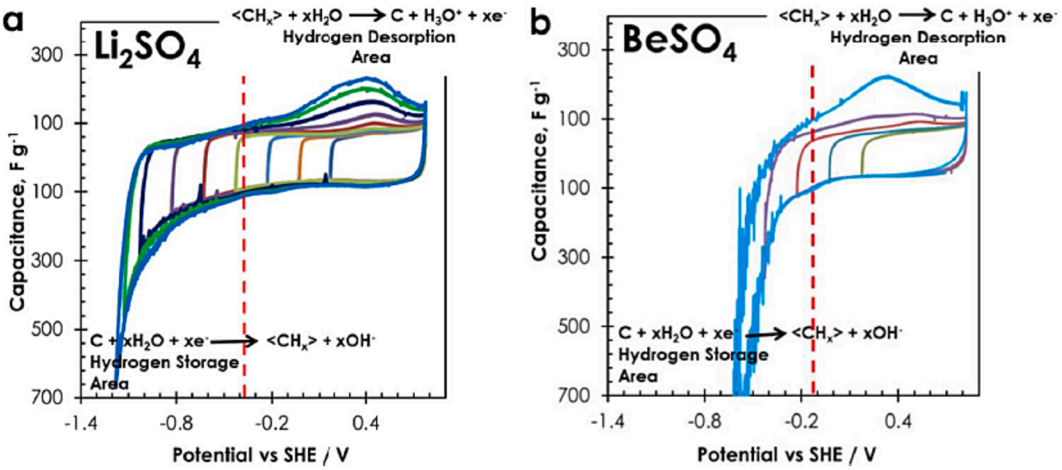

Fig. 26. Plots reported by Abbas et al. [276], where an activated carbon electrode is investigated for hydrogen evolution overpotential (onset of HER) in two different electrolytes (a) neutral aqueous electrolyte: 1 M Li_2SO_4 with pH = 6.5 (b) acidic aqueous electrolyte: 1 M $BeSO_4$ with pH = 2.1. In both (a) and (b), CV studies are performed at a rate of 2 mV s^{-1} by a stepwise decrease of negative cut-off potentials. Reproduced with permission from reference [276] Copyright 2020, The electrochemical society.

employ organic and ionic liquid electrolytes. They are economical, safe, nontoxic, and have high ionic conductivity. The only drawback with the aqueous electrolyte is the decomposition of water occurring at 1.23 V, which severely impacts the supercapacitor's working voltage, leading to poor energy density. Depending on several factors like pH, salt concentration, etc., each electrolyte has its own stable potential window, which majorly dictates the overall voltage output obtained from the supercapacitor. Water decomposition happens via HER at the negative electrode and OER at the positive electrode. Depending on various electrode and electrolyte combinations, an overpotential is required for the HER and OER mechanisms to happen. This overpotential plays a major factor in obtaining an extended voltage window compared to the actual potential difference between electrodes and the stable voltage window of the electrolyte. Significant effort has been made to obtain extended potential window using aqueous electrolytes in supercapacitors following approaches like i) using neutral aqueous electrolyte, thereby not introducing additional H^+ or OH^- ions leading to early onset of hydrogen or oxygen evolution; ii) developing hydrogel electrolyte, and iii) developing water in salt electrolyte to completely restrict the water decomposition.

8.4.1. Neutral electrolyte

The aqueous electrolytes are broadly classified into acidic (e.g., H_2SO_4), neutral (e.g., Na_2SO_4) and alkaline (e.g., KOH) based on the salts used. These electrolytes have a range of pH from 1 to 14, which represents the concentration of H^+ and OH^- ions in the electrolyte. Among these aqueous electrolytes, the neutral electrolytes (i.e., Na_2SO_4, Li_2SO_4, K_2SO_4) employed in supercapacitors have a pH of 7, i.e., they don't have H^+ or OH^- ions in the system. These electrolytes aid in achieving a high voltage window by restricting water electrolysis due to the HER or OER activity [279]. Utilizing neutral aqueous electrolytes is one of the economical options for achieving high voltage supercapacitors, as it does not corrode the current collectors and the other connections in the system [301]. This is practically seen in many electrochemical supercapacitors wherein neutral aqueous electrolytes are used for achieving high voltage in both symmetric and asymmetric configurations. In an attempt to achieve high voltage symmetric supercapacitors, a light MXene (TiC_2T_x) modified with carbon nanospheres (CNS) was synthesized and investigated as a symmetric supercapacitor in a 1 M Li_2SO_4 aqueous electrolyte [302]. The developed hybrid electrode demonstrated a higher specific capacitance compared to each of the individual materials, which can be attributed to the attachment of CNS to MXene, leading to increased interlayer spacing and high surface area. The fabricated symmetric supercapacitor delivered a voltage of 1.5 V even with an aqueous electrolyte beyond the thermal decomposition potential of water. This higher voltage is due to the usage of neutral electrolytes. Since the Li^+ and SO_4^{2-} ions are strongly solvated in the water molecules, the energy required for the water decomposition is less than solvation energy. This delayed the water decomposition to a higher voltage of 1.5 V and beyond. Such high voltages help to achieve higher capacitance and energy density of 180F/g and 14.1 Wh Kg^{-1}. In another work, a neutral ($Li_2SO_4 + CoSO_4$) and alkaline (KOH) aqueous electrolyte employed to study the relationship between the pH and stable voltage window showed that the former aided in achieving a voltage window twice that of the latter. The 3D $NiCo_2O_4$ nanosheets fabricated on carbon cloth via an electrodeposition process were used for this study. The $NiCo_2O_4$ electrode material could work only in the range of 0 to 0.5 V in alkaline KOH electrolyte, while it worked in the potential range of 0 to 1.2 V in the neutral $Li_2SO_4 + CoSO_4$ electrolyte. This study is another proof of achieving a higher voltage window by restricting H^+ or OH^- ions in the system.

8.4.2. Hydrogel electrolyte for high voltage supercapacitors

With the expanding wearable electronics industry, developing safe, cheap, flexible, and mechanically strong aqueous electrolyte is necessary. Hydrogel electrolyte is a promising one-stop solution that fulfills these needs. Hydrogel electrolyte is composed of a solid non-conductive host polymer matrix with aqueous electrolyte offering dual function as the ionic conductive media transferring ions between the electrodes and working as the separator. The polymer matrix has the capability of allowing fast ion mobility. Therefore, an optimized polymer synthesis facilitates in achieving a solid electrolyte, which can provide high power density similar to a liquid electrolyte. These hydrogel electrolytes can be synthesized separately and then used as the separator cum electrolyte in the supercapacitor or can also be directly synthesized on the electrode surface [303,304]. Commonly used hydrogel host networks are made of synthetic polymers like polyvinyl alcohol (PVA), polyacrylamide (PAM), polymethacrylate (PMA), polyethylene oxide (PEO), etc. or biopolymers like carboxymethyl cellulose (CMC), alginate, hyaluran, etc. The hydrogel electrolytes impede the water electrolysis as there is a strong hydrogen bonding interaction between water molecules and hydrophilic groups of the host polymer matrix. This provides two benefits: preventing leakage issues during packing and reducing the electrochemical activity of water molecules [305].

A PVA-based hydrogel electrolyte synthesized via a physical cross-linking procedure involving a series of freezing and thawing steps exhibited high mechanical strength and elasticity (up to 6 times its original size) [306]. Previously, we have seen the benefits of the neutral Na_2SO_4 electrolyte offering higher voltage even in the case of a symmetric system. Combining these two materials would be advantageous in developing a PVA-Na_2SO_4 hydrogel electrolyte for developing a flexible, high voltage supercapacitor with high power density and cyclability. An activated carbon-based symmetric supercapacitor fabricated using the PVA-Na_2SO_4 hydrogel electrolyte delivered a voltage window of 1.8 V with a maximum energy and power density of 13 Wh Kg^{-1} and 4.2 kW Kg^{-1}, respectively. The reason for this high voltage is attributed to the higher overpotential for H_2 evolution at the negative electrode and also due to the operation of the positive electrode at a potential lower than the theoretical potential of water oxidation. This is reflected by the stability of the symmetric supercapacitor with 96% capacitance retention at 1.8 V for 8000 cycles. Biomass-derived self-doped hierarchical porous carbon has the advantages of offering high porosity with numerous channels for ion transport, large surface area and natural N/O doping, contributing to the high capacitance from combined EDLC and pseudocapacitive charge storage [307]. A self-doped carbon nanofoam (A-CS650) synthesized from cotton stalk through a facile procedure involving hydrothermal followed by pyrolysis demonstrated exceptional performance of very high gravimetric and volumetric capacitances up to 282 F g^{-1} and 234 F cm^{-3} at a current density of 0.5 A g^{-1}. The A-CS650 electrode demonstrated excellent electrochemical performance at a higher scan rate and

extensive mass loading. Here, a symmetric device was fabricated using the unique CMC-Na/Na_2SO_4 gel electrolyte. This enables to obtain a voltage of 1.8 V with an outstanding energy density of 22.6 Wh kg^{-1}.

An alternate approach to achieve high voltage is to employ polyelectrolyte hydrogels [308]. Polyelectrolytes are a class of charged polymers with a lot of positive and negative functional groups providing ion migration channels under an applied electric field to achieve faster and improved ionic conductivity [309,310]. Here, an anionic polymer (CMC) and a cationic monomer (methacrylamidopropyltrimethyl ammonium chloride, MAPTAC) with a neutral Li_2SO_4 electrolyte were used to widen the stable electrochemical window. The commercial activated carbon electrodes were used to fabricate a flexible symmetric supercapacitor with polyelectrolyte hydrogel electrolyte. The assembled device delivers a high operating voltage of 2.1 V owing to the low electrochemical activity for water within the hydrogel. This low electrochemical activity is due to the formation of a molecular cage through interaction between anionic and cationic chains, which locks the water molecules, as shown in Fig. 27 **a**. Also, the hydrogen bonding between water molecules and the $–CONH_2$ in the polymer chain and the electrostatic interaction of charged groups with water molecules restricts water decomposition **(**Fig. 27 **a)**. The assembled device at 2.1 V provided a high specific capacitance of 174.9F/g at a current density of 0.2 A g^{-1} **(**Fig. 27 **b)** and a maximum energy density of 26.5 Wh Kg^{-1}. The hydrogel electrolyte can also be made more porous in order to inhibit water electrolysis. A lignocellulose biomass-based membrane (LC-FD) hydrogel electrolyte synthesized via freeze-drying method displayed a high porosity of 95% and high electrolyte uptake of 1100 wt% [311]. This hydrogel electrolyte developed with Li_2SO_4 salts exhibited a high degree of gelation, high ionic conductivity and exhibited a higher voltage window of 1.8 V for an activated carbon symmetric supercapacitor. The highly uniform porous structure of the hydrogel aids in locking the water molecules inside, thereby inhibiting the electrochemical activity of free water molecules. Also, the LC-FD membrane contains many oxygen functional groups that form hydrogen bonds with free water molecules, thereby further reducing the electrochemical activity. The symmetric device exhibited a specific capacitance of 138.4F/g with 88% capacitance retention even after 10,000 cycles.

8.4.3. Water in salt electrolyte

The "water-in-salt electrolyte" (WiSE), a new type of electrolyte, implies that the electrolyte has a high concentration of ionic salt in solvent (water). The salt concentration is typically near or above the saturation limit. This means that the number of water molecules is smaller than the solute molecule. The WiSE is getting more attention as an electrolyte for an aqueous supercapacitor because of the

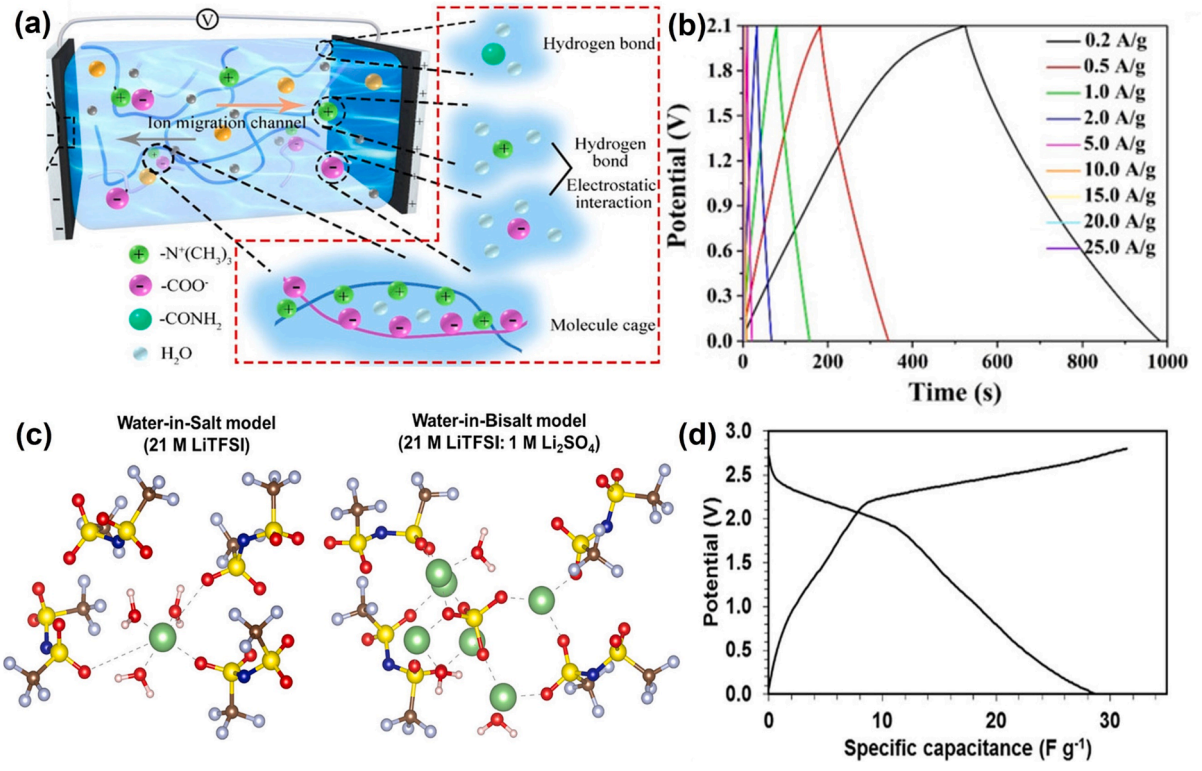

Fig. 27. A) Ion migration in polyelectrolyte hydrogel electrolyte. The figure shows hydrogen bonding, electrostatic interactions, and molecule cage between the functional groups within the polyelectrolyte hydrogel electrolyte (including $-CONH_2$, $-N^+(CH_3)_3$, and $-COO^-$) and the surrounding water molecules. b) GCD curves of the CMC-4 wt% based ASC at current densities from 0.2 to 25A g^{-1}. Reproduced with permission from reference [308] c) Schematic diagram of water-in-salt and water-in-bi salt models (green = lithium, yellow = sulfur, red = oxygen, blue = nitrogen, gray = fluorine, brown = carbon, and pink = oxygen). d) GCD profile of the ASC at a current density of 5 A/g. Reproduced with permission from reference [312]. (For interpretation of the references to colour in this figure legend, the reader is referred to the web version of this article.)

high electrochemical stability window (greater than3 V). It maintains the intrinsic properties of traditional aqueous electrolytes, such as low cost, safety, and good ionic conductivity [313–316]. One of the common salts used in developing the WiSE is lithium bis (trifluoromethanesulfonyl) imide (LiTFSI). This electrolyte provides a wide voltage window due to the formation of a special shell structure in the electrolyte with strong coordination of water molecules with lithium ions [317,318]. A symmetric supercapacitor fabricated with carbon nanorod electrodes using a highly concentrated 21 m LiTFSI electrolyte displayed a wide working voltage of 2.2 V [318]. This high voltage in a symmetric configuration was possible due to the suppression of water splitting caused by a large amount of TFSI anions shielding the water molecules at the electrode/electrolyte interface of the positive electrode. At the same time, an increase in the interaction between water molecules and lithium ions at the negative electrode also aids in restricting the water splitting. Another approach involving the addition of a high concentration of bisalt (21 m LiTFSI + 1 M Li_2SO_4) in water has shown an unprecedented increase in the voltage window, up to 2.8 V [312]. Among all the electrolyte salts used, Li^+ cation with high charge density is one of the preferred choices due to its strong solvation effect. The additional energy required to break this strong ion-water interaction would compete with the energy needed for water decomposition, thus helping to achieve a higher potential or voltage. But, using a high charge density cation with a high charge density anion would lead to strong cation–anion interaction, which would result in lower solubility. This is the reason for preferring a salt with weak cation–anion interaction for developing WiSE as they tend to dissolve better even at higher concentrations.

An ideal choice for WiSE is LiTFSI salt, which has relatively high solubility due to high charge density Li^+ ions and low charge density $LiTFSI^-$ ions. This provides weak anion-cation interaction leading to 21 M electrolyte. But this maximum solubility of 21 m LiTFSI still allows few free water molecules. The addition of a small amount of 1 M Li_2SO_4 with high charge density SO_4^{2-} ions has been shown to lock the remaining free water molecules in their position, further reducing the electrochemical activity of water (Fig. 27 **c**). Though it provides a high stable voltage window, the electrolyte requires electrodes with low OER/HER activity. The asymmetric supercapacitor developed with Li^+ inserted MnO_2 and carbon with this water in bi-salt electrolyte worked at 2.8 V (Fig. 27 **d**), delivering an energy density of 55.7 Wh kg^{-1} at a power density of 1 kW kg^{-1}.

The 17 m sodium perchlorate ($NaClO_4$) salt with low viscosity and high conductivity is an alternative to imide-based salts from an economic point of view to obtain a high voltage supercapacitor [319–321]. Depending on the H-bonding interactions with electrolyte ions, this WISE-based supercapacitor is expected to deliver voltage beyond the range of 2.0 V. In a recent research with WISE, a highly porous activated carbon electrode derived from ground grain hulls provided a very high specific surface area of 1037.6 m^2/g and a specific capacitance of 313.3F/g at a current density of 0.5 A g^{-1} is used [322]. The carbon electrodes assembled into a symmetric supercapacitor using 17 m $NaClO_4$ electrolyte delivered a high voltage of 2.4 V with a high energy density of 47.2 Wh $kg^{-1,}$ which is higher than in the 1 M Na_2SO_4 electrolyte for the same symmetric system. The higher voltage delivered by the $NaClO_4$ electrolyte is due to the decrease in the electrochemical activity of water caused by high salt aggregation, triggering the water molecules to coordinate with Na^+ ions. In another approach, different concentrations of sodium-based salts like CH_3COONa, $NaNO_3$ and $NaClO_4$ are used to determine the optimum WiSE salt concentration for obtaining high voltage and energy density [323]. A symmetric supercapacitor fabricated with N doped rGO was employed in this study. A high voltage of 2.7 V was delivered by the symmetric supercapacitor. The reason behind higher voltage is that the ClO_4^- ions exhibit more chaotropicity, i.e., water breaker. In another instance, to replace imide-based salts, high concentration potassium acetate (CH_3COOK) WiSE salt is used as an economical alternative to obtain a high voltage supercapacitor [324]. An *in situ* free radical polymerization approach was followed to develop PAAK/CMC-CH_3COOK polyelectrolyte hydrogel. The potassium ion in the PAAK chain and the CH_3COOK form a solvent-sheath structure with free water molecules and inhibit water hydrolysis. A symmetric supercapacitor fabricated with N-doped graphene hydrogel electrodes delivered a voltage window of 2.1 V with an energy density of 33.0 W h kg^{-1}. Besides the high voltage, the supercapacitor displayed excellent temperature stability in the range of − 20 to 70 °C. This shows the practicality of the WiSE-based supercapacitors for a wide temperature range.

8.5. Non-aqueous electrolyte systems

The two different non-aqueous electrolytes commonly used in supercapacitors are organic and ionic liquid electrolytes. These electrolytes offer very high voltage windows in the range of 3 to 4.5 V with any electrode materials. Such high voltage is vital in achieving higher energy density, which is difficult to achieve with aqueous electrolyte.

8.5.1. Organic electrolyte:

Organic electrolytes are prepared by dissolving conducting salts in organic solvents. Organic solvents offer the advantage of achieving higher voltage and, thus, higher energy density in supercapacitors, which is on par with lithium-ion batteries [325]. However, they have a lot of other drawbacks, such as higher cost, lower conductivity, volatility, flammability, and toxicity [168]. The larger molecular size of organic electrolytes also necessitates the pore size tuning in electrodes. This will help in overcoming the slower rate in supercapacitors. The safety issues associated with organic electrolytes necessitate the supercapacitor assembly to be done in a very controlled environment, or else it could lead to severe degradation in their performance. Typically, organic electrolytes are widely used in commercial supercapacitors along with carbon-based electrodes. In recent times, their compatibility or best performance output has been optimized and achieved with redox and hybrid electrode materials [274,326].

The organic solvent forms an integral part of the organic electrolyte and holds a pivotal role in achieving exceptional performance. A prime organic solvent should ideally meet several criteria, including efficient solvation of the conducting salt, a higher electrochemical voltage window, low viscosity across operational temperatures, and excellent safety features (such as non-flammability and non-toxicity). Comment solvents used in organic electrolytes are acetonitrile (ACN), propylene carbonate (PC), N,N-Dimethylformamide (DMF) and N-Methylpyrrolidinone (NMP), etc. [326–328]. Among these solvents, ACN displays superior

characteristics like lower viscosity, higher dielectric constant, and a lower melting point than PC. Consequently, ACN-based electrolytes typically exhibit higher conductivity than PC-based ones, leading to lower Equivalent Series Resistance (ESR) and enhanced power performance even at lower temperatures. However, ACN comes with significant drawbacks, notably its low flash point and toxicity. PC, being less toxic and possessing a higher flash point than ACN, has garnered increasing interest as a substitute in PC-based electrolytes. Yet, due to PC's lower conductivity compared to ACN, EDLCs based on PC tend to exhibit lower power density and energy efficiency. This limitation is more pronounced at low temperatures due to PC's high viscosity Furthermore, the operational cell voltages for both ACN- and PC-based EDLCs remain confined to 2.5–2.8 V. Enhancing energy densities by elevating working voltages has been a sought-after goal. Consequently, substantial efforts over the past decade have been focused on developing alternative organic electrolytes to create high-performing EDLCs [329–331].

An organic solvent, when combined with a conducting salt to create an organic electrolyte, assumes a pivotal role in achieving heightened performance. The ion concentration and mobility are pivotal in dictating electrolyte ionic conductivity. Conducting salts significantly impact the Electrical Potential Stability Window (ESPW), thermal stability of organic electrolytes, and specific capacitance. When selecting or developing suitable salts for specific solvents, factors like solubility, conductivity, stability, safety, and cost demand consideration. Tetraethylammonium tetrafluoroborate ($TEABF_4$), renowned for its favorable attributes, is the most prevalent salt in commercial supercapacitors [332,333]. While $TEABF_4$ dominates, other salts are under scrutiny for augmenting electrolyte properties, including solubility, conductivity, stability, and temperature performance. The other common conducting salts used are lithium hexafluorophosphate ($LiPF_6$), lithium perchlorate ($LiClO_4$), and lithium bis(trifluoromethanesulfonyl)imide (LiTFSI), etc. [334–336].

Solubility stands as a significant factor, impacting both ionic conductivity and the maximum energy density of associated supercapacitors. Optimal ion concentration values exist for maximizing electrolyte ionic conductivity, with ACN displaying a solubility limit of 1 M for $TEABF_4$, while other salts showcase higher solubility above 2 M [337]. Operating supercapacitors within a broad temperature range necessitates assessing salt solubility at lower temperatures due to its relevance. Electrolyte conductivity hinges on multiple factors: salt concentration, ion dissociation, ion mobility, solvent type, and temperature. Aqueous electrolytes tend to display high dissociation degrees compared to organic ones, consequently leading to lower ionic conductivity and higher equivalent series resistance (ESR) in organic electrolytes. The choice of cations and anions in organic salts further impacts dissociation degrees and ion mobility, consequently influencing electrolyte conductivity. For example, research by Ue et al. [338] revealed that the conductivity of common salts varies based on cations and anions. Conducting salt choice profoundly influences the electrochemical stable potential window (ESPW) of organic electrolytes. The ESPW hierarchy for different cations and anions was found to impact electrode materials. This factor is crucial for achieving optimal energy storage performance. Matching the ion size with the pore size of carbon-based electrode materials is vital and this necessitates considering ion solvation shell adjustments when pore size aligns with bare ion size. Matching impacts the capacitance and power performance of EDLC charge storage mechanism. The type of anion also strongly influences capacitance. For instance, PF_6^- was identified as the most stable anion among the options studied, contributing to substantial capacitance. Moreover, the valence state of ions also affects EDLC capacitance and energy density. In summary, the interplay between organic solvents and conducting salts in organic electrolytes is a multifaceted process that intricately influences the supercapacitor performance.

To enhance the solubility of salts in organic solvents, particularly propylene carbonate (PC), researchers have investigated asymmetric tetraalkylammonium salts and cyclic quaternary ammonium salts. For instance, compounds like Triethyl methyl ammonium tetrafluoroborate ($TEMABF_4$), 1-ethyl-1-methylpyrrolidinium ($MEPYBF_4$), and tetramethylenepyrrolidinium ($TMPYBF_4$) exhibit significantly higher solubilities in PC compared to $TEABF_4$ [339]. However, since salts contribute considerably to the overall electrolyte cost, achieving a balance between performance and cost (i.e., salt concentration) is crucial. A case in point is the spiro-type quaternary ammonium salt, spiro-(1,1′)-bipyrrolidinium tetrafluoroborate ($SBPBF_4$) [340,341], which has gained attention for its smaller cation size, enhanced mobility, and greater solubility compared to the common $TEABF_4$. Nonetheless, the higher cost of $SBPBF_4$ relative to $TEABF_4$ might limit its widespread utilization. Additionally, Kurig et al. [342] explored substituted phosphonium cation-based electrolytes for EDLCs utilizing titanium carbide derived carbon (C(TiC)) electrodes. An EDLC employing a 1 M tetrakis (diethylamino)-phosphonium hexafluorophosphate ($TDENPPF_6$)/ACN electrolyte exhibited excellent performance up to 3.2 V. The EDLC displayed a gravimetric capacitance of 85F/g, a characteristic relaxation time of 0.9 s, and a gravimetric energy density of 27 Wh kg^{-1} at 3.2 V cell voltage. Remarkably, no significant loss in discharging capacitance was observed after 10,000 charge–discharge cycles. However, these substituted phosphonium cation-based electrolytes demonstrated lower conductivities compared to $TEABF_4$/ACN and $TEMABF_4$/ACN, which could potentially impact supercapacitor's ESR, rate performance, or thermal stability.

Regarding anions, it's noted that commonly used fluoro-complex salts containing halogens, like BF_4, may undergo hydrolysis to generate hazardous hydrogen fluoride (HF). To address this concern, researchers explored salts based on bis(oxalato)borates (BOB anion) such as TMABOB, ETMABOB, TEMABOB, and TEABOB [343,344]. Transitioning from bis(oxalato)borate anions to asymmetric difluoro(oxalato)borate anions was found to heighten salt solubility, offering a potential solution to this issue [345,346]. Notably, in addition to organic cations, salts based on inorganic cations like Li^+, Na^+, and Mg^{2+} have garnered attention [347–349]. In summary, research has explored various avenues to improve salt solubility in organic solvents, striking a balance between performance and cost. The choice of cations and anions significantly impacts solubility and performance, with ongoing exploration of diverse options in the pursuit of advancing energy storage technology.

Organic electrolytes have been utilized in pseudocapacitors employing materials with pseudocapacitive behavior, including metal oxides, composite materials, and conductive polymers. These electrolytes often incorporate Li ions due to their small size, which facilitates ion intercalation and de-intercalation. Commonly employed salts in organic electrolytes include $LiPF_6$ and $LiClO_4$. Among the frequently used solvents are acetonitrile, propylene carbonate, and various mixtures like ethylene carbonate–ethyl methyl

carbonate, ethylene carbonate–diethyl carbonate, ethylene carbonate–dimethyl carbonate, ethylene carbonate–dimethyl carbonate–ethyl methyl carbonate, and ethylene carbonate–dimethyl carbonate–diethyl carbonate [274]. Additionally, the application of organic electrolytes in asymmetric electrochemical supercapacitors has gained significant interest, offering further improvements in energy density. For instance, various organic electrolytes utilized in asymmetric electrochemical supercapacitors are reported, such as carbon//TiO_2 (1 M $LiPF_6$/EC–DMC), graphite//AC (1.5 M $TEMABF_4$/PC), carbon//V_2O_5 (1 M LiTFSI/ACN), carbon//ECP (1 M $TEABF_4$/PC), and carbon//$Li_4Ti_5O_{12}$ (1 M $LiPF_6$/EC–EMC). [64] These organic electrolytes exhibit enhanced energy density due to their wider voltage window (3–4 V) compared to aqueous-based asymmetric supercapacitors.

To address the limited operating voltage range of aqueous gel polymer electrolytes, organic counterparts have been employed, allowing for higher cell voltages of 2.5–3 V. This is achieved through physical blending of high molecular weight polymers like Polyvinylidene fluoride-co-hexafluoropropene (PVDF-HFP) or Polymethyl methacrylate (PMMA) with conducting salts and nonaqueous solvents such as dimethyl formamide (DMF), propylene carbonate (PC), and ethylene carbonate (EC). Lee et al. [350] developed a high-performance, thin, planar supercapacitor with dynamic stretchability. A buckled manganese/molybdenum (Mn/Mo) mixed oxide@multiwalled carbon nanotube (MWCNT) electrode is deposited on a prestrained elastomer film substrate. An organic gel polymer electrolyte composed of adiponitrile/succinonitrile/lithium bis(trifluoromethanesulfonyl)imide/poly(methyl methacrylate) (ADN/SN/LiTFSI/PMMA) is used. This results in a 2 V operation cell voltage, enhanced stability, and notable performance metrics, including an areal capacitance of 7.5 mF cm^{-2}, areal energy density of 4.2 μWh cm^{-2}, and power density of 1.0 mW cm^{-2}. The supercapacitor remains stable under both static and dynamic stretching deformation. Huang et al. [351] developed an organic gel electrolyte by utilizing a blend of PEO–PAN (PAN-b-PEG-b-PAN) as the host, DMF as the plasticizer, and $LiClO_4$ as the electrolytic salt for an activated carbon-based supercapacitor. This organic gel electrolyte exhibited an impressive ionic conductivity of 6.9 mS cm^{-1} and showed excellent compatibility with carbon electrodes. The resulting supercapacitor achieved a capacitance of 101F/g at 0.125 A g^{-1} and delivered an energy of 11.5 Wh kg^{-1} at a high power of 10 kW kg^{-1}, all within a voltage window of 2.1 V. Remarkably, the supercapacitor demonstrated remarkable stability, with minimal capacitance degradation observed over an extensive 30,000 cycle lifespan. The choice of electrolyte salt and the ratio of salt to host polymer significantly influenced the ionic conductivity of the organic gel electrolyte.

8.5.2. Ionic liquid electrolytes:

The utilization of ionic liquid (IL) electrolytes as an alternative to organic electrolytes offers multiple advantages [352]. It enhances ion mobility and eliminates the safety concerns associated with organic electrolytes. A noteworthy observation is the prevalence of robust electrostatic forces among their molecular ions, contributing to reduced volatility and flammability and elevated levels of chemical and electrochemical stability. Additionally, owing to their elevated thermal stability, ILs often exhibit negligible vapor pressure at typical temperatures. Consequently, they have gained traction as solvents or electrolytes in the realm of energy storage applications. These inherent qualities, coupled with commendable intrinsic ionic conductivity, position ILs as desirable candidates for solvents and electrolytes in the context of supercapacitors. Previous findings have indicated that utilizing ILs as electrolytes in supercapacitors exhibits enhanced capacitance retention and operational safety at elevated temperatures, outperforming those employing non-aqueous electrolytes. Furthermore, it has been noted that supercapacitors constructed with the incorporation of ILs can operate at elevated cell voltages. This advancement contributes significantly to enhancing the energy density, aligning them more closely with the energy storage capabilities traditionally associated with secondary batteries. ILs comprise organic cations like imidazolium (Im), pyridinium (PY), pyrrolidinium (PYR), ammonium, phosphonium, and sulfonium [353–356]. These cations are paired with inorganic or organic anions such as PF_6^-, BF_4^-, triflate ($CF_3SO_3^-$), and bis (trifluoromethanesulfonyl imide) (TFSI) ($(CF_3SO_2)_2N^-$) [357,358]. The diverse combinations of cations and anions open a plethora of opportunities to tailor ionic liquids with specific properties suitable for desired applications.

Ionic liquids (ILs) can be categorized into two groups: protic ILs (PILs) and aprotic ILs (AILs) [359–361]. PILs consist of equimolar Bronsted acids and bases, enabling proton exchange between them, leading to the formation of proton donor and acceptor regions. This phenomenon can facilitate the establishment of hydrogen bonds. Notably, PILs are easier to formulate, more cost-effective, less viscous, and exhibit higher conductivities compared to AILs. A phosphonium-based PIL, $[Bu_3HP][BF_4]$, as the electrolyte for carbon-based supercapacitors (carbon-SCs) is explored [362]. The $[Bu_3HP][BF_4]$ PIL mixed with acetonitrile demonstrates high capacitance on activated carbon in a two-electrode cell configuration operating up to 1.5 V. This favorable capacitance is maintained over a wide range of operating temperatures and remains stable even after 1000 charge–discharge cycles. Considering its physicochemical attributes, along with its consistent electrochemical performance and stability, the $[Bu_3HP][BF_4]$ PIL blended with acetonitrile holds potential as a promising electrolyte for supercapacitor applications. Supercapacitor built utilizing nanostructured carbon electrodes and solvent-free IL, $1Me_3BuImBF_4$, as electrolytes, achieving an exceptional specific capacitance of 111F/g at ambient temperature [363]. It also exhibited a key attribute of a nominal voltage of 3.0 V and a maximum cell voltage of 3.5 V. Another work where researchers investigated three different PILs: triethylammonium bis (tetrafluoromethylsulfonyl) imide ($Et_3NHTFSI$), trimethylammonium bis (tetrafluoromethylsulfonyl)imide ($Me_3NHTFSI$) and pyrrolidinium nitrate ($PYRNO_3$) [364]. The study's outcomes reveal that PIL-based supercapacitors can demonstrate remarkable cycling stability, endure over 30,000 cycles, and perform effectively across a wide temperature range. The mixture of Propylene Carbonate-$Me_3NHTFSI$ exhibits suitability even at –20 °C, while the solvent-free supercapacitor utilizing PIL $Et_3NHTFSI$ maintains stability from 10 °C to 60 °C. Additionally, the investigation highlights that PILs with minimal water content combined with AC containing fewer surface groups eliminate noticeable pseudo-capacitive behavior. Despite their stability, PIL and activated carbon-based supercapacitors exhibit lower operational voltages compared to traditional organic solvents, consequently yielding lower energy outputs than those achievable with organic electrolytes or aprotic ILs.

Another work involved assembling Et_4NBF_4 IL electrolyte-soaked separator between montmorillonite *K*10 clay-MWCNT-MnO_2

composite electrodes [365]. This device delivered a voltage of 2.7 V, resulting in energy and power densities of 171 Wh Kg^{-1} and 96.4 kW Kg^{-1}, respectively. The exceptional performance of the EDLCs could be attributed to the interaction between *K*10 and the tetraethylammonium cation [$(C_2H_5)_4N^+$ or TEA^+] in the ionic liquid electrolyte, possibly involving acid-base interactions with *K*10′s surface hydroxyl groups. These EDLCs maintained their remarkable characteristics even at a high-power density of 96.4 kW Kg^{-1}, showcasing an impressive energy density of 91.1 Wh Kg^{-1} and demonstrating outstanding rate capability. Reduced graphene oxide (RGO) synthesized using HBr as a reducing agent was also tested with IL by researchers [366]. Supercapacitors based on RGO were constructed in two-electrode configurations using IL electrolytes: 1-butyl-3-methylimidazolium hexafluorophosphate ($BMIPF_6$) and 1-butyl-3-methylimidazolium tetrafluoroborate ($BMIBF_4$). RGO in $BMIBF_4$ exhibited a higher capacitance of 74F/g, while RGO in $BMIPF_6$ showed 45F/g. However, due to the wider potential window (4 V) of $BMIPF_6$, RGO in $BMIPF_6$ demonstrated superior energy and power densities. Notably, the maximum power density reached 27.8 kW Kg^{-1}, and the highest energy density achieved was 18.9 Wh Kg^{-1}. These findings suggest promising applications for RGO in $BMIPF_6$ based supercapacitors.

A study involving graphene nanosheets to enhance supercapacitor behavior in a butylmethylpyrrolidinium–dicyanamide ($PYR_{14}DCA$) IL electrolyte was conducted [367]. The electrode exhibited a high capacitance of 330F/g with a wide potential window of 3.3 V. At 60 °C, a symmetric-electrode supercapacitor using this IL electrolyte achieves impressive energy and power densities. The maximum values achieved are 140 Wh Kg^{-1} for energy density and 52.5 kW Kg^{-1} for power density. These figures significantly surpass the results obtained with a conventional organic electrolyte, which recorded energy and power densities of 20 Wh Kg^{-1} and 17.8 kW Kg^{-1}, respectively, in a control cell. The IL electrolyte 1-butyl-1-methylpyrrolidinium dicyanamide, [BMP][DCA], when used with nitrogen-doped reduced graphene oxide (N-rGO) aerogel electrodes [368], exhibited a wide potential window of 4.0 V and notable specific capacitance of 764.53F/g at 1 A g^{-1}, exemplifying the potential of IL electrolytes to enhance supercapacitor performance. The device also exhibited a maximum specific energy of 245 Wh Kg^{-1} with a capacitance retention of 86% after 3000 cycles.

Deng et al. [369] introduced a novel electrode configuration comprising MnO_2 nanowires on Ni foam, coupled with a lithium-ion quasi-ionic liquid ($LiClO_4$/2-oxazolidinone (OZO) salts) electrolyte for pseudocapacitors. Operating over a broad potential range (2.5 V), this setup exhibited an impressive energy density of 304 Wh Kg^{-1}. A new approach of redox-active ILs for SC applications [370], involved combining the IL with ferrocene as an electroactive material to enhance energy density, resulted in a wide working potential (around 2.5 V) and a high concentration of redox moieties (2.5 M) in the electrolyte. Another approach employing a eutectic mixture of ILs, namely $Pip_{13}FSI$ and $PYR_{14}FSI$, as an electrolyte paired with exfoliated graphite oxide electrodes, resulting in a capacitance of 180F/g within a voltage window of 3.5 V at 20 mV s^{-1} and a wide temperature range from − 50 °C to 80 °C [371]. All these diverse ILs exhibit unique behaviors that make them promising candidates for electrochemical SC devices. While the development of ILs in SC applications shows promise, it also poses several challenges that warrant further exploration and research.

8.5.3. Ionic Liquid Based Polymer Electrolytes.

The utilization of liquid electrolytes, including ILs, for supercapacitors has been advantageous, yet their requirement for encapsulation hinders their implementation in flexible and printed electronics. To address this limitation, IL-based Gel polymer electrolytes (GPEs) offer a promising solution by combining the benefits of ILs with the mechanical reliability of polymers, paving the way for flexible energy storage devices. Traditional polymers such as polyethylene oxide (PEO), polyvinylidene fluoride (PVDF), and polyvinylidene fluoride-co-hexafluoropropylene (PVDF-HFP) have been extensively explored as polymeric host materials for ionogel electrolytes in energy storage applications [372,373]. IL-incorporated polymers essentially form polyelectrolytes, integrating electrolyte functionalities (cations/anions) into their chemical structure. This incorporation imparts improved mechanical stability to the GPE, making it suitable for flexible applications. However, GPE systems involving liquid electrolytes with organic solvents exhibit inferior electrochemical stability due to the flammable nature of these solvents, leading to a narrower potential window and lower thermal stability.

Of the various polymers suitable for constructing ionogel electrolytes in supercapacitors, PVDF-HFP stands out due to its low glass transition temperature and robust mechanical properties. The impact of incorporating $LiPF_6$ into an IL based gel electrolyte (EMIm-FAP) has been studied for supercapacitor performance [374]. The resulting $LiPF_6$/IL/PVDF-HFP gel electrolyte film demonstrates a wide electrochemical window (−2.0 to 2.0 V), high ionic conductivity (~2.6×10^{-3} S cm^{-1} at 20 °C), and good thermal stability. Electrodes treated with acid-treated MWCNTs exhibit a specific capacitance of ~127F/g using the IL/$LiPF_6$-containing gel polymer electrolyte, whereas the same electrodes with the gel polymer electrolyte lacking Li-salt exhibit a specific capacitance of ~76F/g. Another group of researchers developed a 3 V stretchable supercapacitor using a nonvolatile gel electrolyte [375]. It featured a CNT electrode, Au/Ti current collector, EMIM-TFSI/PVDF-HFP gel electrolyte, and PDMS substrate. This supercapacitor maintained high capacitance (96.6%) through 3000 stretch cycles at 20% strain. Surface microroughness from office paper was transferred to enhance adhesion between layers. This cost-effective, and scalable innovation improved interfacial strength, ensuring durable ion-gel-based supercapacitors without delamination. This novel approach offers insights into devising devices using compliant materials, contributing to technological advancement.

More recently, an ionogel electrolyte based on a graft copolymer (PEGBEM-g-PAEMA) was developed [376]. Supercapacitors were produced using porous carbon electrodes and a PEGBEM-g-PAEMA/$EMIMBF_4$ electrolyte. These capacitors demonstrated a capacitance of 55.5F/g, a power density of 900 W Kg^{-1}, and an energy density of 25 Wh Kg^{-1} at 1.0 A g^{-1}. Remarkably, these capacitors retained good performance even when bent at various angles, without the need for specific encapsulation. A high-performance all-solid-state supercapacitor is successfully developed, employing a [BMIM][BF_4] functionalized graphene (f-graphene) electrode and [EMIM][BF_4]:PVDF-HFP gel polymer electrolyte [377]. The superior performance is attributed to enhanced wettability of graphene achieved through [BMIM][BF_4] functionalization. The charged f-graphene surface promotes rapid ion diffusion across the f-graphene/gel polymer electrolyte interface, maximizing material utilization. Moreover, the [EMIM][BF_4]/PVDF-HFP gel polymer electrolyte

ensures stability in a wide operating potential range (4 V) and a temperature range of −10 to 80 °C. Notably, the supercapacitor achieves an impressive energy density of 92 Wh Kg^{-1} and power density of 33 kW Kg^{-1} at 0.5 A g^{-1}, maintaining 57% energy density even at a high current density of 6 A g^{-1}. The f-graphene supercapacitor exhibits excellent cycling stability, retaining over 90% capacity after 12,000 cycles.

More recently, an all-solid-state asymmetric flexible supercapacitor (AFSC) with a maximum operating voltage of 3.5 V has been successfully developed [378]. This is achieved by utilizing an electrolyte composed of an ionic liquid (IL) incorporated gel-polymer (EMIMTFSI/PVDF-HFP). The optimized AFSC configuration comprises MnO_x@TiN nanowires@carbon nanotube (NWs@CNT) fiber as the positive electrode and C@TiN NWs@CNT fiber as the negative electrode. This configuration led to an exceptionally high stack volumetric energy density of 61.2 mWh cm^{-3}, comparable to commercially available planar lead-acid batteries (50 to 90 mWh cm^{-3}). Additionally, the AFSC maintains excellent flexibility, with 92.7% retention after 1000 bending cycles at 90°. The utilization of ionogel IL-based electrolytes holds promise for creating high-performance, flexible AFSCs suitable for future portable and wearable electronic devices. The choice of polymer matrix significantly influences the performance of ionogel electrolytes in supercapacitor applications, and ongoing research is exploring new polymers and their interactions with ILs to enhance energy storage devices further. Other polymer electrolytes like N-butyl-N-methyl pyrrolidinium bis(trifluoromethylsulfonyl) imide), Im14BF_4-incorporated PVDF-co-HFP GPEs, and 1-ethyl-3-methylimidazolium tetracyanoborate (Im13TCB)-incorporated PVDF-co-HFP polymer GPEs have shown success in SC applications [379]. Overall, the utilization of ILs in various polymer-based electrolytes holds promise for efficient energy storage in SCs. However, further research is needed to fully harness their benefits and address any challenges in SC applications.

8.5.4. Solid state electrolyte

Inorganic solid-state electrolytes have garnered significant attention in energy storage, particularly in supercapacitors, due to their potential to overcome limitations associated with traditional liquid electrolytes [380,381]. In conventional supercapacitors, liquid electrolytes are commonly used. However, these liquid electrolytes have drawbacks such as potential leakage, flammability, limited operating temperature range, and issues related to device miniaturization. Inorganic solid-state electrolytes offer a promising alternative, providing numerous advantages that can address these limitations. They offer safety and stability; unlike liquid electrolytes, inorganic solid-state electrolytes are non-flammable and non-volatile, enhancing the safety and stability of supercapacitor devices [382]. They are less prone to leakage and can withstand mechanical stress and vibrations [383]. Inorganic solid-state electrolytes can operate over a broader temperature range compared to liquid electrolytes, making them suitable for applications in extreme environmental conditions, such as automotive and aerospace systems [384]. These electrolytes offer high electrochemical stability, enabling the use of a wider range of electrode materials, including those with high redox potential. This flexibility allows for the design of high-energy–density supercapacitors. Solid-state electrolytes enable the miniaturization of supercapacitor devices and their integration into various compact electronics and wearable devices, where space and safety are critical considerations.

Despite their advantages, inorganic solid-state electrolytes have received less attention compared to polymer electrolytes due to their lack of flexibility. However, researchers have made significant progress in this area. Francisco et al. developed a Li_2S-P_2S_5 solid-state inorganic electrolyte with high Li-ion conductivity, acting as both separator and ion conductor [385]. The solid-state electrolyte (SSE) was produced through planetary ball milling using Li_2S and P_2S_5 in an 80–20 mol.% ratio. After the ball milling process, the resulting mixture was heat-treated to create a semi-crystalline powder consisting of particles ranging in size from approximately 1 to 5 μm. The selection of the Li_2S-P_2S_5 material system was based on its high lithium-ion conductivity, which exceeds 1×10^{-3} S/cm. Ulihin et al. reported a composite solid electrolyte (0.4$LiClO_4$-0.6Al_2O_3) used in supercapacitors, showing a specific capacitance of 29F/g at high temperature [386]. The composite solid electrolyte was prepared through the sintering of pre-dehydrated components at 300 °C. Liao et al. explored lithium aluminum titanium phosphate (LATP), known for its NASICON-type structure ($Na_{1+x}Zr_2Si_xP_{3-x}O_{12}$, $0 < x < 3$) [387]. LATP is a lithium ionic conductor with high ionic conductivity at room temperature and remarkable electrochemical stability, making it a promising candidate for solid electrolytes in all-solid-state supercapacitors. However, pure ionic conductors like LATP do not allow stoichiometry changes under the working potential necessary for energy storage. To address this limitation, heterophase contacts are crucial, enabling compositional changes. Carbon nanotubes (CNTs), known for their excellent electrical conductivity, have been mixed with LATP in this work. These LATP/CNT mixtures have been utilized in all-solid-state supercapacitors, adopting a sandwich structure - two layers of the mixture separated by a pure LATP layer acting as a separator. The study's findings provide clear evidence that electrical double layers can be established at the heterophase contacts, demonstrating the supercapacitor behavior of the device, particularly with higher CNT contents. The capacitance of specimens without CNTs is limited to 0.52 mF/cm^3. However, this value significantly increases to 11.59 mF/cm^3 when the CNT content is raised to 7.5%.

Another research direction to synthesize a single phase LATP, $Li_{1.3}Al_{0.3}Ti_{1.7}P_3O_{12}$ as a solid electrolyte was a one-step solid-state reaction using ammonium polyphosphate (APP) as a PO_4 precursor [388]. To enhance densification, sintering aids such as $LiMnPO_4$ (LMP) were introduced. Porous/dense/porous layered ceramics were manufactured by sintering a pellet composed of LATP/LATP-2% LMP/LATP at 825 °C. These carbon-filled layered ceramics exhibited a significant capacitance of 0.13F/cm at a low scan rate of 2 mV/s. The high capacitance in carbon-filled layered ceramics was attributed to the increased contact area between the electrode and solid electrolyte within the porous structure. Additionally, the resulting supercapacitor demonstrated excellent cycling stability, retaining approximately 91% of its initial capacitance after 600 cycles at a scan rate of 5 mV/s. These advancements represent significant progress in the development of inorganic solid-state electrolytes for supercapacitors.

Ceramic ionic conductors are known for their limited ionic conductivity, which isn't ideal for practical applications. However, when these ceramics are combined with a small amount of ionic liquid (IL), their ionic conductivity experiences a significant boost. An investigation was done by Dalvi et al. on the use of IL-ceramic composites with IL content up to 13 wt% for capacitor applications [389]. Supercapacitors are designed using these IL-dispersed, Li^+ ion-conducting fast ionic ceramics, such as $LiTi_2(PO_4)_3$ (LTP) and

$Li_{1.3}Al_{0.3}Ti_{1.7}(PO_4)_3$ (LATP). The cells are assembled in 2032-coin cells, with these composites and activated charcoal coated on copper foil serving as the electrodes. The developed supercapacitor containing LATP with 13 wt% EMIM BF_4 as the electrolyte, operated at around 35 °C, demonstrates a high specific capacitance of approximately 181F/g, specific energy of about 6.1 Wh/kg, and a power output of about 140 W/kg at 0.65 mA/cm^2 (0.56 A/g) and 1 V. Another significant advancement made in LATP is by incorporating various solid polymer electrolytes such as PEO, PEG [390]. These electrolytes demonstrate impressive ionic conductivity (approximately 10^{-4} Ω^{-1} cm^{-1} at 40 °C). Supercapacitors constructed with these electrolyte membranes and AC electrodes operate effectively within a voltage range of 0 to 2 V at 1 mA (1.43 A/g). These supercapacitors exhibit a high specific capacitance (~100F/g) along with specific energy (~14 Wh/kg), specific power (~682 W/kg), and exceptional stability lasting up to ~2500 charge–discharge cycles.

Perovskite solid electrolytes, specifically lithium lanthanum titanate, $Li_{3x}La_{2/3-x}\square_{1/3-2x}TiO_3$ (LLTO, □ represents vacancy), have garnered significant interest among various solid-state electrolytes for energy storage devices. This attention is due to their impressive properties, including high lithium-ion conductivity in bulk (approximately 10^{-3} S/cm) at room temperature and exceptional chemical stability even when exposed to air [391,392]. Researchers prepared LLTO electrolytes via a conventional solid-state reaction approach and tested them using an Au|LLTO|Au cell configuration [393]. The results demonstrate that $Li_{0.33}La_{0.56}TiO_3$ exhibits the highest capacitance, reaching 0.28 mF/g among the samples prepared. Furthermore, it shows an excellent cycling performance under a potential range of 2 V at 300 K. Another study was focused on improving the ionic conductivity issue in lithium lanthanum titanate (LLT) caused by its weak grain boundary conductivity [394]. Enhancing LLT's electric performance involves doping cations with larger radii. In this context, a series of $Li_{0.33}La_{0.56}\square_{0.11}Ti_{1-x}Sn_xO_3$ (LLTS, □ representing a vacancy) compounds with varying Sn^{4+} concentrations (x = 0–5 mol%) was synthesized. The LLTS ceramic with 0.1 mol% Sn^{4+} showed the highest ionic conductivity, but higher Sn^{4+} concentrations reduced bulk pellet conductivity, revealing crucial factors affecting intrinsic capacitances in these perovskite compounds for all-solid-state supercapacitors (ASSS).

A summary of various electrolyte systems impacting the performance of some asymmetric supercapacitors is given in Table 2.

9. Enhancement of voltage window in supercapacitors

For an aqueous supercapacitor, the voltage window is determined with the help of electrochemical characterization tools like cyclic voltammetry, galvanic charge–discharge test, etc. [399,400]. A fabricated device undergoing a cyclic charge–discharge may operate normally within a prescribed potential window (obtained from a potential range evaluation of the electrodes). Once the maximum voltage window is achieved, any further increase in the voltage window is marked by the loss of coulombic efficiency, low cycling stability and low reversibility of curves. So far, there are no specific standards to restrict the exact voltage window. Yu et al. have performed an exhaustive study on the voltage window of the aqueous electrolyte [401]. As per their recommendation, a suitable operational voltage window of a supercapacitor should ensure a high coulombic efficiency (>95%), good reversibility and at least 90%

Table 2
The electrochemical performance of selected asymmetric supercapacitors based on different electrolyte systems.

Electrolyte Type	Supercapacitor Device Config.	Electrolyte used	Capacitance (F/g)	Total Voltage window (V)	Specific energy (Wh/Kg)	Ref.
Hydrogel electrolyte	AC // AC	PVA-Na_2SO_4	142	1.8	13	[395]
Hydrogel electrolyte	Carbon nanofoam // Carbon nanofoam	CMC-Na/Na_2SO_4	282	1.8	22.6	[307]
Hydrogel electrolyte	AC // AC	Li_2SO_4 polyelectrolyte	174.9	2.1	26.5	[308]
Hydrogel electrolyte	AC // AC	LC-FD- Li_2SO_4	138.4	1.8	16.1	[396]
Water in salt electrolyte	PANI − N // PANI − N	21 m LiTFSI electrolyte	44	2.2	29.6	[318]
Water in salt electrolyte	$LiMnO_2$//AC	21 m LiTFSI:1M Li_2SO_4	71.1	2.8	55.7	[312]
Water in salt electrolyte	AC // AC	17 m $NaClO_4$	59	2.4	47.2	[397]
Water in salt electrolyte	NG // NG	24 M CH_3COOK	55	2.1	33	[398]
Organic electrolyte	N – AC // N – AC	1 M TEMABF_4 / propylene carbonate	40	2.5	37	[331]
Organic electrolyte	AC // AC	DES 1: 4 + 20% wt. AN	15	3.4	–	[331]
Organic electrolyte	AC // AC	SBP-BF4/PC	120	2.7	31	[340]
Organic electrolyte	C - TiC // C - TiC	1 M TDENPPF_6 / ACN	85	3.2	27	[342]
Organic electrolyte	AC // AC	1.6 M TEAODFB / PC	21.4	2.5	28	[345]
Organic electrolyte	AC // AC	PEO–PAN	101	2.1	11.5	[351]
Ionic liquid electrolyte	AC // AC	1Me_3BuImBF_4	111	3.5	4.1	[363]
Ionic liquid electrolyte	KMC // AC	1 M Et4NBF4 / AC	98	2.7	171	[365]
Ionic liquid electrolyte	GNS // GNS	BMP–DCA	80	3.3	140	[367]
Ionic liquid electrolyte	N-RGO // N-RGO	BMP–DCA	764.53	4.0	245	[368]
Ionic liquid electrolyte	MnO_2 on Ni foam	$LiClO_4$ / 2-oxazolidinone	350	2.5	304	[369]
Ceramic- ionic liquid electrolyte	AC // AC	LATP with 13 wt% EMIM BF_4	181	1	6.1	[389]
Polymer in ceramic electrolyte	AC // AC	LATP with PEO/PEG	100	2	14	[390]

capacitance retention for 10,000 cycles to demonstrate good cycling stability.

As discussed previously, the overpotential has a clear role in expanding the voltage window of the device. Many fabricated devices operate in a potential range smaller than what their electrolyte can sustain. This is better explained in Fig. 28, which shows a practical potential range of a supercapacitor. It provides a stable potential range of the electrolyte for the supercapacitor as discussed by Yu et al. [19] It can be observed that there is a difference between the practical voltage range and the available potential range because the capacitive potential ranges of the two electrodes (combined) are more than what is harnessed [19,402]. The Capacitive potential range of the electrodes is the maximum potential range within which they undergo redox reaction and show pseudocapacitive charge storage without any permanent damage to the electrode's structure, composition and capacitive behavior. This capacitive potential range varies with different active materials, especially in those cases where the faradaic potential window of cathode and anode do not overlap. In such cases, an even wider difference might be visible between the practical and available potential range [402]. On the other hand, the stable potential range of the electrolyte refers to the range between the onset of HER and OER at anode and cathode, respectively. Hence, the maximum potential on the anodic side is given by the more positive one between- the 'minimum capacitive potential of anode' and the onset of HER, as shown in Fig. 28. Similarly, the maximum potential on the cathodic side is given by the more negative one among 'maximum capacitive potential of cathode' and the onset of OER. Thus it can be clearly seen that there exist a possibility of extending the practical voltage window of the supercapacitor device by either obtaining a higher overpotential for H_2 and/or O_2 evolution or selection of appropriate anode and cathode active material with matching capacitive potential range.

Another important aspect that can be attributed to the mismatch of 'practical' and 'available' potential ranges of a supercapacitor is "Potential of Zero Charge." This is represented as P_{0V} in Figs. 24 and 25 (a-b). It is defined as the potential of both electrodes when the supercapacitor operates at 0 V [19]. It also represents the cut-off potentials of the anode and cathode, which could be further determined by their respective open circuit potential (OCP), when the supercapacitor is at 0 V (non-operational). It is believed to be one of the most important parameters for determining the potential ranges of an anode, cathode, and the overall device. [19,402,403] For a charge-balanced supercapacitor (at the cut-off potential), the anode and cathode potential range distributes itself equally on either side of the P_{0V}. Hence P_{0V} lies in the middle of the practical potential range (Figs. 24 and 25 (a-b)). Therefore, when the device starts to charge, the potential on both electrodes increases at the same rate but in opposite directions. As soon as either of the two electrodes reaches the upper (P_U) or lower limit (P_L) potential of the electrolyte (as shown in Fig. 29 (a)), the maximum voltage of the device has been achieved. This leads to an unused potential range on either the cathode side (if the anode reached electrolyte decomposition potential first) or the anode side (if the cathode reached electrolyte decomposition potential first). Hence the relative position of P_{0V} and the potential variation rates on either side together govern the voltage window of an assembled supercapacitor

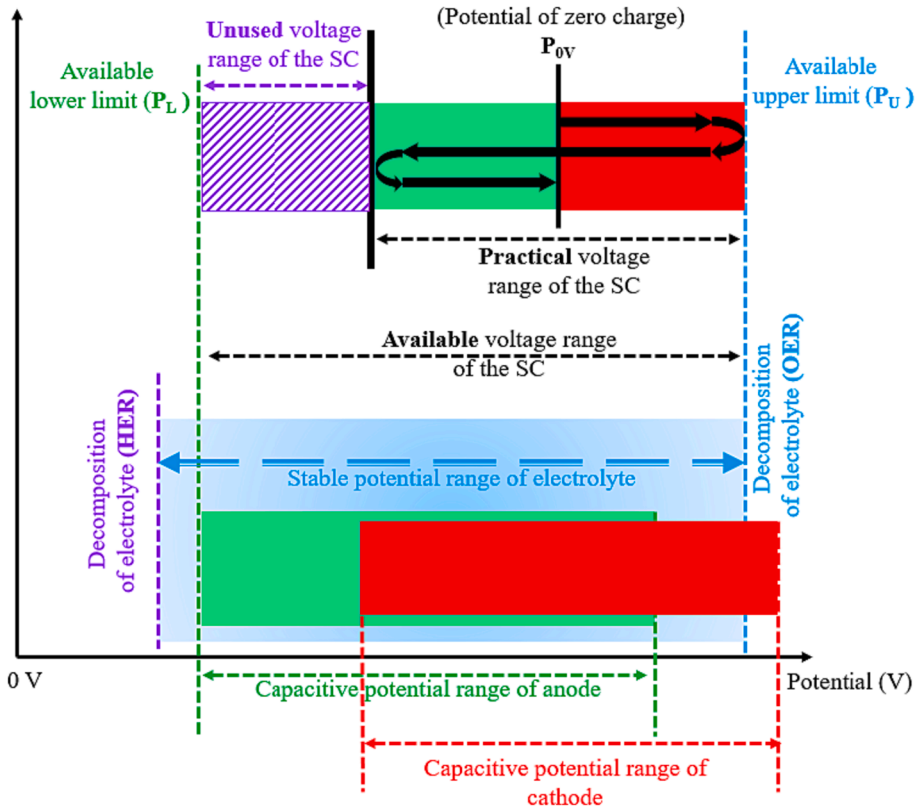

Fig. 28. Schematic illustration of the 'available potential range' and 'practical potential range' of a supercapacitor. Also, the figure shows how the available potential range can be obtained as a capacitive range of the anode and cathode and the hydrogen and oxygen potential of the electrolyte.

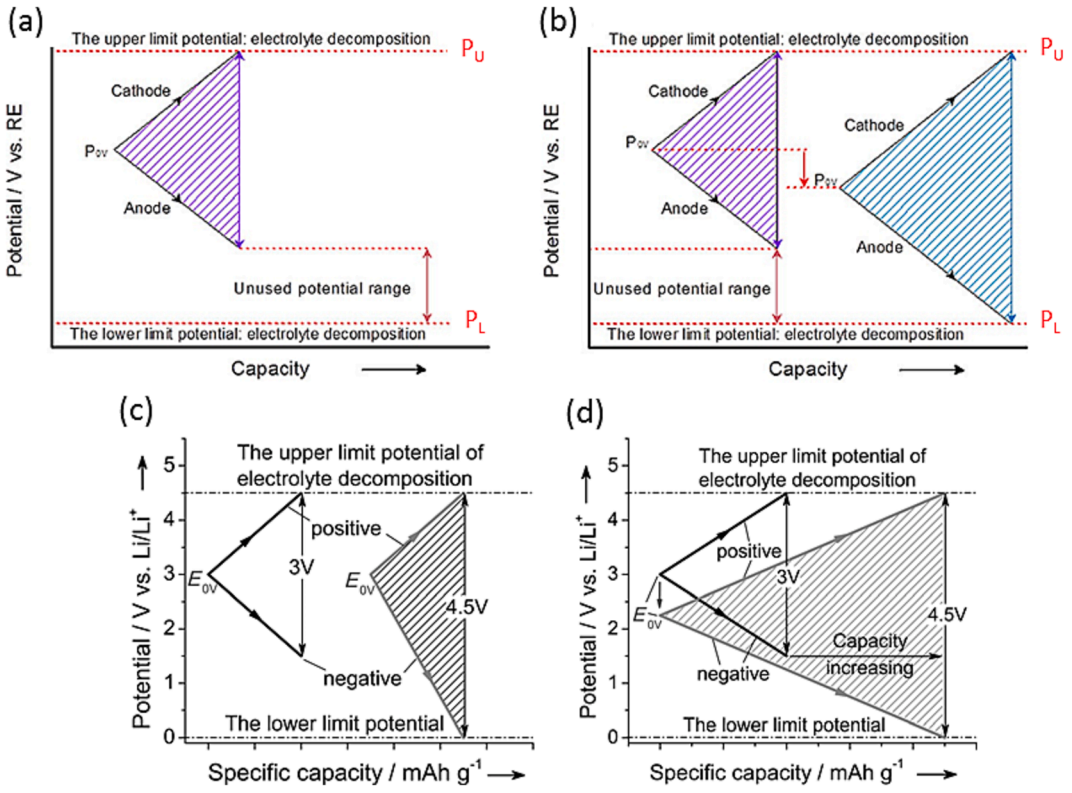

Fig. 29. A) figure shows the potential variation vs. capacity of electrodes in an assembled supercapacitor device. it also highlights the relative positions of the potential of zero charge (p_{0V}), upper (P_U) and lower (P_L) potential limits of electrolyte decomposition and an unused potential range. RE refers to the reference electrode. b) Controlled tuning of P_{0V} by optimization of surface charge to enhance the voltage window and energy density of the overall device. Reproduced with permission from reference [401] copyright 2018. (c) The enhancement of working voltage through increasing mass loading on the electrode by Weng et al. [402] (here E_{0V} is analogous to P_{0V}). Reproduced with permission from reference [402] copyright 2013. d) Enhancement of the working voltage via electrochemical charge injection to tune E_{0V} (or P_{0V}) to get a tenfold increase in energy density and significantly enhanced specific capacity, Reproduced with permission from reference [402] copyright 2013.

device. Controlled tuning of the relative position of P_{0V} could be used to harness the unused potential window. Along with this, Yu et al. have also highlighted some other methods that could be used to extend the voltage window of aqueous electrolyte-based supercapacitors (though it can be extended to non-aqueous as well) [401].

Controlled tuning of the potential of zero charge (P_{0V}): As discussed above, when an aqueous supercapacitor device is assembled, many times there exist an unused potential range due to the relative positioning of P_{0V} with respect to lower (P_L) and upper (P_U) potential limits of electrolyte. Since P_{0V} is governed by the open-circuit potentials of the anode (OCP_1) and the cathode (OCP_2), they distribute themselves equally about this mean position when supercapacitor starts/stops at 0 V (Figs. 28 and 25). Hence P_{0V} is approximately given by the mean of the OCP_1 and OCP_2 [19].

$$P_{0V} = \frac{1}{2}(OCP_1 + OCP_2) \tag{37}$$

In the above eq., OCP_1 and OCP_2 can be determined by a three-electrode study using a reference electrode [276,402]. In order to utilize the full potential range, this P_{0V} should be tuned to such a position (on the potential scale) that it aligns with the arithmetic mean of upper and lower potential limits of electrolytes (P_U and P_L, respectively). This is shown in Fig. 29 (b). Thus, the new desired value of P_{0V} is given by P'_{0V}. [19]

$$P'_{0V} = \frac{1}{2}(P_L + P_U) \tag{38}$$

Weng et al. [402] first investigated this mechanism of tuning the P_{0V} via charge injection, modifying the surface charge of the electrodes for a carbon-based supercapacitor in an organic electrolyte. Graphene, multi-walled carbon nanotube (MWCNT), single-walled carbon nanotube (SWCNT) and hierarchical porous graphitic carbon (HPGC) were used for electrode material, while 1 M $LiPF_6$/ethylene carbonate (EC) and dimethyl carbonate (DMC) were used as the electrolyte. Surprisingly, the group was able to get a tenfold increase in energy density, which resulted in a significant enhancement of operating voltage (from 3 V to 4.5 V) and high

specific capacitance. This is shown in Fig. 29 (d). Similar to their work, Yu et al. [19] performed the tuning of P_{0V} to align it with the mean of upper and lower potential limits in an aqueous electrolyte. Since P_{0V} is a result of the average OCPs of the anode and cathode (OCP_1 and OCP_2), it cannot be controlled directly. Hence, they pre-charged the anode with a constant negative voltage for 60 s to bring its OCP_1 to a new suitable value of OCP_1', as shown in Fig. 30. The value of OCP_1' could be given by eq. [19]

$$\frac{1}{2}\left(OCP_1^{'} + OCP_2\right) = \frac{1}{2}\left(P_L + P_U\right) \tag{39}$$

$$OCP_1^{'} + OCP_2 = P_L + P_U \tag{40}$$

$$OCP_1^{'} = P_L + P_U - OCP_2 \tag{41}$$

The above value of OCP_1' gave the desired open circuit potential. The anode was charged to controllably tune P_{0V} at the mean position of the upper and lower decomposition potential of the electrolyte. Using this pre-charging method, they were able to extend the voltage window from 1.4 V to 1.8 V and achieved a two-fold increase in the device's energy density.

In another work, Wang and his co-workers [404] studied the effect of temperature on the surface charge of an EDLC electrode. They found that these electrodes could be charged by heating. In this case, the charging is due to a coupled thermo-electrochemical effect. This happens due to the faster kinetics of the electrode induced by heating. This could be another approach to modify P_{0V} if the amount of heat could be controlled. Another method to modify surface charge and control P_{0V}, is via functionalization of electrode surface with hydroxyl group (–OH), carboxyl group (–COOH), amino group (–NH_2, –NH), etc. After ionization, the surface charge can be modified by controlling the amount of these functional groups. Only minimal research can be found in this direction but it offers a more permanent solution of surface charge modification and controlled tuning of P_{0V} for supercapacitors.

This pre-charging strategy is a general concept and can be used for both aqueous and organic electrolytes. However, a pre-charged electrode is thermodynamically unstable and has a quick tendency for self-discharging. Therefore, a better strategy is to analyze and choose the right combination of anode and cathode material, providing the lowest difference between the original open circuit potential and pre-charging potential.

Voltage enhancement through additives: Besides working on the strategies to enhance voltage windows through electrode material

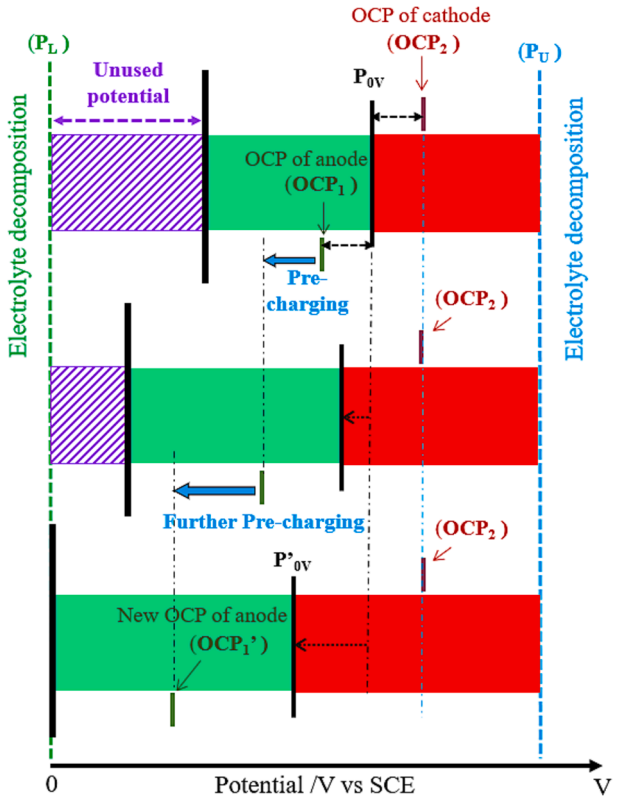

Fig. 30. The schematic shows the pre-charging strategy using a constant potential on one of the electrodes (here, anode) to efficiently tune P_{0V} such that it aligns with the geometric mean of upper and lower evolution potentials of the electrolyte. This enables the complete utilization of the potential window on both electrodes.

and properties, importance must also be given to the electrolyte [330]. The electrolyte decomposition is one of the key parameters that can significantly limit the voltage window. In aqueous electrolytes, it is limited to 1.23 V [93,276,277] (without considering overpotential and other influencing factors). OEs and ILs can provide a much wider voltage window due to their much higher decomposition potentials [70,281–283]. In recent years, research has been accelerated towards the development of a new kind of additive known as redox additives to the electrolyte, which not only facilitates ionic conduction but also shows redox-type charge storage at their redox potentials [405].

Redox-active additives have been widely researched for their charge storage ability by facilitating pseudocapacitance in electrochemical capacitors [406]. However, very little has been investigated on how redox-active additives could enhance the working voltage window of these supercapacitors. Chun et al. [407] have investigated a series of redox-active couples like vanadium complexes, indigo carmine, copper salts, quinones, phenylenediamine, halides, methylene-blue, etc. They have found that besides having a significant contribution to the capacitance, these redox-active additives also enlarge the voltage window of the supercapacitor. This could be made possible by carefully choosing a redox-active additive with its redox potential near the decomposition potential of electrolytes. As a result, once the decomposition potential is reached, these redox additives exhibit faster reaction kinetics and are prioritized for charge transfer over the electrolyte ions. Hence, electrolyte ions end up waiting while the potential exceeds the decomposition

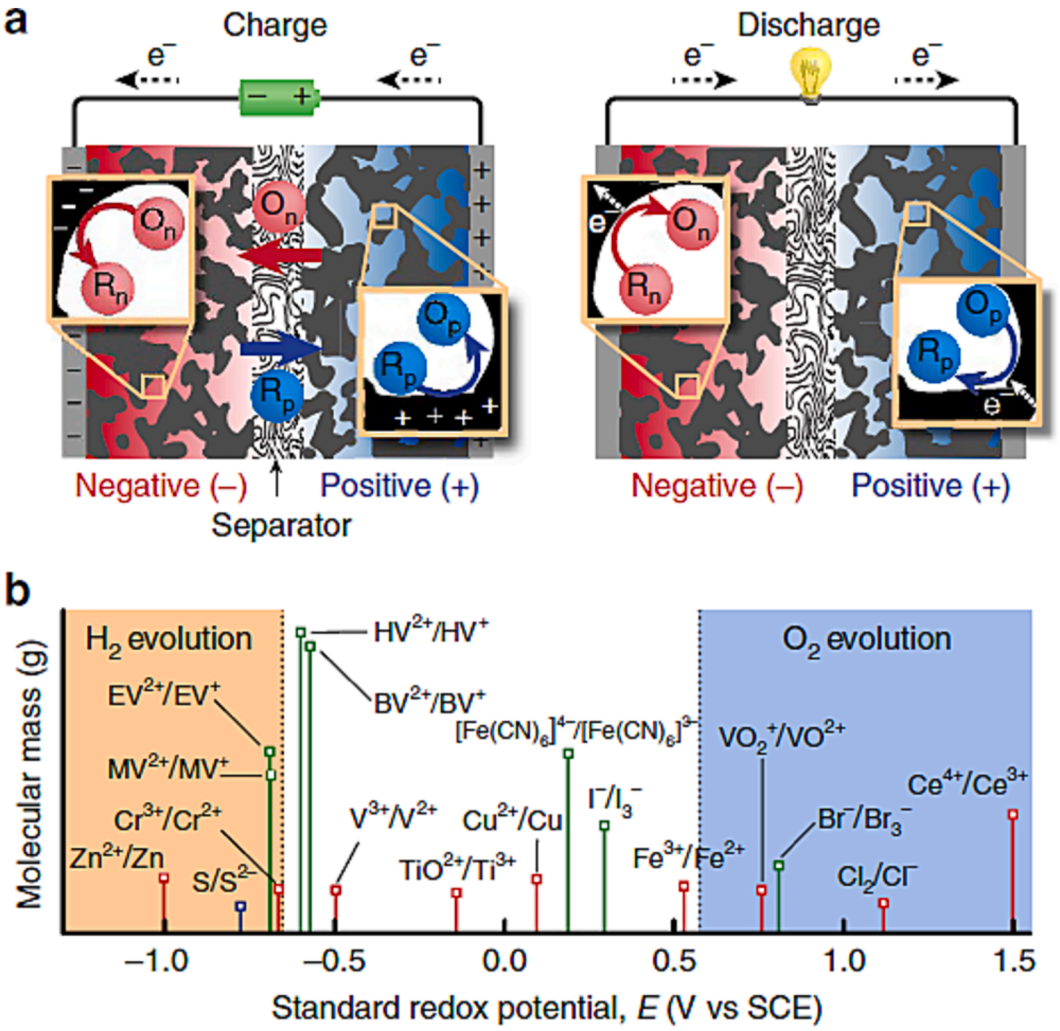

Fig. 31. (a) Figure shows the schematics of the functioning mechanism of redox additives participating in charge storage in negative and positive electrodes of a supercapacitor. O_p/R_p (Catholyte) represents the redox couple interacting with the positive electrode, which is oxidized on charging and reduced when discharged. The O_n/R_n represents a redox couple interacting at the negative electrode, which reduces charging and oxidizes upon discharging. (b) Reduction potentials of various redox couples relative to the thermodynamic stability of water at a neutral pH electrolyte (white area). Lines colored in blue, green and red represent Basic (1 M base) [409], neutral and acid (1 M acid) conditions, respectively [410–416]. Some compounds are abbreviated as MV-methyl viologen, BV- benzyl viologen, HV-heptyl viologen, EV-ethyl viologen, SCE- standard calomel electrode. Reproduced with permission from reference [407] copyright 2015. (For interpretation of the references to colour in this figure legend, the reader is referred to the web version of this article.)

limits. This leads to a higher voltage window by suppression of HER and OER reaction by faster kinetics exhibited by redox additives. Fig. 31 shows the plot of various redox couples vs. their reduction potentials (against saturated calomel electrode/SCE), compiled by Chun et al. [407] Based on this, the group concluded that to avoid self-discharging effects, negatively charged couples could be used as redox additives for cathodes. This would mean Br^-/ Br_3^-, I^-/ I_3^- and $[Fe(CN)_6]^{4-}$ / $[Fe(CN)_6]^{6-}$ could serve as useful redox couple to suppress the OER on the cathode due to their quick redox kinetics, extending the upper limit of the voltage window. On the other hand, redox couples like HV^{2+}/ HV^+ (HV = heptyl viologen), BV^{2+}/ BV^+ (BV = benzyl viologen), EV^{2+}/ EV^+ (EV = ethyl viologen) and MV^{2+}/ MV^+ (MV = methyl viologen) have their reduction potentials near (or slightly more negative than) the hydrogen evolution potentials. Therefore, these ions have the ability to suppress the HER, through faster reaction kinetics on the anode, and extend the lower limit of the voltage window.

In another work, Hwang et al. [408] extended the voltage window of the activated carbon-based supercapacitor up to 2 V by adding 0.1 M $[Fe(CN)_6]^{4-}$ / $[Fe(CN)_6]^{6-}$ into the pre-existing 1 M Na_2SO_4 aqueous electrolyte. As per their findings, this extension of the voltage window was achieved due to (i) high solvation energies of Na^+ and SO_4^{2-} ions, and (ii) fast redox kinetics of $[Fe(CN)_6]^{4-}$ / $[Fe(CN)_6]^{6-}$ near the reduction potentials of electrolyte. However, it is worth noting that when the concentration of $[Fe(CN)_6]^{4-}$ / $[Fe(CN)_6]^{6-}$ was increased to 0.2 M to extend the voltage further, the device could not be charged even up to 2 V due to increased leakage current. Therefore, the concentration of the redox couple needs to be carefully optimized to avoid self-discharging effects.

10. Summary and prospects

The supercapacitor-based energy storage is a rapidly evolving area of energy storage. As a result of the harmonized effort from the supercapacitor community, consistent improvement in its energy density, power density, cycle life and other performance parameters has been achieved since its inception. To adequately equip supercapacitors to compete in the upcoming EV revolution, it is necessary to improve the overall performance of the existing supercapacitors. The electric car industry eyes on supercapacitor's inherent ability to offer a high-power density due to its surface charge storage mechanism. However, supercapacitors struggle to make their energy density sufficient to function as independent energy storage devices. One of the most important parameters enhancing the energy density is the device output voltage, which has a quadratic effect on its energy density. This review provides an exhaustive discussion of the factors affecting the voltage window of supercapacitors from the available literature. It can be summarized along with the future prospects under the following points.

(1) First, this review covers the overall classification of supercapacitors based on (1) charge storage mechanisms and (2) electrode configurations.

Making such a classification is very important to avoid any ambiguity that could arise when using terminologies like asymmetric, hybrid, etc. Even though this review attempts to do a categorical classification, it remains challenging to set a global standard when assigning a proper nomenclature, its acceptance, and a standard performance comparison matrix. For example, using different electrolytes (or the same electrolyte with a different concentration or pH) for the same set of anode and cathode material will result in different performance outputs.

(2) As the research advances more into the charge storage and transport mechanisms, it has been established that the output voltage window of supercapacitors is a result of energy interactions between the (a) two electrodes (among themselves), (b) electrolyte (stability window), and (c) the electrode–electrolyte interface. Energy interactions among the two electrodes are best described by their work functions, which is the net sum of their electrochemical potential and surface potential. The electrochemical potential is a bulk property of the electrode active material. In contrast, the surface potential is a surface phenomenon that depends on surface adsorbates on the electrode. These adsorbates could be any other functional groups, electrolyte ions, polarized solvent molecules, etc. Since supercapacitors operate by storing charges at the surface, it becomes imperative to understand this surface potential and learn how it affects the overall work function of the electrode.

Though some modeling studies might help to better understand this effect, some in-situ experiments must be designed to measure modifications in the work function of electrodes due to these adsorbates while a supercapacitor electrode is in operation. A kelvin probe force microscopy-based experiment could be used to perform an in-situ, three-electrode-based electrochemical characterization test (like the galvanic charge–discharge test). As the electrode charges and discharges, its work function could be measured along with its performance. Different electrolytes can be used to uncover the effects of surface adsorbates on the work function and operating voltage range of the electrode. A similar test could be performed for an assembled device too.

(3) On the other hand, the electrochemical potential of the electrode active materials is an exhibition of its fermi level and an interplay of three energies (i) electron affinity, (ii) ionization potential, and (iii) its group electronegativity. As discussed, it is a bulk property and is dependent on a number of factors like impurities in the crystal, defects in the lattice, added dopants, crystal structure and chemical state of the electrode active material. From the discussed models of MoO_3 (anode) and MnO_2 (cathode), we get a glimpse of how defect states in MoO_3 and charge switching states of MnO_2 control the energy interactions (fermi level) and affect the electrochemical potential as reduction/oxidation reactions proceed in a functional supercapacitor. As the electrochemical potentials of anode and cathode change, they increase/decrease the work functions of the anode and cathode (in an opposite nature) to generate a stable voltage window for the electrode material.

Based on this discussion, it is evident that the voltage window is dependent on the work function difference of the anode and cathode material. The larger the difference in work functions, the higher the voltage window that can be achieved. This provides a tremendous opportunity to tune the voltage window if the work function of the electrodes can be selectively modulated. This can be achieved by modifying the electrochemical potential in the bulk (of the material) via introducing appropriate dopants in the crystal lattice of the active electrode materials. The energy states of the dopant can interfere with those of the host active material in the bulk. This can result in the re-positioning of its CBM and VBM, thereby shifting its fermi level. It can change the bulk electrochemical potential, which would be marked by a modified work function value. Hence the voltage window could be tuned.

(4) Besides the voltage window offered by the electrodes, it is essential to see how much of that voltage window overlaps with the stable potential range of the electrolyte. The stable potential range of the electrolyte is marked by energies of its HOMO and LUMO levels. As the electrolyte forms an interface at the electrode's surface, the electrode's work function interacts with the electrolyte's HOMO/LUMO level. As the voltage sweeps and the work function on either of the electrode cross the respective HOMO/LUMO level, the electrolyte dissociates. If the electrolyte is water-based (aqueous), an evolution of H_2 or O_2 is seen upon its dissociation.

In order to make full use of the voltage window based on the electrode's work function difference, an appropriate electrolyte having its stable potential range overlapping to that of the electrodes should be used. However, further research can guide us on how to thermodynamically extend the HOMO-LUMO range of the electrolyte. Recently, Suo et al. [417] prepared a special water-in-salt electrolyte system by dissolving an excessive amount of lithium bis (trifluro-methane sulphonyl)imide (LiTFSI) salt in water. Here water-in-salt system refers to a state where both the weight and volume of the salt outweigh those of the solvent. LiTFSI exhibits extremely high solubility in water and can hold up 20 mol Kg^{-1} of water without getting hydrolyzed. Due to this, a 21 *m* (molality) concentration of the electrolyte could be prepared, which had a stable potential range of 3 V. This became possible because, for the water-in-salt system, the average number of water molecules required to solvate each ion is far less compared to the regular salt-in-water system. It means that the solvation sheet has a very small number of polarized water molecules. Thus, the onset of HER and OER have pushed them apart beyond their thermodynamic range. This extends the HOMO-LUMO range. More such systems should be synthesized and investigated. This could help in fabricating aqueous-based high-voltage supercapacitors, which are cheaper and safer to operate.

(5) Similar to the thermodynamic approach of extending the stable potential range of the electrolyte, there is a kinetic approach to achieve the same objective, which is called overpotential. In a neutral aqueous electrolyte, this is naturally achieved due to the slower kinetics of the HER and OER. However, as the pH of the electrolyte shifts towards the acidic or basic system, the increase in the concentration of H^+ / OH^- ions slows down the reaction kinetics of the HER and OER, resulting in overpotential. This extends the stable potential range of the electrolyte.

In order to further extend the stable potential range, kinetically (i.e., by virtue of overpotential), certain additives like Br^-/ Br_3^-, I^-/ I_3^- and $[Fe(CN)_6]^{4-}$ / $[Fe(CN)_6]^{6-}$ could be added to the electrolyte for suppressing OER on the cathode. Similarly, on the anode side, redox couples like HV^{2+}/ HV^+ (HV = heptyl viologen), BV^{2+}/ BV^+ (BV = benzyl viologen), EV^{2+}/ EV^+ (EV = ethyl viologen) and MV^{2+}/ MV^+ (MV = methyl viologen) could suppress the HER due to their faster reaction kinetics.

(6) The extension of the voltage window of an assembled device can also be achieved by optimizing the surface charge on the electrodes. This can be done by aligning the potential of zero charge (P_{0V}) of the two electrodes exactly in the middle of the upper (P_U) and lower (P_L) potential limit of the electrolyte. This could be naturally achieved by choosing the right combinations of electrode material and electrolyte. This is a universal approach and works with any type of electrode or electrolyte.

11. Conclusions

Supercapacitors have been popular since the beginning of this century but still have not reached their full potential in the commercial market compared to conventional Li-ion batteries. In spite of having excellent power density, very high cycling stability and superior safety, it is still not a popular choice for energy storage devices due to its low energy density. The factor that quadratically affects its energy density is the voltage up to which the device can be charged/discharged without any detrimental effect on its performance. This study has tried to cover all aspects that govern the overall voltage of the devices. Through the approach of electrode energetics and their interaction with the energy levels of electrolytes, this review has tried to uncover and encompass all the factors affecting the voltage window in an asymmetric supercapacitor. Since symmetric configuration has a limited potential range due to its design, it has not been the focus of this work. However, many aspects of this study, like energy interactions with electrolytes, overpotential, tuning the potential of zero charge (P_{0V}), and addition of redox additives, are equally applicable to the symmetric design.

This review highlights the factors affecting the overall voltage window and methods to extend. It also discusses the work function-based new strategies to effectively tune the voltage window of the supercapacitors. This liberty to effectively tune the voltage window enables fabricating high-performing and cheaper devices using scalable technologies suitable for industrial production on a massive scale.

Declaration of Competing Interest

The authors declare that they have no known competing financial interests or personal relationships that could have appeared to influence the work reported in this paper.

Data availability

No data was used for the research described in the article.

Acknowledgments

JT acknowledges the National Science Foundation (CAREER: ECCS-1351757 Supplement- IIP 1839459 and IIP-2122779) for the financial support.

References

[1] Sergeev A. Lamborghini Sian Debuts As Brand's First Electrified Production Car. Motor 2019;1:368588.
[2] Hurd B. Lamborghini uses supercapacitors in its most powerful car ever. Green Car Reports 2019:1124923.
[3] Li C, Islam MM, Moore J, Sleppy J, Morrison C, Konstantinov K, et al. Wearable energy-smart ribbons for synchronous energy harvest and storage. Nat Commun 2016;7:1–10.
[4] Varma J, Sambath Kumar K, Seal S, Rajaraman S, Thomas J. Fiber-type solar cells, nanogenerators, batteries, and supercapacitors for wearable applications. Adv Sci 2018;5:1800340.
[5] Kumar KS, Choudhary N, Jung Y, Thomas J. Recent advances in two-dimensional nanomaterials for supercapacitor electrode applications. Acs Energy Lett 2018;3:482–95.
[6] Fan Z, Yan J, Wei T, Zhi L, Ning G, Li T, et al. Asymmetric supercapacitors based on graphene/MnO2 and activated carbon nanofiber electrodes with high power and energy density. Adv Funct Mater 2011;21:2366–75.
[7] Harrop P. Supercapacitors to the rescue. Off Grid Energy Independence 2013:5106.
[8] Goodwood. First one up the drive. The Economist; 2014.
[9] Jaafar A, Sareni B, Roboam X, Thiounn-Guermeur M. Sizing of a hybrid locomotive based on accumulators and ultracapacitors. In: 2010 IEEE Vehicle Power and Propulsion Conference: IEEE; 2010. p. 1-6.
[10] Végvári Z. Supercapacitors and Their Military Applicability. HONVÉDSÉGI SZEMLE: A MAGYAR HONVÉDSÉG KÖZPONTI FOLYÓIRATA. 2019; 147: 38-49.
[11] Meng C, Gall OZ, Irazoqui pp.. A flexible super-capacitive solid-state power supply for miniature implantable medical devices. Biomed Microdevices 2013;15:973–83.
[12] Castelli Dezza F, Musolino V, Piegari L, Rizzo R. Hybrid battery–supercapacitor system for full electric forklifts. IET Electr Syst Transp 2019;9:16–23.
[13] Miller JR, Burke AF. Electrochemical capacitors: challenges and opportunities for real-world applications. Electrochem Soc Interface 2008;17:53.
[14] Conway BE. Electrochemical supercapacitors: scientific fundamentals and technological applications. Springer Science & Business Media; 2013.
[15] Sahalianov I, Singh SK, Tybrandt K, Berggren M, Zozoulenko I. The intrinsic volumetric capacitance of conducting polymers: pseudo-capacitors or double-layer supercapacitors? RSC Adv 2019;9:42498–508.
[16] Yamada A, Goodenough JB. Keggin-type heteropolyacids as electrode materials for electrochemical supercapacitors. J Electrochem Soc 1998;145:737.
[17] Greiner MT, Chai L, Helander MG, Tang WM, Lu ZH. Transition metal oxide work functions: the influence of cation oxidation state and oxygen vacancies. Adv Funct Mater 2012;22:4557–68.
[18] Salanne M, Rotenberg B, Naoi K, Kaneko K, Taberna P-L, Grey CP, et al. Efficient storage mechanisms for building better supercapacitors. Nat Energy 2016;1:1–10.
[19] Yu M, Lin D, Feng H, Zeng Y, Tong Y, Lu X. Boosting the energy density of carbon-based aqueous supercapacitors by optimizing the surface charge. Angew Chem 2017;129:5546–51.
[20] Roldán S, Barreda D, Granda M, Menéndez R, Santamaría R, Blanco C. An approach to classification and capacitance expressions in electrochemical capacitors technology. Phys Chem Chem Phys 2015;17:1084–92.
[21] Gogotsi Y. What nano can do for energy storage. ACS Publications; 2014.
[22] Simon P, Gogotsi Y, Dunn B. Where do batteries end and supercapacitors begin? Science 2014;343:1210–1.
[23] Forghani M, Donne SW. Method comparison for deconvoluting capacitive and pseudo-capacitive contributions to electrochemical capacitor electrode behavior. J Electrochem Soc 2018;165:A664.
[24] Patra A, Namsheer K, Jose JR, Sahoo S, Chakraborty B, Rout CS. Understanding the charge storage mechanism of supercapacitors: in situ/operando spectroscopic approaches and theoretical investigations. J Mater Chem A 2021;9:25852–91.
[25] Choudhary N, Li C, Moore J, Nagaiah N, Zhai L, Jung Y, et al. Asymmetric supercapacitor electrodes and devices. Adv Mater 2017;29:1605336.
[26] Cherusseri J, Kumar KS, Choudhary N, Nagaiah N, Jung Y, Roy T, et al. Novel mesoporous electrode materials for symmetric, asymmetric and hybrid supercapacitors. Nanotechnology 2019;30:202001.
[27] Choudhary N, Li C, Chung H-S, Moore J, Thomas J, Jung Y. High-performance one-body core/shell nanowire supercapacitor enabled by conformal growth of capacitive 2D WS2 layers. ACS Nano 2016;10:10726–35.
[28] Cherusseri J, Kar KK. Self-standing carbon nanotube forest electrodes for flexible supercapacitors. RSC Adv 2015;5:34335–41.
[29] Zhang LL, Zhao X. Carbon-based materials as supercapacitor electrodes. Chem Soc Rev 2009;38:2520–31.
[30] Zhai Y, Dou Y, Zhao D, Fulvio PF, Mayes RT, Dai S. Carbon materials for chemical capacitive energy storage. Adv Mater 2011;23:4828–50.
[31] Kötz R, Carlen M. Principles and applications of electrochemical capacitors. Electrochim Acta 2000;45:2483–98.
[32] Frackowiak E, Beguin F. Carbon materials for the electrochemical storage of energy in capacitors. Carbon 2001;39:937–50.
[33] Pandolfo AG, Hollenkamp AF. Carbon properties and their role in supercapacitors. J Power Sources 2006;157:11–27.
[34] Frackowiak E, Beguin F. Electrochemical storage of energy in carbon nanotubes and nanostructured carbons. Carbon 2002;40:1775–87.
[35] Cherusseri J, Kar KK. Hierarchically mesoporous carbon nanopetal based electrodes for flexible supercapacitors with super-long cyclic stability. J Mater Chem A 2015;3:21586–98.
[36] Cherusseri J, Kar KK. Ultra-flexible fibrous supercapacitors with carbon nanotube/polypyrrole brush-like electrodes. J Mater Chem A 2016;4:9910–22.
[37] Cherusseri J, Kar KK. Hierarchical carbon nanopetal/polypyrrole nanocomposite electrodes with brush-like architecture for supercapacitors. Phys Chem Chem Phys 2016;18:8587–97.
[38] Zhao X, Sánchez BM, Dobson PJ, Grant PS. The role of nanomaterials in redox-based supercapacitors for next generation energy storage devices. Nanoscale 2011;3:839–55.
[39] Augustyn V, Simon P, Dunn B. Pseudocapacitive oxide materials for high-rate electrochemical energy storage. Energ Environ Sci 2014;7:1597–614.
[40] Conway BE, Birss V, Wojtowicz J. The role and utilization of pseudocapacitance for energy storage by supercapacitors. J Power Sources 1997;66:1–14.

[41] Rauda IE, Augustyn V, Dunn B, Tolbert SH. Enhancing pseudocapacitive charge storage in polymer templated mesoporous materials. Acc Chem Res 2013;46:1113–24.
[42] Trasatti S, Buzzanca G. Ruthenium dioxide: a new interesting electrode material. Solid state structure and electrochemical behaviour. J Electroanal Chem Interfacial Electrochem 1971;29:A1–5.
[43] Brousse T, Bélanger D, Long JW. To be or not to be pseudocapacitive? J Electrochem Soc 2015;162:A5185.
[44] Conway B. Two-dimensional and quasi-two-dimensional isotherms for Li intercalation and upd processes at surfaces. Electrochim Acta 1993;38:1249–58.
[45] Sudha V, Sangaranarayanan M. Underpotential deposition of metals: structural and thermodynamic considerations. J Phys Chem B 2002;106:2699–707.
[46] Herrero E, Buller LJ, Abruña HD. Underpotential deposition at single crystal surfaces of Au, Pt, Ag and other materials. Chem Rev 2001;101:1897–930.
[47] Toupin M, Brousse T, Bélanger D. Charge storage mechanism of MnO2 electrode used in aqueous electrochemical capacitor. Chem Mater 2004;16:3184–90.
[48] Li H, Wang J, Chu Q, Wang Z, Zhang F, Wang S. Theoretical and experimental specific capacitance of polyaniline in sulfuric acid. J Power Sources 2009;190:578–86.
[49] Peng C, Hu D, Chen GZ. Theoretical specific capacitance based on charge storage mechanisms of conducting polymers: Comment on 'Vertically oriented arrays of polyaniline nanorods and their super electrochemical properties'. Chem Commun 2011;47:4105–7.
[50] Simon P, Gogotsi Y. Materials for electrochemical capacitors. Nanoscience and technology: a collection of reviews from Nature journals. 2010:320-9.
[51] Kim JW, Augustyn V, Dunn B. The effect of crystallinity on the rapid pseudocapacitive response of Nb2O5. Adv Energy Mater 2012;2:141–8.
[52] Augustyn V, Come J, Lowe MA, Kim JW, Taberna P-L, Tolbert SH, et al. High-rate electrochemical energy storage through Li+ intercalation pseudocapacitance. Nat Mater 2013;12:518–22.
[53] Lamba P, Singh P, Singh P, Singh P, Kumar A, Gupta M, et al. Recent advancements in supercapacitors based on different electrode materials: classifications, synthesis methods and comparative performance. J Storage Mater 2022;48:103871.
[54] Sambath Kumar K, Cherusseri J, Thomas J. Two-dimensional Mn3O4 nanowalls grown on carbon fibers as electrodes for flexible supercapacitors. ACS Omega 2019;4:4472–80.
[55] Cherusseri J, Choudhary N, Kumar KS, Jung Y, Thomas J. Recent trends in transition metal dichalcogenide based supercapacitor electrodes. Nanoscale Horiz 2019;4:840–58.
[56] Pell WG, Conway BE. Peculiarities and requirements of asymmetric capacitor devices based on combination of capacitor and battery-type electrodes. J Power Sources 2004;136:334–45.
[57] Conte M. Supercapacitors technical requirements for new applications. Fuel Cells 2010;10:806–18.
[58] Ramachandran T, Sana SS, Kumar KD, Kumar YA, Hegazy H, Kim SC. Asymmetric supercapacitors: Unlocking the energy storage revolution. J Storage Mater 2023;73:109096.
[59] Brousse T, Taberna P-L, Crosnier O, Dugas R, Guillemet P, Scudeller Y, et al. Long-term cycling behavior of asymmetric activated carbon/MnO2 aqueous electrochemical supercapacitor. J Power Sources 2007;173:633–41.
[60] Qu D, Shi H. Studies of activated carbons used in double-layer capacitors. J Power Sources 1998;74:99–107.
[61] Shao Y, El-Kady MF, Sun J, Li Y, Zhang Q, Zhu M, et al. Design and mechanisms of asymmetric supercapacitors. Chem Rev 2018;118:9233–80.
[62] Cericola D, Kötz R. Hybridization of rechargeable batteries and electrochemical capacitors: Principles and limits. Electrochim Acta 2012;72:1–17.
[63] Li J, Gao F. Analysis of electrodes matching for asymmetric electrochemical capacitor. J Power Sources 2009;194:1184–93.
[64] Amatucci GG, Badway F, Du Pasquier A, Zheng T. An asymmetric hybrid nonaqueous energy storage cell. J Electrochem Soc 2001;148:A930.
[65] Naoi K, Naoi W, Aoyagi S, Miyamoto J-i, Kamino T. New generation "nanohybrid supercapacitor". Acc Chem Res 2013;46:1075–83.
[66] Naoi K. 'Nanohybrid capacitor': the next generation electrochemical capacitors. Fuel Cells 2010;10:825–33.
[67] Lukatskaya MR, Dunn B, Gogotsi Y. Multidimensional materials and device architectures for future hybrid energy storage. Nat Commun 2016;7:1–13.
[68] Naoi K, Ishimoto S, Miyamoto J-i, Naoi W. Second generation 'nanohybrid supercapacitor': evolution of capacitive energy storage devices. Energ Environ Sci 2012;5:9363–73.
[69] Khomenko V, Raymundo-Piñero E, Béguin F. A new type of high energy asymmetric capacitor with nanoporous carbon electrodes in aqueous electrolyte. J Power Sources 2010;195:4234–41.
[70] Khomenko V, Raymundo-Piñero E, Béguin F. High-energy density graphite/AC capacitor in organic electrolyte. J Power Sources 2008;177:643–51.
[71] Wang H, Yoshio M, Thapa AK, Nakamura H. From symmetric AC/AC to asymmetric AC/graphite, a progress in electrochemical capacitors. J Power Sources 2007;169:375–80.
[72] Snook GA, Kao P, Best AS. Conducting-polymer-based supercapacitor devices and electrodes. J Power Sources 2011;196:1–12.
[73] Arbizzani C, Mastragostino M, Meneghello L. Polymer-based redox supercapacitors: A comparative study. Electrochim Acta 1996;41:21–6.
[74] Khomenko V, Raymundo-Pinero E, Béguin F. Optimisation of an asymmetric manganese oxide/activated carbon capacitor working at 2 V in aqueous medium. J Power Sources 2006;153:183–90.
[75] Brousse T, Toupin M, Belanger D. A hybrid activated carbon-manganese dioxide capacitor using a mild aqueous electrolyte. J Electrochem Soc 2004;151:A614.
[76] Yuan A, Zhang Q. A novel hybrid manganese dioxide/activated carbon supercapacitor using lithium hydroxide electrolyte. Electrochem Commun 2006;8:1173–8.
[77] Du X, Wang C, Chen M, Jiao Y, Wang J. Electrochemical performances of nanoparticle Fe3O4/activated carbon supercapacitor using KOH electrolyte solution. J Phys Chem C 2009;113:2643–6.
[78] Park JH, Park OO, Shin KH, Jin CS, Kim JH. An electrochemical capacitor based on a Ni (OH) 2/activated carbon composite electrode. Electrochem Solid State Lett 2001;5:H7.
[79] Laforgue A, Simon P, Fauvarque J, Mastragostino M, Soavi F, Sarrau J, et al. Activated carbon/conducting polymer hybrid supercapacitors. J Electrochem Soc 2003;150:A645.
[80] Di Fabio A, Giorgi A, Mastragostino M, Soavi F. Carbon-poly (3-methylthiophene) hybrid supercapacitors. J Electrochem Soc 2001;148:A845.
[81] Chang J, Jin M, Yao F, Kim TH, Le VT, Yue H, et al. Asymmetric supercapacitors based on graphene/MnO2 nanospheres and graphene/MoO3 nanosheets with high energy density. Adv Funct Mater 2013;23:5074–83.
[82] Du Pasquier A, Plitz I, Gural J, Badway F, Amatucci G. Power-ion battery: bridging the gap between Li-ion and supercapacitor chemistries. J Power Sources 2004;136:160–70.
[83] Chen F, Li R, Hou M, Liu L, Wang R, Deng Z. Preparation and characterization of ramsdellite Li2Ti3O7 as an anode material for asymmetric supercapacitors. Electrochim Acta 2005;51:61–5.
[84] Cericola D, Novák P, Wokaun A, Kötz R. Hybridization of electrochemical capacitors and rechargeable batteries: An experimental analysis of the different possible approaches utilizing activated carbon, Li4Ti5O12 and LiMn2O4. J Power Sources 2011;196:10305–13.
[85] Wu H, Rao CV, Rambabu B. Electrochemical performance of LiNi0. 5Mn1. 5O4 prepared by improved solid state method as cathode in hybrid supercapacitor. Mater Chem Phys 2009;116:532–5.
[86] Du Pasquier A, Laforgue A, Simon P, Amatucci GG, Fauvarque J-F. A nonaqueous asymmetric hybrid li4ti5 o 12/poly (fluorophenylthiophene) energy storage device. J Electrochem Soc 2002;149:A302.
[87] Du Pasquier A, Laforgue A, Simon P. Li4Ti5O12/poly (methyl) thiophene asymmetric hybrid electrochemical device. J Power Sources 2004;125:95–102.
[88] Roldán S, Blanco C, Granda M, Menéndez R, Santamaría R. Towards a further generation of high-energy carbon-based capacitors by using redox-active electrolytes. Angew Chem Int Ed 2011;50:1699–701.
[89] Roldan S, Granda M, Menendez R, Santamaría R, Blanco C. Mechanisms of energy storage in carbon-based supercapacitors modified with a quinoid redox-active electrolyte. J Phys Chem C 2011;115:17606–11.
[90] Roldán S, Granda M, Menéndez R, Santamaría R, Blanco C. Supercapacitor modified with methylene blue as redox active electrolyte. Electrochim Acta 2012;83:241–6.

[91] Roldán S, González Z, Blanco C, Granda M, Menéndez R, Santamaría R. Redox-active electrolyte for carbon nanotube-based electric double layer capacitors. Electrochim Acta 2011;56:3401–5.
[92] Lota G, Fic K, Frackowiak E. Alkali metal iodide/carbon interface as a source of pseudocapacitance. Electrochem Commun 2011;13:38–41.
[93] Demarconnay L, Raymundo-Piñero E, Béguin F. A symmetric carbon/carbon supercapacitor operating at 1.6 V by using a neutral aqueous solution. Electrochem Commun 2010;12:1275–8.
[94] Bello A, Barzegar F, Madito M, Momodu DY, Khaleed AA, Masikhwa T, et al. Stability studies of polypyrole-derived carbon based symmetric supercapacitor via potentiostatic floating test. Electrochim Acta 2016;213:107–14.
[95] Miller JR, Simon P. Electrochemical capacitors for energy management. Science Magazine 2008;321:651–2.
[96] Hall PJ, Mirzaeian M, Fletcher SI, Sillars FB, Rennie AJ, Shitta-Bey GO, et al. Energy storage in electrochemical capacitors: designing functional materials to improve performance. Energ Environ Sci 2010;3:1238–51.
[97] Chen P-C, Shen G, Shi Y, Chen H, Zhou C. Preparation and characterization of flexible asymmetric supercapacitors based on transition-metal-oxide nanowire/single-walled carbon nanotube hybrid thin-film electrodes. ACS Nano 2010;4:4403–11.
[98] Wang Y-g, Xia Y-y. A new concept hybrid electrochemical surpercapacitor: Carbon/LiMn2O4 aqueous system. Electrochem Commun 2005;7:1138–42.
[99] Yan J, Fan Z, Sun W, Ning G, Wei T, Zhang Q, et al. Advanced asymmetric supercapacitors based on Ni (OH) 2/graphene and porous graphene electrodes with high energy density. Adv Funct Mater 2012;22:2632–41.
[100] Kumar KS, Choudhary N, Pandey D, Hurtado L, Chung H-S, Tetard L, et al. High-performance flexible asymmetric supercapacitor based on rGO anode and WO3/WS2 core/shell nanowire cathode. Nanotechnology 2020;31:435405.
[101] Jiang H, Ma J, Li C. Mesoporous carbon incorporated metal oxide nanomaterials as supercapacitor electrodes. Wiley Online. Library 2012.
[102] Meyer J, Zilberberg K, Riedl T, Kahn A. Electronic structure of Vanadium pentoxide: An efficient hole injector for organic electronic materials. J Appl Phys 2011;110:033710.
[103] Smoluchowski R. Anisotropy of the electronic work function of metals. Phys Rev 1941;60:661.
[104] Li W, Li D. On the correlation between surface roughness and work function in copper. J Chem Phys 2005;122:064708.
[105] Wandelt K. The local work function: Concept and implications. Appl Surf Sci 1997;111:1–10.
[106] Ishii H, Sugiyama K, Ito E, Seki K. Energy level alignment and interfacial electronic structures at organic/metal and organic/organic interfaces. Adv Mater 1999;11:605–25.
[107] Steinberger I, Wandelt K. Ionization energies of valence levels in physisorbed rare-gas multilayers. Phys Rev Lett 1987;58:2494.
[108] Kwon KC, Choi KS, Kim SY. Increased work function in few-layer graphene sheets via metal chloride doping. Adv Funct Mater 2012;22:4724–31.
[109] Greiner M, Helander M, Wang Z, Tang WM, Qiu J, Lu Z. A metallic molybdenum suboxide buffer layer for organic electronic devices. Appl Phys Lett 2010;96:103.
[110] Cheng J, Sprik M. Alignment of electronic energy levels at electrochemical interfaces. PCCP 2012;14:11245–67.
[111] Trasatti S. The absolute electrode potential: an explanatory note (Recommendations 1986). Pure Appl Chem 1986;58:955–66.
[112] El Gabaly F, Grass M, McDaniel AH, Farrow RL, Linne MA, Hussain Z, et al. Measuring individual overpotentials in an operating solid-oxide electrochemical cell. PCCP 2010;12:12138–45.
[113] Greiner MT, Helander MG, Tang W-M, Wang Z-B, Qiu J, Lu Z-H. Universal energy-level alignment of molecules on metal oxides. Nat Mater 2012;11:76–81.
[114] Pan C, Ma T. Work function of In2O3 film as determined from internal photoemission. Appl Phys Lett 1980;37:714–6.
[115] Viskadourakis Z, Paramês M, Conde O, Zervos M, Giapintzakis J. Very high thermoelectric power factor in a Fe3O4/SiO2/p-type Si (100) heterostructure. Appl Phys Lett 2012;101:033505.
[116] Chen F, Schafranek R, Wu W, Klein A. Reduction-induced Fermi level pinning at the interfaces between Pb (Zr, Ti) O3 and Pt, Cu and Ag metal electrodes. J Phys D Appl Phys 2011;44:255301.
[117] Nandakumar NK, Seebauer EG. Relating catalytic activity of d0 semiconducting metal oxides to the fermi level position. J Phys Chem C 2014;118:6873–81.
[118] Henrich VE, Cox PA. The surface science of metal oxides. Cambridge University Press; 1996.
[119] Scanlon DO, Watson GW, Payne D, Atkinson G, Egdell R, Law D. Theoretical and experimental study of the electronic structures of MoO3 and MoO2. J Phys Chem C 2010;114:4636–45.
[120] Kröger M, Hamwi S, Meyer J, Riedl T, Kowalsky W, Kahn A. Role of the deep-lying electronic states of MoO 3 in the enhancement of hole-injection in organic thin films. Appl Phys Lett 2009;95:251.
[121] Meyer J, Kröger M, Hamwi S, Gnam F, Riedl T, Kowalsky W, et al. Charge generation layers comprising transition metal-oxide/organic interfaces: Electronic structure and charge generation mechanism. Appl Phys Lett 2010;96:93.
[122] Gordy W, Thomas WO. Electronegativities of the elements. J Chem Phys 1956;24:439–44.
[123] Mulliken RS. A new electroaffinity scale; together with data on valence states and on valence ionization potentials and electron affinities. J Chem Phys 1934;2:782–93.
[124] Mulliken RS. Electronic structures of molecules XI. Electroaffinity, molecular orbitals and dipole moments. J Chem Phys 1935;3:573–85.
[125] Neamen D. semiconductors physics and Devices, copyright©. McGraw Hill Compnies, Inc; 2003.
[126] Nethercot Jr AH. Prediction of Fermi energies and photoelectric thresholds based on electronegativity concepts. Phys Rev Lett 1974;33:1088.
[127] Michaelson HB. Work functions of the elements. J Appl Phys 1950;21:536–40.
[128] Conway B, Bockris JOM. Electrolytic hydrogen evolution kinetics and its relation to the electronic and adsorptive properties of the metal. J Chem Phys 1957;26:532–41.
[129] Miedema A, De Boer F, De Chatel P. Empirical description of the role of electronegativity in alloy formation. J Phys F 1973;3:1558.
[130] Chen EC, Wentworth W, Ayala J. The relationship between the Mulliken electronegativities of the elements and the work functions of metals and nonmetals. J Chem Phys 1977;67:2642–7.
[131] Michaelson HB. Relation between an atomic electronegativity scale and the work function. IBM J Res Dev 1978;22:72–80.
[132] Yamamoto S. Fundamental physics of vacuum electron sources. Rep Prog Phys 2005;69:181.
[133] Clementi E, Raimondi D-L. Atomic screening constants from SCF functions. J Chem Phys 1963;38:2686–9.
[134] Oxtoby DW, Gillis HP, Butler LJ. Principles of modern chemistry. Cengage AU 2016.
[135] Lu X, Wang G, Zhai T, Yu M, Gan J, Tong Y, et al. Hydrogenated TiO2 nanotube arrays for supercapacitors. Nano Lett 2012;12:1690–6.
[136] Zhou H, Zhang Y. Electrochemically self-doped TiO2 nanotube arrays for supercapacitors. J Phys Chem C 2014;118:5626–36.
[137] Kashiwaya S, Morasch J, Streibel V, Toupance T, Jaegermann W, Klein A. The work function of TiO2. Surfaces 2018;1:73–89.
[138] Wang Y, Xiao X, Xue H, Pang H. Zinc oxide based composite materials for advanced supercapacitors. ChemistrySelect 2018;3:550–65.
[139] Du X, Wang S, Liu Y, Lu M, Wu K, Lu M. Self-assembly of free-standing hybrid film based on graphene and zinc oxide nanoflakes for high-performance supercapacitors. J Solid State Chem 2019;277:441–7.
[140] Moormann H, Kohl D, Heiland G. Work function and band bending on clean cleaved zinc oxide surfaces. Surf Sci 1979;80:261–4.
[141] Schultz T, Frey NC, Hantanasirisakul K, Park S, May SJ, Shenoy VB, et al. Surface termination dependent work function and electronic properties of Ti3C2T x MXene. Chem Mater 2019;31:6590–7.
[142] Khazaei M, Arai M, Sasaki T, Ranjbar A, Liang Y, Yunoki S. OH-terminated two-dimensional transition metal carbides and nitrides as ultralow work function materials. Phys Rev B 2015;92:075411.
[143] Zhan C, Naguib M, Lukatskaya M, Kent PR, Gogotsi Y, Jiang D-e. Understanding the MXene pseudocapacitance. J Phys Chem Lett 2018;9:1223–8.
[144] Lin Y-J, Baikie ID, Chou W-Y, Lin S-T, Chang H-C, Chen Y-M, et al. Changes in surface roughness and work function of indium-tin-oxide due to KrF excimer laser irradiation. J Vac Sci Technol A 2005;23:1305–8.
[145] Ryu I, Yang M, Kwon H, Park HK, Do YR, Lee SB, et al. Coaxial RuO2–ITO nanopillars for transparent supercapacitor application. Langmuir 2014;30:1704–9.
[146] Zhang CJ, Nicolosi V. Graphene and MXene-based transparent conductive electrodes and supercapacitors. Energy Storage Mater 2019;16:102–25.

[147] Li W, Li D. Influence of surface morphology on corrosion and electronic behavior. Acta Mater 2006;54:445–52.
[148] Henderson MA. The interaction of water with solid surfaces: fundamental aspects revisited. Surf Sci Rep 2002;46:1–308.
[149] Thiel PA, Madey TE. The interaction of water with solid surfaces: Fundamental aspects. Surf Sci Rep 1987;7:211–385.
[150] Hagstrum HD. Effect of monolayer adsorption on the ejection of electrons from metals by ions. Phys Rev 1956;104:1516.
[151] Muscat J, Batra IP. Coverage dependence of the work function of metals upon alkali-metal adsorption. Phys Rev B 1986;34:2889.
[152] Besocke K, Wagner H. Adsorption of W on W (110): Work-function reduction and island formation. Phys Rev B 1973;8:4597.
[153] Trasatti S. Structure of the metal/electrolyte solution interface: new data for theory. Electrochim Acta 1991;36:1659–67.
[154] Trasatti S. The electrode potential. Comprehensive Treatise of Electrochemistry: Springer; 1980. p. 45-81.
[155] Bockris JOM, Potter E. The mechanism of hydrogen evolution at nickel cathodes in aqueous solutions. J Chem Phys 1952;20:614–28.
[156] Debye P. Polar molecules, the chemical catalog company. Inc, New York. 1929:77-108.
[157] Onsager L. Electric moments of molecules in liquids. J Am Chem Soc 1936;58:1486–93.
[158] Kirkwood JG. The dielectric polarization of polar liquids. J Chem Phys 1939;7:911–9.
[159] Kaur J, Kant R. Theory of work function and potential of zero charge for metal nanostructured and rough electrodes. J Phys Chem C 2017;121:13059–69.
[160] Tokarz-Sobieraj R, Hermann K, Witko M, Blume A, Mestl G, Schlögl R. Properties of oxygen sites at the MoO3 (0 1 0) surface: density functional theory cluster studies and photoemission experiments. Surf Sci 2001;489:107–25.
[161] Young MJ, Holder AM, George SM, Musgrave CB. Charge storage in cation incorporated α-MnO2. Chem Mater 2015;27:1172–80.
[162] Yin B, Zhang S, Jiang H, Qu F, Wu X. Phase-controlled synthesis of polymorphic MnO 2 structures for electrochemical energy storage. J Mater Chem A 2015;3:5722–9.
[163] Thackeray MM. Manganese oxides for lithium batteries. Prog Solid State Chem 1997;25:1–71.
[164] Feng Q, Yanagisawa K, Yamasaki N. Hydrothermal soft chemical process for synthesis of manganese oxides with tunnel structures. J Porous Mater 1998;5:153–62.
[165] Wu N, Bai X, Pan D, Dong B, Wei R, Naik N, et al. Recent advances of asymmetric supercapacitors. Adv Mater Interfaces 2021;8:2001710.
[166] Chodankar NR, Dubal DP, Lokhande AC, Patil AM, Kim JH, Lokhande CD. An innovative concept of use of redox-active electrolyte in asymmetric capacitor based on MWCNTs/MnO2 and Fe2O3 thin films. Sci Rep 2016:6.
[167] Singh A, Chandra A. Enhancing Specific Energy and Power in Asymmetric Supercapacitors - A Synergetic Strategy based on the Use of Redox Additive Electrolytes. Sci Rep 2016:6.
[168] Kumar KS, Pandey D, Thomas J. High voltage asymmetric supercapacitors developed by engineering electrode work functions. ACS Energy Lett 2021;6:3590–9.
[169] Wei W, Cui X, Chen W, Ivey DG. Manganese oxide-based materials as electrochemical supercapacitor electrodes. Chem Soc Rev 2011;40:1697–721.
[170] Liu Y, Luo D, Shi K, Michaud X, Zhitomirsky I. Asymmetric supercapacitor based on MnO2 and Fe2O3 nanotube active materials and graphene current collectors. Nano-Struct Nano-Objects 2018;15:98–106.
[171] Lu X, Zeng Y, Yu M, Zhai T, Liang C, Xie S, et al. Oxygen-deficient hematite nanorods as high-performance and novel negative electrodes for flexible asymmetric supercapacitors. Adv Mater 2014;26:3148–55.
[172] Yang P, Ding Y, Lin Z, Chen Z, Li Y, Qiang P, et al. Low-cost high-performance solid-state asymmetric supercapacitors based on MnO2 nanowires and Fe2O3 nanotubes. Nano Lett 2014;14:731–6.
[173] Xia H, Hong C, Li B, Zhao B, Lin Z, Zheng M, et al. Facile synthesis of hematite quantum-dot/functionalized graphene-sheet composites as advanced anode materials for asymmetric supercapacitors. Adv Funct Mater 2015;25:627–35.
[174] Chodankar NR, Dubal DP, Gund GS, Lokhande CD. Bendable all-solid-state asymmetric supercapacitors based on MnO2 and Fe2O3 thin films. Energ Technol 2015;3:625–31.
[175] Gund GS, Dubal DP, Chodankar NR, Cho JY, Gomez-Romero P, Park C, et al. Low-cost flexible supercapacitors with high-energy density based on nanostructured MnO 2 and Fe 2 O 3 thin films directly fabricated onto stainless steel. Sci Rep-Uk 2015;5:12454.
[176] Zhou Z, Zhang Q, Sun J, He B, Guo J, Li Q, et al. Metal–organic framework derived spindle-like carbon incorporated α-Fe2O3 grown on carbon nanotube fiber as anodes for high-performance wearable asymmetric supercapacitors. ACS Nano 2018;12:9333–41.
[177] Li Y, Xu J, Feng T, Yao Q, Xie J, Xia H. Fe2O3 nanoneedles on ultrafine nickel nanotube arrays as efficient anode for high-performance asymmetric supercapacitors. Adv Funct Mater 2017;27:1606728.
[178] Hu Y, Guan C, Ke Q, Yow ZF, Cheng C, Wang J. Hybrid Fe2O3 nanoparticle clusters/rGO paper as an effective negative electrode for flexible supercapacitors. Chem Mater 2016;28:7296–303.
[179] Liang H, Xia C, Emwas A-H, Anjum DH, Miao X, Alshareef HN. Phosphine plasma activation of α-Fe2O3 for high energy asymmetric supercapacitors. Nano Energy 2018;49:155–62.
[180] Jia R, Zhu F, Sun S, Zhai T, Xia H. Dual support ensuring high-energy supercapacitors via high-performance NiCo2S4@ Fe2O3 anode and working potential enlarged MnO2 cathode. J Power Sources 2017;341:427–34.
[181] Nithya V, Arul NS. Progress and development of Fe 3 O 4 electrodes for supercapacitors. J Mater Chem A 2016;4:10767–78.
[182] Cottineau T, Toupin M, Delahaye T, Brousse T, Bélanger D. Nanostructured transition metal oxides for aqueous hybrid electrochemical supercapacitors. Appl Phys A 2006;82:599–606.
[183] Sun J, Huang Y, Fu C, Huang Y, Zhu M, Tao X, et al. A high performance fiber-shaped PEDOT@ MnO 2//C@ Fe 3 O 4 asymmetric supercapacitor for wearable electronics. J Mater Chem A 2016;4:14877–83.
[184] Yang J, Xiao X, Chen P, Zhu K, Cheng K, Ye K, et al. Creating oxygen-vacancies in MoO3-x nanobelts toward high volumetric energy-density asymmetric supercapacitors with long lifespan. Nano Energy 2019;58:455–65.
[185] Yu M, Cheng X, Zeng Y, Wang Z, Tong Y, Lu X, et al. Dual-doped molybdenum trioxide nanowires: a bifunctional anode for fiber-shaped asymmetric supercapacitors and microbial fuel cells. Angew Chem 2016;128:6874–8.
[186] Ma W, Chen S, Yang S, Chen W, Weng W, Cheng Y, et al. Flexible all-solid-state asymmetric supercapacitor based on transition metal oxide nanorods/reduced graphene oxide hybrid fibers with high energy density. Carbon 2017;113:151–8.
[187] Lee TH, Pham DT, Sahoo R, Seok J, Luu THT, Lee YH. High energy density and enhanced stability of asymmetric supercapacitors with mesoporous MnO2@ CNT and nanodot MoO3@ CNT free-standing films. Energy Storage Mater 2018;12:223–31.
[188] Noh J, Yoon C-M, Kim YK, Jang J. High performance asymmetric supercapacitor twisted from carbon fiber/MnO2 and carbon fiber/MoO3. Carbon 2017;116:470–8.
[189] Sawangphruk M, Srimuk P, Chiochan P, Krittayavathananon A, Luanwuthi S, Limtrakul J. High-performance supercapacitor of manganese oxide/reduced graphene oxide nanocomposite coated on flexible carbon fiber paper. Carbon 2013;60:109–16.
[190] Thangappan R, Arivanandhan M, Kalaiselvam S, Jayavel R, Hayakawa Y. Molybdenum oxide/graphene nanocomposite electrodes with enhanced capacitive performance for supercapacitor applications. J Inorg Organomet Polym Mater 2018;28:50–62.
[191] Chen Z, Qin Y, Weng D, Xiao Q, Peng Y, Wang X, et al. Design and synthesis of hierarchical nanowire composites for electrochemical energy storage. Adv Funct Mater 2009;19:3420–6.
[192] Zhai T, Lu X, Ling Y, Yu M, Wang G, Liu T, et al. A new benchmark capacitance for supercapacitor anodes by mixed-valence sulfur-doped V6O13− x. Adv Mater 2014;26:5869–75.
[193] Liu W, Liu N, Shi Y, Chen Y, Yang C, Tao J, et al. A wire-shaped flexible asymmetric supercapacitor based on carbon fiber coated with a metal oxide and a polymer. J Mater Chem A 2015;3:13461–7.
[194] Wang W, Xiao Y, Li X, Cheng Q, Wang G. Bismuth oxide self-standing anodes with concomitant carbon dots welded graphene layer for enhanced performance supercapacitor-battery hybrid devices. Chem Eng J 2019;371:327–36.

[195] Xu H, Hu X, Yang H, Sun Y, Hu C, Huang Y. Flexible asymmetric micro-supercapacitors based on Bi2O3 and MnO2 nanoflowers: Larger areal mass promises higher energy density. Adv Energy Mater 2015;5:1401882.
[196] Subramani K, Kowsik S, Sathish M. Facile and scalable ultra–fine cobalt oxide/reduced graphene oxide nanocomposites for high energy asymmetric supercapacitors. ChemistrySelect 2016;1:3455–67.
[197] Xu W, Chen J, Yu M, Zeng Y, Long Y, Lu X, et al. Sulphur-doped Co 3 O 4 nanowires as an advanced negative electrode for high-energy asymmetric supercapacitors. J Mater Chem A 2016;4:10779–85.
[198] Shinde PA, Chodankar NR, Lokhande VC, Patil AM, Ji T, Kim JH, et al. Fabrication of high performance flexible all-solid-state asymmetric supercapacitors with a three dimensional disc-like WO 3/stainless steel electrode. Rsc Adv 2016;6:113442–51.
[199] Sahoo R, Pham DT, Lee TH, Luu THT, Seok J, Lee YH. Redox-driven route for widening voltage window in asymmetric supercapacitor. ACS Nano 2018;12:8494–505.
[200] Julien CM, Mauger A. Nanostructured MnO2 as electrode materials for energy storage. Nanomaterials-Basel 2017;7:396.
[201] Sambath Kumar K, Choudhary N, Pandey D, Ding Y, Hurtado L, Chung H-S, et al. Investigating 2D WS2 supercapacitor electrode performance by Kelvin Probe Force Microscopy. J Mater Chem A 2020.
[202] Jabeen N, Hussain A, Xia Q, Sun S, Zhu J, Xia H. High-performance 2.6 V aqueous asymmetric supercapacitors based on in situ formed Na0. 5MnO2 nanosheet assembled nanowall arrays. Adv Mater 2017;29.
[203] Singh A, Chandra A. Significant performance enhancement in asymmetric supercapacitors based on metal oxides, carbon nanotubes and neutral aqueous electrolyte. Sci Rep-Uk 2015;5:15551.
[204] Yang C, Sun M, Lu H. Asymmetric all-metal-oxide supercapacitor with superb cycle performance. Chemistry–A. European Journal 2018;24:6169–77.
[205] Liu ZH, Tian XC, Xu X, He L, Yan MY, Han CH, et al. Capacitance and voltage matching between MnO2 nanoflake cathode and Fe2O3 nanoparticle anode for high-performance asymmetric micro-supercapacitors. Nano Res 2017;10:2471–81.
[206] Zeng Y, Han Y, Zhao Y, Zeng Y, Yu M, Liu Y, et al. Advanced Ti-doped Fe2O3@ PEDOT core/shell anode for high-energy asymmetric Supercapacitors. Adv Energy Mater 2015;5:1402176.
[207] Yu Z, Moore J, Calderon J, Zhai L, Thomas J. Coil-Type Asymmetric Supercapacitor Electrical Cables. Small 2015;11:5289–95.
[208] Chodankar NR, Dubal DP, Lokhande AC, Patil AM, Kim JH, Lokhande CD. An innovative concept of use of redox-active electrolyte in asymmetric capacitor based on MWCNTs/MnO 2 and Fe 2 O 3 thin films. Sci Rep-Uk 2016;6:1–14.
[209] Gu T, Wei B. High-performance all-solid-state asymmetric stretchable supercapacitors based on wrinkled MnO 2/CNT and Fe 2 O 3/CNT macrofilms. J Mater Chem A 2016;4:12289–95.
[210] Singh A, Chandra A. Enhancing specific energy and power in asymmetric supercapacitors-a synergetic strategy based on the use of redox additive electrolytes. Sci Rep-Uk 2016;6:25793.
[211] Béguin F, Presser V, Balducci A, Frackowiak E. Carbons and electrolytes for advanced supercapacitors. Adv Mater 2014;26:2219–51.
[212] Zhu Y, Murali S, Stoller MD, Ganesh K, Cai W, Ferreira PJ, et al. Carbon-based supercapacitors produced by activation of graphene. Science 2011;332:1537–41.
[213] Wang Q, Yan J, Wang Y, Wei T, Zhang M, Jing X, et al. Three-dimensional flower-like and hierarchical porous carbon materials as high-rate performance electrodes for supercapacitors. Carbon 2014;67:119–27.
[214] He T, Meng X, Nie J, Tong Y, Cai K. Thermally reduced graphene oxide electrochemically activated by bis-spiro quaternary alkyl ammonium for capacitors. ACS Appl Mater Interfaces 2016;8:13865–70.
[215] Lian C, Liu K, Van Aken KL, Gogotsi Y, Wesolowski DJ, Liu H, et al. Enhancing the capacitive performance of electric double-layer capacitors with ionic liquid mixtures. ACS Energy Lett 2016;1:21–6.
[216] Radovic LR. Chemistry & Physics Of Carbon:, Volume 29. CRC Press; 2004.
[217] Oliveira NCd. Deposição de filmes de óxido de grafeno mediada por íons de metais de transição. 2017.
[218] Ishimoto S, Asakawa Y, Shinya M, Naoi K. Degradation responses of activated-carbon-based EDLCs for higher voltage operation and their factors. J Electrochem Soc 2009;156:A563.
[219] Morimoto T, Hiratsuka K, Sanada Y, Kurihara K. Electric double-layer capacitor using organic electrolyte. J Power Sources 1996;60:239–47.
[220] Yoshida A, Tanahashi I, Nishino A. Effect of concentration of surface acidic functional groups on electric double-layer properties of activated carbon fibers. Carbon 1990;28:611–5.
[221] Ju YT, Cho M-Y, Kim M-H, Lee J-W, Park S-M, Choi BH, et al. The reduction effect of oxygen functional groups in activated carbon for supercapacitor electrode. J Ceram Process Res 2012;13:S159–62.
[222] Li X-r, Jiang Y-h, Wang P-z, Mo Y, Li Z-j, Yu R-j, et al. Effect of the oxygen functional groups of activated carbon on its electrochemical performance for supercapacitors. New Carbon Mater 2020; 35: 232–43.
[223] Wertheimer M, Klemberg-Sapieha J, Cerny J, Liang S. Modification of active carbon by hydrophobic plasma polymers: II fabric substrates. Plasma Polym 1998;3:151–63.
[224] Fang B, Binder L. A novel carbon electrode material for highly improved EDLC performance. J Phys Chem B 2006;110:7877–82.
[225] Cosnier F, Celzard A, Furdin G, Begin D, Marêché J, Barres O. Hydrophobisation of active carbon surface and effect on the adsorption of water. Carbon 2005;43:2554–63.
[226] Derouet D, Forgeard S, Brosse JC, Emery J, Buzare JY. Application of solid-state NMR (13C and 29Si CP/MAS NMR) spectroscopy to the characterization of alkenyltrialkoxysilane and trialkoxysilyl-terminated polyisoprene grafting onto silica microparticles. J Polym Sci A Polym Chem 1998;36:437–53.
[227] Yoshida W, Castro RP, Jou J-D, Cohen Y. Multilayer alkoxysilane silylation of oxide surfaces. Langmuir 2001;17:5882–8.
[228] Budarin VL, Clark JH, Mikhalovsky SV, Gorlova AA, Boldyreva NA, Yatsimirsky VK. The hydrophobisation of activated carbon surfaces by organic functional groups. Adsorpt Sci Technol 2000;18:55–64.
[229] Yang M, Zhou Z. Recent breakthroughs in supercapacitors boosted by nitrogen-rich porous carbon materials. Adv Sci 2017;4:1600408.
[230] Bleda-Martínez MJ, Maciá-Agulló JA, Lozano-Castelló D, Morallon E, Cazorla-Amorós D, Linares-Solano A. Role of surface chemistry on electric double layer capacitance of carbon materials. Carbon 2005;43:2677–84.
[231] Panchakarla L, Subrahmanyam K, Saha S, Govindaraj A, Krishnamurthy H, Waghmare U, et al. Synthesis, structure, and properties of boron-and nitrogen-doped graphene. Adv Mater 2009;21:4726–30.
[232] Hasegawa G, Deguchi T, Kanamori K, Kobayashi Y, Kageyama H, Abe T, et al. High-level doping of nitrogen, phosphorus, and sulfur into activated carbon monoliths and their electrochemical capacitances. Chem Mater 2015;27:4703–12.
[233] Chi Y-W, Hu C-C, Shen H-H, Huang K-P. New approach for high-voltage electrical double-layer capacitors using vertical graphene nanowalls with and without nitrogen doping. Nano Lett 2016;16:5719–27.
[234] Shiraishi S. Heat-treatment and nitrogen-doping of activated carbons for high voltage operation of electric double layer capacitor. Key Engineering Materials: Trans Tech Publ; 2012. p. 80-6.
[235] Salinas-Torres D, Shiraishi S, Morallón E, Cazorla-Amorós D. Improvement of carbon materials performance by nitrogen functional groups in electrochemical capacitors in organic electrolyte at severe conditions. Carbon 2015;82:205–13.
[236] Wang X, Liu C-G, Neff D, Fulvio PF, Mayes RT, Zhamu A, et al. Nitrogen-enriched ordered mesoporous carbons through direct pyrolysis in ammonia with enhanced capacitive performance. J Mater Chem A 2013;1:7920–6.
[237] Seredych M, Hulicova-Jurcakova D, Lu GQ, Bandosz TJ. Surface functional groups of carbons and the effects of their chemical character, density and accessibility to ions on electrochemical performance. Carbon 2008;46:1475–88.
[238] Kwon T, Nishihara H, Itoi H, Yang Q-H, Kyotani T. Enhancement mechanism of electrochemical capacitance in nitrogen-/boron-doped carbons with uniform straight nanochannels. Langmuir 2009;25:11961–8.
[239] Candelaria SL, Garcia BB, Liu D, Cao G. Nitrogen modification of highly porous carbon for improved supercapacitor performance. J Mater Chem 2012;22:9884–9.

[240] Ornelas O, Sieben JM, Ruiz-Rosas R, Morallon E, Cazorla-Amorós D, Geng J, et al. On the origin of the high capacitance of nitrogen-containing carbon nanotubes in acidic and alkaline electrolytes. Chem Commun 2014;50:11343–6.
[241] Pinkert K, Oschatz M, Borchardt L, Klose M, Zier M, Nickel W, et al. Role of surface functional groups in ordered mesoporous carbide-derived carbon/ionic liquid electrolyte double-layer capacitor interfaces. ACS Appl Mater Interfaces 2014;6:2922–8.
[242] Kim M-H, Yang J-H, Kang Y-M, Park S-M, Han JT, Kim K-B, et al. Fluorinated activated carbon with superb kinetics for the supercapacitor application in nonaqueous electrolyte. Colloids Surf A Physicochem Eng Asp 2014;443:535–9.
[243] Ruch P, Cericola D, Foelske A, Kötz R, Wokaun A. A comparison of the aging of electrochemical double layer capacitors with acetonitrile and propylene carbonate-based electrolytes at elevated voltages. Electrochim Acta 2010;55:2352–7.
[244] Zhu M, Weber C, Yang Y, Konuma M, Starke U, Kern K, et al. Chemical and electrochemical ageing of carbon materials used in supercapacitor electrodes. Carbon 2008;46:1829–40.
[245] Shen H-H, Hu C-C. Capacitance enhancement of activated carbon modified in the propylene carbonate electrolyte. J Electrochem Soc 2014;161:A1828.
[246] Michan AL, Parimalam BS, Leskes M, Kerber RN, Yoon T, Grey CP, et al. Fluoroethylene carbonate and vinylene carbonate reduction: understanding lithium-ion battery electrolyte additives and solid electrolyte interphase formation. Chem Mater 2016;28:8149–59.
[247] Xu C, Lindgren F, Philippe B, Gorgoi M, Björefors F, Edström K, et al. Improved performance of the silicon anode for Li-ion batteries: understanding the surface modification mechanism of fluoroethylene carbonate as an effective electrolyte additive. Chem Mater 2015;27:2591–9.
[248] Aurbach D, Markovsky B, Shechter A, Ein-Eli Y, Cohen H. A comparative study of synthetic graphite and Li electrodes in electrolyte solutions based on ethylene carbonate-dimethyl carbonate mixtures. J Electrochem Soc 1996;143:3809.
[249] Boltersdorf J, Delp SA, Yan J, Cao B, Zheng JP, Jow TR, et al. Electrochemical performance of lithium-ion capacitors evaluated under high temperature and high voltage stress using redox stable electrolytes and additives. J Power Sources 2018;373:20–30.
[250] Delp SA, Borodin O, Olguin M, Eisner CG, Allen JL, Jow TR. Importance of reduction and oxidation stability of high voltage electrolytes and additives. Electrochim Acta 2016;209:498–510.
[251] Rong H, Xu M, Xing L, Li W. Enhanced cyclability of LiNi0. 5Mn1. 5O4 cathode in carbonate based electrolyte with incorporation of tris (trimethylsilyl) phosphate (TMSP). J Power Sources 2014;261:148–55.
[252] Yan G, Li X, Wang Z, Guo H, Wang C. Tris (trimethylsilyl) phosphate: a film-forming additive for high voltage cathode material in lithium-ion batteries. J Power Sources 2014;248:1306–11.
[253] Zhang J, Wang J, Yang J, NuLi Y. Artificial interface deriving from sacrificial tris (trimethylsilyl) phosphate additive for lithium rich cathode materials. Electrochim Acta 2014;117:99–104.
[254] Wang Y, Xing L, Borodin O, Huang W, Xu M, Li X, et al. Quantum chemistry study of the oxidation-induced stability and decomposition of propylene carbonate-containing complexes. PCCP 2014;16:6560–7.
[255] Li M, Westover AS, Carter R, Oakes L, Muralidharan N, Boire TC, et al. Noncovalent pi–pi stacking at the carbon–electrolyte interface: controlling the voltage window of electrochemical supercapacitors. ACS Appl Mater Interfaces 2016;8:19558–66.
[256] Liu R, Wan L, Liu S, Pan L, Wu D, Zhao D. An interface-induced Co-assembly approach towards ordered mesoporous carbon/graphene aerogel for high-performance supercapacitors. Adv Funct Mater 2015;25:526–33.
[257] Wang H, Pilon L. Accurate simulations of electric double layer capacitance of ultramicroelectrodes. J Phys Chem C 2011;115:16711–9.
[258] Pilon L, Wang H, d'Entremont A. Recent advances in continuum modeling of interfacial and transport phenomena in electric double layer capacitors. J Electrochem Soc 2015;162:A5158.
[259] Chen Y, Qing L, Liu T, Zhao S, Han Y. Tuning interfacial ion distribution to improve energy density of supercapacitors. Nano Energy 2022;102:107660.
[260] Qing L, Li Y, Tang W, Zhang D, Han Y, Zhao S. Dynamic adsorption of ions into like-charged nanospace: a dynamic density functional theory study. Langmuir 2019;35:4254–62.
[261] Wu D, Zhang WY, Feng HJ, Zhang ZJ, Chen XY, Cui P. Mechanistic insights into the intermolecular interaction and Li+ solvation structure in small-molecule crowding electrolytes for high-voltage aqueous supercapacitors. ACS Applied Energy Materials 2022;5:12067–77.
[262] Wu D, Feng HJ, Xu LH, Zhang WY, Zhang ZJ, Chen XY, et al. Optimal design of a small-molecule crowding electrolyte and molecular dynamics simulation of an electrode–electrolyte interface for aqueous supercapacitors with a wide operating temperature range. ACS Applied Energy Materials 2022;5:355–66.
[263] Morita M, Arizono R, Yoshimoto N, Egashira M. On the electrochemical activation of alkali-treated soft carbon for advanced electrochemical capacitors. J Appl Electrochem 2014;44:447–53.
[264] Shen H-H, Hu C-C. A high-voltage asymmetric electrical double-layer capacitors using propylene carbonate. Electrochem Commun 2016;70:23–7.
[265] Kim I-T, Egashira M, Yoshimoto N, Morita M. Combination of alkali-treated soft carbon and activated carbon fiber electrodes for asymmetric electric double-layer capacitor. Electrochemistry 2012;80:415–20.
[266] Liu C-F, Liu Y-C, Yi T-Y, Hu C-C. Carbon materials for high-voltage supercapacitors. Carbon 2019;145:529–48.
[267] Rajkumar M, Hsu C-T, Wu T-H, Chen M-G, Hu C-C. Advanced materials for aqueous supercapacitors in the asymmetric design. Prog Nat Sci: Mater Int 2015;25:527–44.
[268] Wang H, Zhu C, Chao D, Yan Q, Fan HJ. Nonaqueous hybrid lithium-ion and sodium-ion capacitors. Adv Mater 2017;29:1702093.
[269] Zhang F, Zhang T, Yang X, Zhang L, Leng K, Huang Y, et al. A high-performance supercapacitor-battery hybrid energy storage device based on graphene-enhanced electrode materials with ultrahigh energy density. Energ Environ Sci 2013;6:1623–32.
[270] Naoi K, Simon P. New materials and new configurations for advanced electrochemical capacitors. Electrochem Soc Interface 2008;17:34.
[271] He Y-B, Li B, Liu M, Zhang C, Lv W, Yang C, et al. Gassing in Li 4 Ti 5 O 12-based batteries and its remedy. Sci Rep 2012;2:1–9.
[272] Aida T, Murayama I, Yamada K, Morita M. High-energy-density hybrid electrochemical capacitor using graphitizable carbon activated with KOH for positive electrode. J Power Sources 2007;166:462–70.
[273] Cao W, Zheng J. The effect of cathode and anode potentials on the cycling performance of Li-ion capacitors. J Electrochem Soc 2013;160:A1572.
[274] Zhong C, Deng Y, Hu W, Qiao J, Zhang L, Zhang J. A review of electrolyte materials and compositions for electrochemical supercapacitors. Chem Soc Rev 2015;44:7484–539.
[275] Huang J, Yuan K, Chen Y. Wide voltage aqueous asymmetric supercapacitors: advances, strategies, and challenges. Adv Funct Mater 2022;32:2108107.
[276] Abbas Q, Ratajczak P, Babuchowska P, Le Comte A, Bélanger D, Brousse T, et al. Strategies to improve the performance of carbon/carbon capacitors in salt aqueous electrolytes. J Electrochem Soc 2015;162:A5148.
[277] Bichat M, Raymundo-Piñero E, Béguin F. High voltage supercapacitor built with seaweed carbons in neutral aqueous electrolyte. Carbon 2010;48:4351–61.
[278] Gao Q, Demarconnay L, Raymundo-Piñero E, Béguin F. Exploring the large voltage range of carbon/carbon supercapacitors in aqueous lithium sulfate electrolyte. Energ Environ Sci 2012;5:9611–7.
[279] Fic K, Lota G, Meller M, Frackowiak E. Novel insight into neutral medium as electrolyte for high-voltage supercapacitors. Energ Environ Sci 2012;5:5842–50.
[280] Lin T, Chen I-W, Liu F, Yang C, Bi H, Xu F, et al. Nitrogen-doped mesoporous carbon of extraordinary capacitance for electrochemical energy storage. Science 2015;350:1508–13.
[281] Pohlmann S, Ramirez-Castro C, Balducci A. The influence of conductive salt ion selection on EDLC electrolyte characteristics and carbon-electrolyte interaction. J Electrochem Soc 2015;162:A5020.
[282] Péan C, Daffos B, Merlet C, Rotenberg B, Taberna P-L, Simon P, et al. Single electrode capacitances of porous carbons in neat ionic liquid electrolyte at 100 C: a combined experimental and modeling approach. J Electrochem Soc 2015;162:A5091.
[283] Sillars FB, Fletcher SI, Mirzaeian M, Hall PJ. Variation of electrochemical capacitor performance with room temperature ionic liquid electrolyte viscosity and ion size. Phys Chem Chem Phys 2012;14:6094–100.
[284] Watanabe M, Thomas ML, Zhang S, Ueno K, Yasuda T, Dokko K. Application of ionic liquids to energy storage and conversion materials and devices. Chem Rev 2017;117:7190–239.
[285] Goodenough JB, Kim Y. Challenges for rechargeable Li batteries. Chem Mater 2010;22:587–603.

[286] Goodenough JB, Park K-S. The Li-ion rechargeable battery: a perspective. J Am Chem Soc 2013;135:1167–76.
[287] Long JW, Bélanger D, Brousse T, Sugimoto W, Sassin MB, Crosnier O. Asymmetric electrochemical capacitors—Stretching the limits of aqueous electrolytes. MRS Bull 2011;36:513–22.
[288] Shimizu W, Makino S, Takahashi K, Imanishi N, Sugimoto W. Development of a 4.2 V aqueous hybrid electrochemical capacitor based on MnO2 positive and protected Li negative electrodes. J Power Sources 2013;241:572–7.
[289] Peng C, Zhang S, Zhou X, Chen GZ. Unequalisation of electrode capacitances for enhanced energy capacity in asymmetrical supercapacitors. Energ Environ Sci 2010;3:1499–502.
[290] Chae J, Ng K, Chen G. Nanostructured materials for the construction of asymmetrical supercapacitors. Proc Instit Mech Eng, Part A: J Power Energy 2010;224:479–503.
[291] Bard AJ, Faulkner LR. Fundamentals and applications. Electrochemical methods. 2001;2:580-632.
[292] Laursen AB, Varela AS, Dionigi F, Fanchiu H, Miller C, Trinhammer OL, et al. Electrochemical hydrogen evolution: Sabatier's principle and the volcano plot. J Chem Educ 2012;89:1595–9.
[293] Lyon YA, Roberts AA, McMillin DR. Exploring hydrogen evolution and the overpotential. J Chem Educ 2015;92:2130–3.
[294] Wang W, Wei X, Choi D, Lu X, Yang G, Sun C. Electrochemical cells for medium-and large-scale energy storage: Fundamentals. Advances in batteries for medium and large-scale energy storage: Elsevier; 2015. p. 3-28.
[295] Covington AK, Bates R, Durst R. Definition of pH scales, standard reference values, measurement of pH and related terminology (Recommendations 1984). Pure Appl Chem 1985;57:531–42.
[296] Lee HY, Goodenough JB. Supercapacitor behavior with KCl electrolyte. J Solid State Chem 1999;144:220–3.
[297] Wen S, Lee J-W, Yeo I-H, Park J, Mho S-i. The role of cations of the electrolyte for the pseudocapacitive behavior of metal oxide electrodes, MnO2 and RuO2. Electrochim Acta 2004;50:849–55.
[298] Sun L, Tian C, Fu Y, Yang Y, Yin J, Wang L, et al. Nitrogen-doped porous graphitic carbon as an excellent electrode material for advanced supercapacitors. Chem Eur J 2014;20:564–74.
[299] Chun S-E, Whitacre J. Investigating the role of electrolyte acidity on hydrogen uptake in mesoporous activated carbons. J Power Sources 2013;242:137–40.
[300] Wen Y, Wang B, Huang C, Wang L, Hulicova-Jurcakova D. Synthesis of phosphorus-doped graphene and its wide potential window in aqueous supercapacitors. Chemistry–A. European Journal 2015;21:80–5.
[301] Bichat MP, Raymundo-Pinero E, Beguin F. High voltage supercapacitor built with seaweed carbons in neutral aqueous electrolyte. Carbon 2010;48:4351–61.
[302] Melchior SA, Raju K, Ike IS, Erasmus RM, Kabongo G, Sigalas I, et al. High-Voltage Symmetric Supercapacitor Based on 2D Titanium Carbide (MXene, Ti2CTx)/Carbon Nanosphere Composites in a Neutral Aqueous Electrolyte. J Electrochem Soc 2018;165:A501–11.
[303] Han L, Huang HL, Fu XB, Li JF, Yang ZL, Liu XJ, et al. A flexible, high-voltage and safe zwitterionic natural polymer hydrogel electrolyte for high-energy-density zinc-ion hybrid supercapacitor. Chem. Eng J 2020;392.
[304] Jiang MJ, Zhu JD, Chen C, Lu Y, Pampal ES, Luo L, et al. Superior high-voltage aqueous carbon/ carbon supercapacitors operating with in situ electrodeposited polyvinyl alcohol borate gel polymer electrolytes. J Mater Chem A 2016;4:16588–96.
[305] Liu TC, Sutarsis S, Zhong XY, Lin WC, Chou SH, Kirana N, et al. An interfacial wetting water based hydrogel electrolyte for high-voltage flexible quasi solid-state supercapacitors. Energy Storage Mater 2021;38:489–98.
[306] Batisse N, Raymundo-Pinero E. A self-standing hydrogel neutral electrolyte for high voltage and safe flexible supercapacitors. J Power Sources 2017;348:168–74.
[307] Li ZW, Gao S, Mi HY, Lei CC, Ji CC, Xie ZL, et al. High-energy quasi-solid-state supercapacitors enabled by carbon nanofoam from biowaste and high-voltage inorganic gel electrolyte. Carbon 2019;149:273–80.
[308] Wei J, Zhou J, Su S, Jiang J, Feng J, Wang Q. Water-deactivated polyelectrolyte hydrogel electrolytes for flexible high-voltage supercapacitors. ChemSusChem 2018;11:3410–5.
[309] Wei JJ, Yin CY, Wang HL, Wang QG. Polyampholyte-doped aligned polymer hydrogels as anisotropic electrolytes for ultrahigh-capacity supercapacitors. J Mater Chem A 2018;6:58–64.
[310] Peng X, Liu HL, Yin Q, Wu JC, Chen PZ, Zhang GZ, et al. A zwitterionic gel electrolyte for efficient solid-state supercapacitors. Nature. Communications 2016;7.
[311] Qiu F, Huang Y, He GG, Luo C, Li X, Wang MS, et al. A lignocellulose-based neutral hydrogel electrolyte for high-voltage supercapacitors with overlong cyclic stability. Electrochim Acta 2020;363.
[312] Lee WSV, Xiong T, Loh GC, Tan TL, Xue JM. Optimizing Electrolyte Physiochemical Properties toward 2.8 V Aqueous Supercapacitor. Acs Appl Energ Mater 2018;1:3070–6.
[313] Sennu P, Chua R, Dintakurti SSH, Hanna JV, Ramabhadran RO, Aravindan V, et al. Supersaturated "water-in-salt" hybrid electrolyte towards building high voltage Na-ion capacitors with wide temperatures operation. J Power Sources 2020;472.
[314] Wang WJ, Deng WJ, Wang XS, Li YB, Zhou ZQ, Hu ZX, et al. A hybrid superconcentrated electrolyte enables 2.5 V carbon-based supercapacitors. Chem Commun 2020;56:7965–8.
[315] Mahankali K, Thangavel NK, Ding Y, Putatunda SK, Arava LMR. Interfacial behavior of water-in-salt electrolytes at porous electrodes and its effect on supercapacitor performance. Electrochim Acta 2019;326.
[316] Tian ZY, Deng WJ, Wang XS, Liu CY, Li C, Chen JT, et al. Superconcentrated aqueous electrolyte to enhance energy density for advanced supercapacitors. Funct. Mater Lett 2017;10.
[317] Quan T, Hark E, Xu YL, Ahmet I, Hohn C, Mei SL, et al. Unveiling the Formation of Solid Electrolyte Interphase and its Temperature Dependence in "Water-in-Salt" Supercapacitors. ACS Appl Mater Interfaces 2021;13:3979–90.
[318] Xiao DW, Wu QH, Liu XL, Dou QY, Liu LY, Yang BJ, et al. Aqueous Symmetric Supercapacitors with Carbon Nanorod Electrodes and Water-in-Salt Electrolyte. ChemElectroChem 2019;6:439–43.
[319] Zhang M, Li YT, Shen ZR. "Water-in-salt" electrolyte enhanced high voltage aqueous supercapacitor with all-pseudocapacitive metal-oxide electrodes. J Power Sources 2019;414:479–85.
[320] Dou QY, Lu YL, Su LJ, Zhang X, Lei SL, Bu XD, et al. A sodium perchlorate-based hybrid electrolyte with high salt-to-water molar ratio for safe 2.5 V carbon-based supercapacitor. Energy Storage Mater 2019;23:603–9.
[321] Bu XD, Su LJ, Dou QY, Lei SL, Yan XB. A low-cost "water-in-salt" electrolyte for a 2.3 V high-rate carbon-based supercapacitor. J Mater Chem A 2019;7:7541–7.
[322] Pang MJ, Jiang S, Zhao JG, Zhang SF, Wang RW, Li N, et al. "Water-in-salt" electrolyte enhanced high voltage aqueous supercapacitor with carbon electrodes derived from biomass waste-ground grain hulls. RSC Adv 2020;10:35545–56.
[323] Thareja S, Kumar A, "Water-In-Salt",. Electrolyte-Based High-Voltage (2.7 V) Sustainable Symmetric Supercapacitor with Superb Electrochemical Performance-An Analysis of the Role of Electrolytic Ions in Extending the Cell Voltage. Acs Sustain Chem Eng 2021;9:2338–47.
[324] Deng YQ, Wang HF, Zhang KF, Shao JW, Qiu J, Wu J, et al. A high-voltage quasi-solid-state flexible supercapacitor with a wide operational temperature range based on a low-cost "water-in-salt" hydrogel electrolyte. Nanoscale 2021;13:3010–8.
[325] Pal B, Yang S, Ramesh S, Thangadurai V, Jose R. Electrolyte selection for supercapacitive devices: a critical review. Nanoscale Adv 2019;1:3807–35.
[326] Qiu X, Wang N, Wang Z, Wang F, Wang Y. Towards High-Performance Zinc-Based Hybrid Supercapacitors via Macropores-Based Charge Storage in Organic Electrolytes. Angew Chem Int Ed 2021;60:9610–7.
[327] Khosrozadeh A, Tao L, Zhao P, Miller MB, Voznyy O, Liu J. Water/acetonitrile hybrid electrolyte enables using smaller ions for achieving superior energy density in carbon-based supercapacitors. J Power Sources 2021;498:229905.
[328] Muzaffar A, Ahamed MB, Hussain CM. Electrolyte materials for supercapacitors. Smart Supercapacitors: Elsevier; 2023. p. 227–254.
[329] Yeletsky PM, Lebedeva MV, Yakovlev VA. Today's progress in the synthesis of porous carbons from biomass and their application for organic electrolyte and ionic liquid based supercapacitors. J Storage Mater 2022;50:104225.

[330] Lim JM, Jang YS, Nguyen HVT, Kim JS, Yoon Y, Park BJ, et al. Advances in high-voltage supercapacitors for energy storage systems: materials and electrolyte tailoring to implementation. Nanoscale Adv 2023;5:615–26.
[331] Mostazo-López MJ, Ruiz-Rosas R, Tagaya T, Hatakeyama Y, Shiraishi S, Morallón E, et al. Nitrogen doped superactivated carbons prepared at mild conditions as electrodes for supercapacitors in organic electrolyte. C 2020;6:56.
[332] Chen Z, Wang X, Ding Z, Wei Q, Wang Z, Yang X, et al. Biomass-based hierarchical porous carbon for supercapacitors: effect of aqueous and organic electrolytes on the electrochemical performance. ChemSusChem 2019;12:5099–110.
[333] Zhu J-J, Hemesh A, Biendicho JJ, Martinez-Soria L, Rueda-Garcia D, Morante JR, et al. Rational design of MXene/activated carbon/polyoxometalate triple hybrid electrodes with enhanced capacitance for organic-electrolyte supercapacitors. J Colloid Interface Sci 2022;623:947–61.
[334] Fernando N. A novel polyimide porous organic polymer for high energy supercapacitors.
[335] Beg YR, Nishad GR, Singh P. Organic Electrolytes for Flexible Supercapacitors. Flexible Supercapacitor Nanoarchitectonics 2021:143–75.
[336] Tran KT, Truong TT, Nguyen HV, Nguyen QD, Phung Q, Le PM, et al. Hybrid Deep Eutectic Solvent of LiTFSI-Ethylene Glycol Organic Electrolyte for Activated Carbon-Based Supercapacitors. J Chem 2021;2021:1–13.
[337] Zheng JP, Jow T. The effect of salt concentration in electrolytes on the maximum energy storage for double layer capacitors. J Electrochem Soc 1997;144:2417.
[338] Ue M, Ida K, Mori S. Electrochemical properties of organic liquid electrolytes based on quaternary onium salts for electrical double-layer capacitors. J Electrochem Soc 1994;141:2989.
[339] Ue M. Chemical capacitors and quaternary ammonium salts. Electrochemistry 2007;75:565–72.
[340] Yu X, Ruan D, Wu C, Wang J, Shi Z. Spiro-(1, 1′)-bipyrrolidinium tetrafluoroborate salt as high voltage electrolyte for electric double layer capacitors. J Power Sources 2014;265:309–16.
[341] Zheng C, Gao J, Yoshio M, Qi L, Wang H. Non-porous activated mesophase carbon microbeads as a negative electrode material for asymmetric electrochemical capacitors. J Power Sources 2013;231:29–33.
[342] Kurig H, Jänes A, Lust E. Substituted phosphonium cation based electrolytes for nonaqueous electrical double-layer capacitors. J Mater Res 2010;25:1447–50.
[343] Ebina T, Uno H, Ishizawa S, Nanbu N, Sasaki Y. Use of tetraethylammonium bis (oxalato) borate as electrolyte for electrical double-layer capacitors. Chem Lett 2005;34:1014–5.
[344] Nanbu N, Ebina T, Uno H, Ishizawa S, Sasaki Y. Physical and electrochemical properties of quaternary ammonium bis (oxalato) borates and their application to electric double-layer capacitors. Electrochim Acta 2006;52:1763–70.
[345] Lai Y, Chen X, Zhang Z, Li J, Liu Y. Tetraethylammonium difluoro (oxalato) borate as electrolyte salt for electrochemical double-layer capacitors. Electrochim Acta 2011;56:6426–30.
[346] Nambu N, Takahashi R, Suzuki K, Sasaki Y. Electrolytic properties of tetramethylammonium compound in highly concentrated solutions and its application to electric double-layer capacitors. Electrochemistry 2013;81:811–3.
[347] Li Q, Zuo X, Liu J, Xiao X, Shu D, Nan J. The preparation and properties of a novel electrolyte of electrochemical double layer capacitors based on LiPF6 and acetamide. Electrochim Acta 2011;58:330–5.
[348] Väli R, Laheäär A, Jänes A, Lust E. Characteristics of non-aqueous quaternary solvent mixture and Na-salts based supercapacitor electrolytes in a wide temperature range. Electrochim Acta 2014;121:294–300.
[349] Chandrasekaran R, Koh M, Yamauchi A, Ishikawa M. Electrochemical cell studies based on non-aqueous magnesium electrolyte for electric double layer capacitor applications. J Power Sources 2010;195:662–6.
[350] Lee G, Kim JW, Park H, Lee JY, Lee H, Song C, et al. Skin-like, dynamically stretchable, planar supercapacitors with buckled carbon nanotube/Mn–Mo mixed oxide electrodes and air-stable organic electrolyte. ACS Nano 2018;13:855–66.
[351] Huang CW, Wu CA, Hou SS, Kuo PL, Hsieh CT, Teng H. Gel electrolyte derived from poly (ethylene glycol) blending poly (acrylonitrile) applicable to roll-to-roll assembly of electric double layer capacitors. Adv Funct Mater 2012;22:4677–85.
[352] Pan S, Yao M, Zhang J, Li B, Xing C, Song X, et al. Recognition of ionic liquids as high-voltage electrolytes for supercapacitors. Front Chem 2020;8:261.
[353] Aetizaz M, Sarfaraz S, Ayub K. Interaction of imidazolium based ionic liquid electrolytes with carbon nitride electrodes in supercapacitors; a step forward for understanding electrode–electrolyte interaction. J Mol Liq 2023;369:120955.
[354] Wong SI, Lin H, Ma T, Sunarso J, Wong BT, Jia B. Binary ionic liquid electrolyte design for ultrahigh-energy density graphene-based supercapacitors. Materials Reports: Energy 2022;2:100093.
[355] Sampaio AM, Pereira GFL, Salanne M, Siqueira LJA. Comparing the performance of sulfonium and phosphonium ionic liquids as electrolytes for supercapacitors by molecular dynamics simulations. Electrochim Acta 2020;364:137181.
[356] Bhowmick S, Tatrari G, Filippov A, Johansson P, Shah FU. Structurally flexible pyrrolidinium-and morpholinium-based ionic liquid electrolytes. Phys Chem Chem Phys 2023;25:19815–23.
[357] de Araujo CH, Fileti EE, Colherinhas G. A molecular dynamics study of graphyne-based electrode and biocompatible ionic liquid for supercapacitor applications. J Mol Liq 2022;360:119494.
[358] de Araujo CH, Fileti EE, Colherinhas G. Comparing supercapacitors with graphene/graphyne electrodes and [Bmim][PF6],[Emim][BF4],[Ch][Gly] and [Pyr][Tfsi] ionic liquids using molecular dynamics. J Mol Liq 2023;379:121703.
[359] Seenath JS, Pech D, Rochefort D. Investigation of protic ionic liquid electrolytes for porous RuO2 micro-supercapacitors. J Power Sources 2022;548:232040.
[360] Stettner T, Balducci A. Protic ionic liquids in energy storage devices: Past, present and future perspective. Energy Storage Mater 2021;40:402–14.
[361] Feng J, Wang Y, Xu Y, Sun Y, Tang Y, Yan X. Ion regulation of ionic liquid electrolytes for supercapacitors. Energ Environ Sci 2021;14:2859–82.
[362] Timperman L, Galiano H, Lemordant D, Anouti M. Phosphonium-based protic ionic liquid as electrolyte for carbon-based supercapacitors. Electrochem Commun 2011;13:1112–5.
[363] Denshchikov K, Izmaylova M, Zhuk A, Vygodskii Y, Novikov V, Gerasimov A. 1-Methyl-3-butylimidazolium tetraflouroborate with activated carbon for electrochemical double layer supercapacitors. Electrochim Acta 2010;55:7506–10.
[364] Brandt A, Pires J, Anouti M, Balducci A. An investigation about the cycling stability of supercapacitors containing protic ionic liquids as electrolyte components. Electrochim Acta 2013;108:226–31.
[365] Maiti S, Pramanik A, Chattopadhyay S, De G, Mahanty S. Electrochemical energy storage in montmorillonite K10 clay based composite as supercapacitor using ionic liquid electrolyte. J Colloid Interface Sci 2016;464:73–82.
[366] Chen Y, Zhang X, Zhang D, Ma Y. High power density of graphene-based supercapacitors in ionic liquid electrolytes. Mater Lett 2012;68:475–7.
[367] Yang CH, Huang PL, Luo XF, Wang CH, Li C, Wu YH, et al. Holey Graphene Nanosheets with Surface Functional Groups as High-Performance Supercapacitors in Ionic-Liquid Electrolyte. ChemSusChem 2015;8:1779–86.
[368] Iamprasertkun P, Krittayavathananon A, Sawangphruk M. N-doped reduced graphene oxide aerogel coated on carboxyl-modified carbon fiber paper for high-performance ionic-liquid supercapacitors. Carbon 2016;102:455–61.
[369] Deng M-J, Chang J-K, Wang C-C, Chen K-W, Lin C-M, Tang M-T, et al. High-performance electrochemical pseudo-capacitor based on MnO 2 nanowires/Ni foam as electrode with a novel Li-ion quasi-ionic liquid as electrolyte. Energ Environ Sci 2011;4:3942–6.
[370] Xie HJ, Gélinas B, Rochefort D. Redox-active electrolyte supercapacitors using electroactive ionic liquids. Electrochem Commun 2016;66:42–5.
[371] Tsai W-Y, Lin R, Murali S, Zhang LL, McDonough JK, Ruoff RS, et al. Outstanding performance of activated graphene based supercapacitors in ionic liquid electrolyte from− 50 to 80 C. Nano Energy 2013;2:403–11.
[372] Jamil R, Silvester DS. Ionic liquid gel polymer electrolytes for flexible supercapacitors: Challenges and prospects. Curr Opin Electrochem 2022;35:101046.
[373] Lee KS, Jeong HT. Development and optimization of ionic liquid based gel polymer electrolyte for all solid-state supercapacitor. J Storage Mater 2021;42:103001.
[374] Pandey G, Hashmi S. Solid-state supercapacitors with ionic liquid based gel polymer electrolyte: effect of lithium salt addition. J Power Sources 2013;243:211–8.

[375] Lee J, Kim W, Kim W. Stretchable carbon nanotube/ion–gel supercapacitors with high durability realized through interfacial microroughness. ACS Appl Mater Interfaces 2014;6:13578–86.
[376] Kang DA, Kim K, Karade SS, Kim H, Kim JH. High-performance solid-state bendable supercapacitors based on PEGBEM-g-PAEMA graft copolymer electrolyte. Chem Eng J 2020;384:123308.
[377] Ujjain SK, Sahu V, Sharma RK, Singh G. High performance, all solid state, flexible supercapacitor based on ionic liquid functionalized graphene. Electrochim Acta 2015;157:245–51.
[378] Pan Z, Yang J, Zhang Q, Liu M, Hu Y, Kou Z, et al. All-solid-state fiber supercapacitors with ultrahigh volumetric energy density and outstanding flexibility. Adv Energy Mater 2019;9:1802753.
[379] Murphy JN, Mendes T, Kerton FM, MacFarlane DR. Biorenewable Calcite as an Inorganic Filler in Ionic Liquid Gel Polymer Electrolytes for Supercapacitors. ACS Omega 2023.
[380] Singh MD, Kaur G, Sharma S, Dalvi A. All-solid-state Na+ ion supercapacitors using Na3Zr2Si2PO12-polymer hybrid films as electrolyte. J Storage Mater 2021; 41:102984.
[381] Yoshizawa-Fujita M, Kubota S, Ishimoto S. All-solid-state high-voltage supercapacitors using an ionic plastic crystal-based electrolyte. Front Energy Res 2022; 10:854090.
[382] Gu R, Yu K, Wu L, Ma R, Sun H, Jin L, et al. Dielectric properties and IV characteristics of Li0. 5La0. 5TiO3 solid electrolyte for ceramic supercapacitors. Ceram Int 2019;45:8243–7.
[383] Lokhande P, Chavan U. Inorganic electrolytes in supercapacitor. Mater Res Found 2019;61:11–30.
[384] Zhang X, He B, Zhao Y, Tang Q. A porous ceramic membrane tailored high-temperature supercapacitor. J Power Sources 2018;379:60–7.
[385] Francisco BE, Jones CM, Lee S-H, Stoldt CR. Nanostructured all-solid-state supercapacitor based on Li2S-P2S5 glass-ceramic electrolyte. Appl Phys Lett 2012; 100.
[386] Ulihin A, Mateyshina YG, Uvarov N. All-solid-state asymmetric supercapacitors with solid composite electrolytes. Solid State Ion 2013;251:62–5.
[387] Liao G, Mahrholz T, Geier S, Wierach P, Wiedemann M. Nanostructured all-solid-state supercapacitors based on NASICON-type Li 1.4 Al 0.4 Ti 1.6 (PO 4) 3 electrolyte. J Solid State Electrochem 2018;22:1055–61.
[388] Hu X, Chen Y, Hu Z, Li Y, Ling Z. All-solid-state supercapacitors based on a carbon-filled porous/dense/porous layered ceramic electrolyte. J Electrochem Soc 2018;165:A1269.
[389] Kaur G, Sivasubramanian SC, Dalvi A. Solid-state supercapacitors using ionic liquid dispersed Li+-NASICONs as electrolytes. Electrochim Acta 2022;434: 141311.
[390] Sharma S, Dalvi A. Solid polymer electrolyte membranes using the "polymer-in-ceramic" approach for all-solid-state supercapacitor applications. Solid State Ion 2022;387:116063.
[391] Yu K, Tian Y, Gu R, Jin L, Ma R, Sun H, et al. Ionic conduction, colossal permittivity and dielectric relaxation behavior of solid electrolyte Li3xLa2/3-xTiO3 ceramics. J Eur Ceram Soc 2018;38:4483–7.
[392] Li R, Liao K, Zhou W, Li X, Meng D, Cai R, et al. Realizing fourfold enhancement in conductivity of perovskite Li0. 33La0. 557TiO3 electrolyte membrane via a Sr and Ta co-doping strategy. J Membr Sci 2019;582:194–202.
[393] Lu D-L, Zhao R-R, Wu J-L, Ma J-M, Huang M-L, Yao Y-B, et al. Investigations on the properties of Li3xLa2/3-xTiO3 based all-solid-state supercapacitor: Relationships between the capacitance, ionic conductivity, and temperature. J Eur Ceram Soc 2020;40:2396–403.
[394] Lu D-L, Chang Y, Lu S-G. Properties and working mechanism of Sn-doped Li0. 33La0. 56TiO3-based all-solid-state supercapacitor. J Solid State Electrochem 2023;27:1021–31.
[395] Batisse N, Raymundo-Piñero E. A self-standing hydrogel neutral electrolyte for high voltage and safe flexible supercapacitors. J Power Sources 2017;348: 168–74.
[396] Qiu F, Huang Y, He G, Luo C, Li X, Wang M, et al. A lignocellulose-based neutral hydrogel electrolyte for high-voltage supercapacitors with overlong cyclic stability. Electrochim Acta 2020;363:137241.
[397] Pang M, Jiang S, Zhao J, Zhang S, Wang R, Li N, et al. "Water-in-salt" electrolyte enhanced high voltage aqueous supercapacitor with carbon electrodes derived from biomass waste-ground grain hulls. RSC Adv 2020;10:35545–56.
[398] Deng Y, Wang H, Zhang K, Shao J, Qiu J, Wu J, et al. A high-voltage quasi-solid-state flexible supercapacitor with a wide operational temperature range based on a low-cost "water-in-salt" hydrogel electrolyte. Nanoscale 2021;13:3010–8.
[399] Lu X, Yu M, Wang G, Zhai T, Xie S, Ling Y, et al. H-TiO2@ MnO2//H-TiO2@ C core–shell nanowires for high performance and flexible asymmetric supercapacitors. Adv Mater 2013;25:267–72.
[400] Lu X, Yu M, Zhai T, Wang G, Xie S, Liu T, et al. High energy density asymmetric quasi-solid-state supercapacitor based on porous vanadium nitride nanowire anode. Nano Lett 2013;13:2628–33.
[401] Yu M, Lu Y, Zheng H, Lu X. New insights into the operating voltage of aqueous supercapacitors. Chem–A Eur J 2018;24:3639–49.
[402] Weng Z, Li F, Wang DW, Wen L, Cheng HM. Controlled electrochemical charge injection to maximize the energy density of supercapacitors. Angew Chem Int Ed 2013;52:3722–5.
[403] Dai Z, Peng C, Chae JH, Ng KC, Chen GZ. Cell voltage versus electrode potential range in aqueous supercapacitors. Sci Rep 2015;5:1–8.
[404] Wang J, Feng S-P, Yang Y, Hau NY, Munro M, Ferreira-Yang E, et al. "Thermal charging" phenomenon in electrical double layer capacitors. Nano Lett 2015;15: 5784–90.
[405] Senthilkumar S, Selvan RK, Melo J. Redox additive/active electrolytes: a novel approach to enhance the performance of supercapacitors. J Mater Chem A 2013; 1:12386–94.
[406] Qin W, Zhou N, Wu C, Xie M, Sun H, Guo Y, et al. Mini-review on the redox additives in aqueous electrolyte for high performance supercapacitors. ACS Omega 2020;5:3801–8.
[407] Chun S-E, Evanko B, Wang X, Vonlanthen D, Ji X, Stucky GD, et al. Design of aqueous redox-enhanced electrochemical capacitors with high specific energies and slow self-discharge. Nat Commun 2015;6:1–10.
[408] Hwang JY, Li M, El-Kady MF, Kaner RB. Next-generation activated carbon supercapacitors: a simple step in electrode processing leads to remarkable gains in energy density. Adv Funct Mater 2017;27:1605745.
[409] Licht S, Davis J. Disproportionation of aqueous sulfur and sulfide: kinetics of polysulfide decomposition. J Phys Chem B 1997;101:2540–5.
[410] Skyllas-Kazacos M, Milne N. Evaluation of iodide and titanium halide redox couple combinations for common electrolyte redox flow cell systems. J Appl Electrochem 2011;41:1233–43.
[411] Schweitzer GK, Pesterfield LL. The aqueous chemistry of the elements. OUP USA; 2010.
[412] Jasinski RJ. The electrochemistry of some n-heptylviologen salt solutions. J Electrochem Soc 1977;124:637.
[413] Bird C, Kuhn A. Electrochemistry of the viologens. Chem Soc Rev 1981;10:49–82.
[414] Michaelis L, Hill ES. The viologen indicators. J Gen Physiol 1933;16:859–73.
[415] Weber AZ, Mench MM, Meyers JP, Ross PN, Gostick JT, Liu Q. Redox flow batteries: a review. J Appl Electrochem 2011;41:1137.
[416] Bard A. Standard potentials in aqueous solution. Routledge; 2017.
[417] Suo L, Borodin O, Gao T, Olguin M, Ho J, Fan X, et al. "Water-in-salt" electrolyte enables high-voltage aqueous lithium-ion chemistries. Science 2015;350: 938–43.